STUDIES OF GAAS SOLAR CELLS GROWN BY CLOSE-SPACED VAPOR TRANSPORT

by

JASON BOUCHER

A DISSERTATION

Presented to the Department of Physics
and the Graduate School of the University of Oregon
in partial fulfillment of the requirements
for the degree of
Doctor of Philosophy

December 2016

DISSERTATION APPROVAL PAGE

Student: Jason Boucher

Title: Studies of GaAs Solar Cells Grown by Close-Spaced Vapor Transport

This dissertation has been accepted and approved in partial fulfillment of the requirements for the Doctor of Philosophy degree in the Department of Physics by:

Benjamin McMorran	Chair
Shannon Boettcher	Advisor
Hailin Wang	Core Member
Miriam Deutsch	Core Member
Mark Lonergan	Institutional Representative

and

Scott L. Pratt	Dean of the Graduate School

Original approval signatures are on file with the University of Oregon Graduate School.

Degree awarded December 2016

DISSERTATION ABSTRACT

Jason Boucher

Doctor of Philosophy

Department of Physics

December 2016

Title: Studies of GaAs Solar Cells Grown by Close-Spaced Vapor Transport

While photovoltaic (PV) manufacturing is on track to provide a substantial portion of world electricity generation, the growth of the industry is likely to be lower than desired to meet targets designed to mitigate climate change. Many different PV technologies have been developed, but PV modules based on Si are the dominant technology due to its low cost and relatively high energy conversion efficiencies. PV modules based on III-V materials are primarily used for aerospace applications due to their high cost and record-setting efficiencies. Traditional manufacturing techniques for III-V PV require expensive precursors, and have high capital costs and low throughput. Close-spaced vapor transport (CSVT) is an alternative technique for deposition of III-V materials that was invented in the 1960s but has not been fully developed for the production of PV devices. This work describes progress towards high efficiency solid-state GaAs solar cells produced by CSVT.

Previous results have demonstrated good electronic quality of CSVT GaAs using photoelectrochemical cells, but such devices have not been demonstrated to be commercially practical. This work investigates the potential of CSVT to produce high-efficiency III-V PV by fabricating and characterizing GaAs films and simple homojunction solar cells. Chapter I describes the motivation and state of III-V PV

research, and establishes basic device physics background. Chapter II gives details of film growth and device design and fabrication. Chapter III gives an overview of the film and device characterization methods employed. Chapter IV explores the primary limitations in the efficiency of the homojunction solar cells fabricated for this study and discusses some practical concerns in translating the technique to a manufacturing environment. Chapter V explores the electronically-active defects in both *n*-type films and in *p*-type absorbers of solar cells, which would be likely to limit the efficiency of devices optimized considering the results presented in Chapter IV. Chapter VI discusses some of the possible future directions for applying CSVT to more advanced device structures which are more commercially relevant, including the growth on alternative substrates and growth of ternary materials for passivating layers or multijunction cells.

This dissertation includes previously published and unpublished co-authored material.

CURRICULUM VITAE

NAME OF AUTHOR: Jason Boucher

GRADUATE AND UNDERGRADUATE SCHOOLS ATTENDED:
University of Oregon
Seattle Pacific University

DEGREES AWARDED:
Doctor of Philosophy, Physics, 2016, University of Oregon
Bachelor of Science, Physics and Engineering and Applied Science, 2010, Seattle Pacific University

AREAS OF SPECIAL INTEREST:
Semiconductor Device Physics
Epitaxial Growth
Inorganic Photovoltaics

PROFESSIONAL EXPERIENCE:

Graduate Research and Teaching Assistant, University of Oregon, 2010-2016

Intern, National Renewable Energy Laboratory, Summer 2009 & 2010

GRANTS, AWARDS AND HONORS:

Magna cum Laude, Seattle Pacific University, 2010

PUBLICATIONS:

J.W. Boucher, A.L. Greenaway, K.E. Egelhofer, S.W. Boettcher, "Analysis of performance-limiting defects in pn junction GaAs solar cells grown by water-mediated close-spaced vapor transport epitaxy," Sol. Energ. Mat. Sol. C., vol. 159, pp. 546-552, Oct. 2016.

A. L. Greenaway, A. L. Davis, J. W. Boucher, A. J. Ritenour, S. Aloni, S. W. Boettcher, "Gallium arsenide phosphide grown by close-spaced vapor transport from mixed powder sources for low-cost III-V photovoltaic and photoelectrochemical devices," J. Mater. Chem. A, vol. 4, no. 8, pp. 2909-2918, Nov. 2015

J.W. Boucher, A.L. Greenaway, A.J. Ritenour, A.L. Davis, B.F. Bachman, S. Aloni, S.W. Boettcher, “Low-cost growth of III-V layers on Si using close-spaced vapor transport,” 42nd Photovolt. Spec. Conf., pp. 1-4, Jun. 2015

A.J. Ritenour, J.W. Boucher, R. DeLancey, A.L. Greenaway, S. Aloni, S. W. Boettcher. “Doping and electronic properties of GaAs grown by close-spaced vapor transport from powder sources for scalable III-V photovoltaics,” Energ. & Environ. Sci., vol. 8, no. 1, pp. 278-285, 2015.

J.W. Boucher, D.W. Miller, C.W. Warren, J.D. Cohen, B.E. McCandless, J.T. Heath, M.C. Lonergan, S.W. Boettcher, “Optical response of deep defects as revealed by transient photocapacitance and photocurrent spectroscopy in CdTe/CdS solar cells,” Sol. Energ. Mat. Sol. C., vol. 129, pp. 57-63, Oct. 2014.

J.W. Boucher, A.J. Ritenour, A.L. Greenaway, S. Aloni, S. W. Boettcher, “Homojunction GaAs solar cells grown by close space vapor transport,” 40th Photovolt. Spec. Conf., pp. 0460-0464, Jun. 2014.

J.W. Boucher, A.J. Ritenour, S.W. Boettcher, “Towards low-cost high-efficiency GaAs photovoltaics and photoelectrodes grown via vapor transport from a solid source,” Proc. SPIE 8725, pp. 87250Z, May 2013.

ACKNOWLEDGEMENTS

Graduate school has been a wonderful, awful experience that was tolerable and often fun only because of the great people who I have known during my time here. I owe them all a tremendous thanks.

First and foremost, I would like thank my parents for putting me through so many years of schooling, and continuing to encourage me throughout graduate school, as none of this would have even started without them. I also thank my late advisor, David Cohen, for supporting me as I started my research here, and I appreciate the subsequent support of Mark Lonergan and his students in keeping solar cell defect characterization work going at this university. I would like to especially thank Wes Miller, Charles Warren, and Ellis Roe for many conversations about solar cell characterization. Additionally, much of the DLTS data in this work would not have been collected without the percussive maintenance performed by Wes on the capacitance meter.

I would also like to acknowledge the support of the technical science administration. Clifford Dax, John Boosinger, Jeffrey Garman, and Kris Johnson have provided an invaluable resource in building and maintaining equipment throughout my time here. Also, much of the research in this work was performed using equipment in the Center for Advanced Materials Characterization in Oregon (CAMCOR) and the staff there have always been helpful and pleasure to work with.

Of course none of this work would have been possible without my advisor, Dr. Shannon Boettcher, whose passion for doing good science has been a great source of inspiration. I would like to specifically thank the members of team III-V: Ann Greenaway, Ben Bachman, Chris Funch, and Andrew Ritenour, who started the project and put up with me when I first joined. All of the members of the Boettcher lab have been wonderful to work with, but I would particularly like to thank Matt Kast and Adam Smith, who were here when I first joined and who have always had insightful comments to make in any situation.

Finally, I would like to thank my friends and acquaintances both inside and outside the university who have joined me on so many adventures in the wilderness around Oregon and generally helped keep me sane.

This research was made possible by funding from the U.S. Department of Energy Sunshot Initiative BRIDGE program (DE-EE0005957) and by the Research Corporation for Scientific Advancement through a Scialog Scholar Award (SWB).

TABLE OF CONTENTS

Chapter Page

Chapter Page

LIST OF FIGURES

Figure Page

Figure Page

LIST OF TABLES

Table Page

CHAPTER I

INTRODUCTION AND BACKGROUND

Overview

This work describes progress towards producing low-cost III-V solar cells with high efficiencies. The first chapter gives background information on the relevant physics and provides a comparison with other plausibly low-cost techniques. The second chapter describes the process for growing films and fabricating solar cells. The third chapter discusses the various characterization techniques which have been used. Portions of Chapter III were taken from Boucher, J.W.; Miller, D.W.; Warren, C.W.; Cohen, J.D.; McCandless, B.E.; Heath, J.T.; Lonergan, M.C.; Boettcher, S.W. Optical response of deep defects as revealed by transient photocapacitance and photocurrent spectroscopy in CdTe/CdS solar cells. Solar Energy Materials and Solar Cells, 2014. It was written entirely by me with editorial assistance of my co-authors. The data was collected by me with assistance from D.W.M and C.W.W..

Chapter IV describes the current performance limitations of homojunction cells, and includes data and text from Boucher, J.W.; Ritenour, A.J.; Greenaway; A.L., Aloni, S.; and Boettcher, S.W. Homojunction GaAs Solar Cells Grown by Close Space Vapor Transport. Proc. 40th IEEE Photovolt. Spec. Conf., 2014. It was written entirely by me with editorial assistance of my co-authors. Some of the data was collected with A.J.R. Portions of this chapter were also taken from Boucher, J. W.; Greenaway, A. L.; K. E. Egelhofer, K. E.; Boettcher, S. W. Analysis of performance-limiting defects in pn junction GaAs solar cells grown by water-mediated close-spaced vapor transport epitaxy. Accepted manuscript in Solar Energy Materials and Solar

Cells, 2016. It was written entirely by me with editorial assistance of my co-authors. Some of the data was collected by K.E.E. under my direction.

Chapter V describes the microscopic defect character of CSVT films and the relationship with growth conditions, and Chapter VI describes future directions for CSVT growth. Portions of this chapter were taken from Boucher, J.W.; Greenaway, A.L.; Ritenour, A.J.; Davis, A.L.; Bachman, B. F.; Aloni, S.; and Boettcher, S.W. Low-Cost Growth of III-V Layers on Si Using Close-Spaced Vapor Transport. It was written entirely by me with editorial assistance of my co-authors. Data was collected by myself or B.F.B under my direction.

Motivation

Demand for renewable energy has increased rapidly as climate projections show a need for reduced CO_2 emissions. Since 2004, installed photovoltaic (PV) capacity in the United States has increased by over two orders of magnitude, and now exceeds 10 GW, though this is still only a small fraction of the total energy generation capacity [1]. Market projections for PV predict 2–4 TW of capacity by 2030, though climate projections suggest that as much as 11 TW will be required to limit global warming to 1.5–2 °C [2]. Thus, significant innovation in PV is still required to minimize the risks to the climate.

Compound semiconductors made of elements from group III and V on the periodic table (III-V materials) are commonly used to produce devices such as transistors and LEDs, and particularly are used as the light-absorbing material in high efficiency solar cells. Epitaxial growth of III-V films is currently dominated by two techniques: molecular beam epitaxy (MBE) and metalorganic vapor phase epitaxy (MOVPE) both of which can produce films with precise control of alloy composition and dopant incorporation. Since MBE requires high vacuum and has poor precursor utilization it has not been adopted for commercial growth, while MOVPE is widely used in the production of complex multijunction solar cells for aerospace applications. MOVPE has high capital costs, in part due to the need for safety infrastructure to handle toxic and pyrophoric precursor materials (e.g., AsH_3 and trimethylgallium) and precursor utilization is still relatively low [3]. Due to the costs, III-V solar cells are typically only used for terrestrial applications in concentrator systems where very small cells can convert large amounts of energy, though these systems are not economically viable in many climates. Recently, several alternative growth techniques have seen renewed interest as the dominant photovoltaic technology, Si, approaches theoretical limiting efficiencies and cost decreases have slowed.

The largest costs in III-V deposition are associated with the substrate and precursor utilization. Most III-V solar cells are grown epitaxially either on a Ge or a GaAs single-crystal wafer, and these substrates are much more expensive than their Si counterparts. A number of strategies have been proposed to address this, all of which rely on either reusing a substrate or replacing it with a lower-cost substrate. Reuse of the substrate can be achieved by employing epitaxial liftoff, in which a sacrificial layer (typically AlAs) is grown prior to the device structure, and then etched away with the device attached to a flexible handle. Similarly, a technique called spalling [4] has been investigated to remove controlled layer thicknesses by mechanical means. Reuse of wafers is an attractive option as III-V solar cells are grown in an inverted configuration or employ a back-reflector to provide voltage enhancements from photon recycling (where photons are effectively concentrated near the junction due to radiative recombination and reabsorption within the absorbing material) [5].

Alternative Deposition Techniques for III-V Semiconductors

Three deposition techniques have been investigated in recent years for their potential cost reductions, and these are summarized below.

Hydride Vapor Phase Epitaxy (HVPE)

HVPE is commonly used for the growth of GaN films but has historically not been favored for production of III-V-based photovoltaics. Recently, the National Renewable Energy Laboratory (NREL) has redeveloped the technique and demonstrated unpassivated homojunction devices with uncertified one-sun efficiencies reaching 9.5 % and passivated efficiencies of 16.5 % [6, 7]. The HVPE reactor at NREL is comprised of a custom fused quartz chamber through which H_2 is flowed as a carrier gas. As with MOVPE, the source of arsenic for HVPE is AsH_3, though the overpressure required is reportedly decreased. The group III precursors are introduced as pure metals in a heated boat upstream of the deposition zone, and are transported using HCl gas. Typically, source temperatures are ~700 °C. Very high growth rates above 1 µm have been achieved with no apparent degradation in crystal quality. While doping is still accomplished with metalorganic compounds, the group III elements are introduced as pure metals and transported with high utilization using HCl, which decreases the cost of deposition. For comparison, the price of trimethylgallium has been reported at $2.50/g, while Ga metal is only $0.29/g [6]. In contrast to MOVPE, compositional grading is achieved by varying the temperature or amount of transport agent added to the metal source streams. Binary and ternary compounds containing In and P have also been reported by HVPE, suggesting that it could be applied to tandem or multijunction PV structures in a similar fashion as MOVPE. Deposition of Al-containing compounds is a challenge due to the high reactivity of the chlorides with the fused silica reactor walls as well as its affinity for oxygen.

Thin-film Vapor Liquid Solid (TF-VLS) Growth

TF-VLS growth, also referred to as templated liquid phase growth, is a technique developed recently for growing films on non-epitaxial substrates [8, 9]. Heterojunction devices fabricated by the Javey group using p-InP absorbers have reached uncertified efficiencies of 12.1 % [8]. In this technique, In is first deposited onto Mo foil or sputtered Mo on SiO_2/Si, then it is capped by SiO_x and exposed to a PH_3:H_2 flux at 750 °C and 100 Torr which initiates a dendritic growth mechanism. After the initial dendrites coalesce, grain sizes in the final films can be in excess of 100 µm. Devices are fabricated by depositing a window of n-TiO_2 and a transparent conductive oxide contact layer.

Though In is very expensive, it could be electrochemically deposited in a high-throughput process with essentially unity utilization, and only a thin film is required. However, GaP is the only other III-V that has been deposited by TF-VLS [9], and there is no clear approach for fabricating tandem or multijunction devices. The best V_{oc} reported for InP solar cells under one-sun equivalent illumination is only 692 mV, implying a voltage deficit of 650 mV relative to the band gap. In comparison, the best published HVPE and CSVT GaAs cells have voltage deficits of ~500 mV.

Close-Spaced Vapor Transport (CSVT)

CSVT was explored as early as the 1960s for the growth of III-V semiconductors [10]. In this process, solid precursors (doped or undoped GaAs wafers or pressed powder) are used to generate in situ gas phase compounds which transport by diffusion to the substrate which is placed in close proximity. Growth rates above 1 µm min^{-1} have been reported using CSVT. Our first-generation design uses ∼1000–10,000 ppm H_2O diluted in H_2 at 1 atm as a group III transport agent, though HCl has also been used in this regard. Devices are fabricated by sequential deposition of a p-GaAs absorber and an n^+-GaAs emitter, which in the current design requires exposure to air between layers to change the source material. Growth temperatures for CSVT are typically ∼800 °C when using H_2O as a transport agent.

CSVT is unique in that it uses a solid source for the group V element, eliminating the need for toxic hydrides. Close-spaced vapor transport (CSVT) of GaAs is a plausibly scalable process, similar to commercial CdTe deposition, which uses water vapor to generate gas-phase As_2 and Ga_2O in situ at atmospheric pressure with high (∼1 µm/min) growth rates and 95% overall transport efficiency [11, 12]. Doping and compositional control are more challenging in CSVT, however, as it requires either a change of the solid source material or injection of gas-phase reactants into a small, enclosed volume. Multijunction architectures requiring metamorphic buffer layers are therefore a significant engineering challenge for CSVT, though two-junction tandems are more feasible in the short term. Much of this work is concerned with fabrication of homojunction GaAs solar cells which serve as a benchmark for the process.

Semiconductor and Device Physics

Semiconductor Energy Bands

For isolated atoms, the position of valence electrons can be probabilistically represented (as dictated by quantum mechanics) by atomic orbitals with widely spaced energy levels. In a solid material, however, the wavefunctions of electrons from adjacent atoms have significant overlap. Since electrons are fermions, only one can occupy a given quantum state and therefore the energy levels must spread out into energy bands. In semiconductors, there are energies between two bands for which no electron states exist. In the lower energy band, called the valence band, the states are mostly filled, while in the upper band, the conduction band, the states are mostly empty. Since electrons cannot move into filled states, electrons must exist in conduction band or must be missing from the valence band in order for current to flow through a material. The latter empty states can be treated as positive charge carriers and are called holes.

The band structure of semiconductors can be quite complex since the energy states depend on the electron momentum in three dimensions. This is usually simplified by considering only the first conduction band minimum (CBM) and valence band maximum (VBM), as this determines the minimum energy gap, E_g between the bands. An example of such a simplified band diagram for GaAs with no applied voltage is shown in Fig. 1. Band diagrams such as this are drawn in reference to electron energy, such that positive charges tend to move upward toward lower energy.

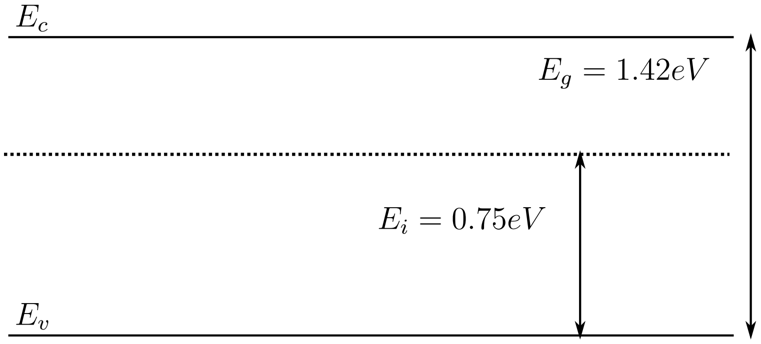

FIGURE 1. Band diagram for GaAs. Conduction band, valence band, band gap, and intrinsic Fermi energy at room temperature are indicated.

For GaAs, the transition between the VBM and CBM requires no change in momentum so it is called a direct bandgap material. Absorption of photons across the direct gap is much more likely since it does not require absorption of a phonon, so only a few microns of GaAs is required to absorb most of the incoming light in a single pass, while Si, an indirect bandgap material, requires ~100 µm. This property of GaAs makes it possible to fabricate flexible solar cells as such thin layers can be bent significantly without breaking. Additionally, the materials costs for III-V solar cells could actually be lower than Si since cells can be so much thinner, even though costs per gram of precursor are much higher as the elements are less earth abundant or have high processing costs [13].

Occupation of Electronic States and Doping

The probability of occupation for a state in a semiconductor is given by the Fermi-Dirac distribution

$$f(E) = \frac{1}{1 + e^{(E-E_f)/kT}} \tag{1.1}$$

Where E_f is called the fermi level or fermi energy and is the position at which the probability of occupation is 1/2. The number of electrons in the conduction band can then be determined by multiplying $f(E)$ by the density of states, usually denoted $g(E)$ and integrating over the conduction band. The density of states, and therefore the fermi level, can be modified by adding impurities, called dopants, to a semiconductor as these introduce states near one of the band edges.

Dopants can produce either positively charged centers (donors) or negatively charged centers (acceptors), and for some elements this can be predicted simply based on their position on the periodic table. For instance, in GaAs, elements in group VI tend to incorporate on arsenic lattice sites, and contribute an extra electron, forming positively charged donors, whereas the opposite is true for elements in group II. Films which have an abundance of donor atoms are called n-type, since their conductivity is dominated by negatively charged electrons, while films dominated by acceptor atoms are called *p*-type and have conductance defined by hole concentration.

PN Junction Solar Cells

Solar cells most commonly consist of a number of inorganic semiconductor layers of different properties. The photovoltaic effect in such materials describes the observation of a voltage generated by light with energy $h\nu > E_g$. Such voltage is explained by the excitation of electrons across the band gap in conjunction with a spatial asymmetry in the conductivity of charge carriers.

To produce useful semiconductor devices, the incorporation of dopants must typically be controllable as the aforementioned asymmetry is commonly provided by depositing layers with different dopant types. When semiconductors of opposite conductivity type are grown on top of each other, they form a *pn* junction. The *pn* junction is one of the most fundamental semiconductor structures and is the basis for many solar cell devices due to the built-in asymmetry which creates a preferred direction for electric current across the cell.

It is common for the diode behavior *pn* junctions to be explained using a band diagram as shown in Fig. 2 for a *pn* junction at equilibrium. When the junction is formed, holes from the *p*-type side tend to diffuse into the *n*-type side, and vice versa. At equilibrium, there is no driving force for current flow so this current must be exactly counterbalanced by the electric field. This explanation is somewhat misleading, however, as a logical extension is to assume that, under illumination, the current in a *pn* junction is driven by the electric field. It also implies that actual opposing diffusive and drift currents exist in equilibrium, which cannot be the case as these would cause resistive heating in the absence of an energy source. In reality, the current depends on both the electric field (drift) and the carrier concentration gradients (diffusion) which are a result of the doping gradient. A more generalized approach to understanding the operating principles of solar cells is given by Wurfel [14]. Under this approach, it is more illustrative to consider the concentration gradient (or equivalently the chemical potential gradient) and the electric field (the electric potential gradient) as driving forces whose sum determines the overall current of electrons or holes. For instance, for electrons the total current is

$$j_n = -\frac{\sigma_n}{q}\nabla(\phi_{chem,n} + \phi_{elec,n}) \tag{1.2}$$

where $\phi_{chem,n} = \phi_{chem,n,0} + kT\ln\frac{n}{N_0}$ for some standard potential $\phi_{chem,n,0}$ and concentration N_0 [14]. The sum of these two potentials, whether in the dark or at steady state, gives the electrochemical potential for electrons, and this is commonly referred to as the *quasi-Fermi level.* The current through any solar cell can therefore be determined entirely by the gradient in the quasi-Fermi levels of the holes and electrons and does not require explicit consideration of drift and diffusion currents.

The total current, given as a function of voltage, through an ideal *pn* junction was first derived by Shockley [15] and is given by

$$J = J_0\left(e^{\frac{qV}{kT}} - 1\right) - J_{sc} \tag{1.3}$$

where J_0 is a material-dependent quantity called the reverse bias saturation current, q is the fundamental charge, V is the applied voltage, k is Boltzmann's constant, T is the temperature, and J_{sc} is the short-circuit current (assuming the light-induced current is voltage-independent). This equation follows from several assumptions: (1) the regions far from the junction are uncharged ("quasi-neutral regions") (2) doping

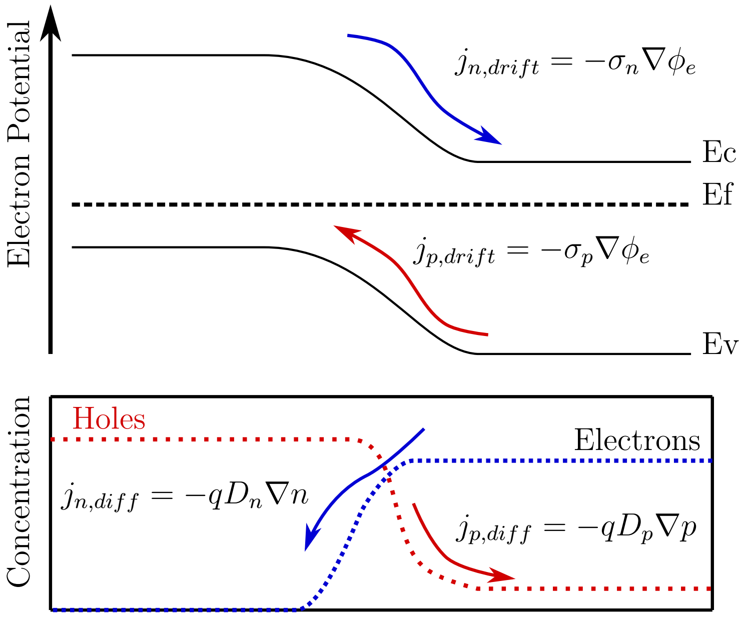

FIGURE 2. Schematic band diagram for a *pn* junction in the dark. Also shown are qualitative carrier concentrations for a *pn* junction at equilibrium with different virtual current contributions indicated.

is constant on either side of the junction (3) the region near the junction is depleted of free carriers ("depletion region") and has charge density equal to the dopant density. Without these assumptions, the current must be solved for numerically and a number of software packages are available for such modeling.

Under illumination, J_{sc} becomes nonzero and the device can operate as a solar cell producing power. The amount of current produced depends on many characteristics of the device, but in particular on the thickness of the layers and a quantity called the minority carrier diffusion length, denoted as L_n or L_p for p- and n-type material, respectively. The quantity L_n characterizes the average distance that an electron will travel before recombining. It depends on the carrier mobility μ and lifetime τ (the average time before recombination) through the relation

$$L = \sqrt{\frac{kT}{q}\mu\tau} \tag{1.4}$$

Mobility is most impacted by ionized defects and carrier concentration, both of which cause carriers to scatter. Lifetime is often dependent on the amount of Shockley-Read-Hall recombination (recombination through defects deep within the band gap), though in high quality GaAs and other direct gap semiconductors lifetimes can become limited by radiative recombination across the band gap. A final recombination mechanism which is prevalent in indirect gap semiconductors such as Si is Auger recombination, in which a first carrier gives up energy to a second carrier within the band; the energy is usually then converted to thermal energy as the second carrier gives up its energy to lattice vibrations in relaxing to the band edge.

It is important to note that some recombination is unavoidable in a solar cell, as this is both necessary to maintain charge neutrality while current flows and also must occur for thermodynamic reasons. The latter point is realized by considering that a solar cell essentially operates as a heat engine with the sun as the hot reservoir and Earth as the cold reservoir. Thus, the absolute maximum efficiency is given by the Carnot efficiency $\eta = 1 - T_C/T_H$, though many other efficiencies have been derived for solar cells. The most famous solar cell efficiency limit is called the Shockley-Quiesser limit [16], which is derived under the assumption that (1) a solar cell has only a single band-gap and light with energy in excess of that gap provides no additional current; (2) the sun subtends a finite solid angle (zero light concentration); (3) that current-voltage characteristics are given by Eq. (1.3); and (4) that the minority diffusion lengths are limited by radiative recombination. This last assumption follows from a *detailed balance* consideration, which requires that in equilibrium each process of carrier generation must be independently balanced by the inverse recombination mechanism. To date, the most effective method of exceeding this limit (strictly speaking) has been to use two or more materials with different band gaps, such that minimal energy is lost in thermalization processes or lack of absorption.

Since carrier lifetimes in GaAs are usually limited by SRH recombination, it is useful to consider this process quantitatively. Under low level injection (photogenerated carrier densities less than the dopant density) and for defects near the intrinsic fermi level, the lifetime is calculated as

$$\tau_{SRH} = \frac{1}{v\sigma N_t} \tag{1.5}$$

where v is the average carrier velocity, σ is the trap capture cross section, and N_t is the trap density [17]. If multiple recombination mechanisms are important, lifetimes can be added in inverse (as recombination rates) to calculate the overall carrier lifetime. Fig. 3 shows the theoretical effect of a defect with $\sigma = 1 \times 10^{-14}\,\mathrm{cm}^2$ near the middle of the band gap as a function of concentration. As shown, the lifetime can be impacted dramatically even by defects with concentration as low as a few parts per billion ($\sim 1 \times 10^{14}\,\mathrm{cm}^{-3}$), and various techniques have been developed to measure such defect concentrations. Many of these require measurement of the solar cell capacitance, as described below.

Depletion Capacitance

The capacitance of a *pn* junction is given simply as the amount of charge added in response to a voltage perturbation by

$$C = \frac{dQ}{dV} \tag{1.6}$$

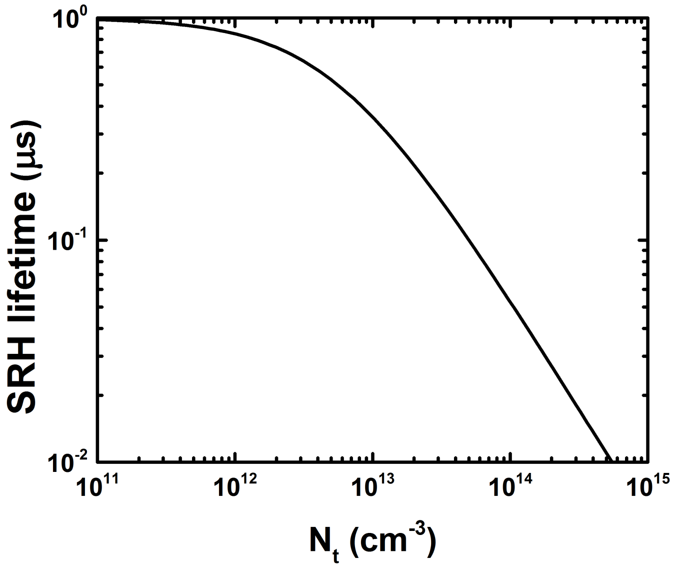

FIGURE 3. Theoretical minority carrier lifetime. Curve is for a defect with $\sigma = 1 \times 10^{-14}\,\mathrm{cm}^2$ as a function of defect concentration. At low trap density, the lifetime is limited by radiative recombination.

with Q being the total charge added to one side of the junction and V the applied bias. In one dimension, Q can be calculated by solving Poisson's equation to determine the depletion width. This can be calculated for arbitrary doping profiles, but devices are commonly fabricated with approximately constant doping profiles on either side of the junction and a much higher doping on one side. Assuming a junction with $N_d << N_a$, this produces the useful relation:

$$x_d = \sqrt{\frac{2\epsilon V}{qN_d}} \tag{1.7}$$

Since the fixed charge on the n-type side of the junction is simply qN_dAx_d, the capacitance can be calculated simply using Eq. (1.6), with the simple result

$$C = \frac{\epsilon A}{x_d} \tag{1.8}$$

This is identical to the well-known parallel-plate capacitor relation. Thus, a useful qualitative model of a *pn* junction solar cell is a parallel-plate capacitor with spacing that increases in reverse bias and decreases in forward bias.

Since x_d depends on the fixed charge density in the depletion region, measurement of capacitance as a function of applied bias allows for calculation of the ionized dopant density. Furthermore, the junction capacitance changes in response to charge trapped in localized states within the depletion region. Thus, a wide variety of techniques have been developed to use capacitance to determine properties of defect states within the band gap of semiconductors. Some of these have been applied in this study and are described in detail in Chapter III.

Bridge

In the next chapter, details of the CSVT growth chamber construction are given. This is followed by general discussion of the CSVT growth process and strategies used for doping films. Finally, device fabrication and simulation is discussed.

CHAPTER II

GAAS SOLAR CELL FABRICATION

CSVT Deposition

Close-spaced vapor transport is a subset of a more general class of chemical reactions known as chemical vapor transport (CVT) reactions in which a solid source material is volatilized by a transport agent and is deposited through a temperature gradient by the reverse reaction. The generalized reaction can be written as

$$\mathrm{iA\,(s) + jB\,(g) \rightleftharpoons kC\,(g)}$$

where the equilibrium is shifted toward the right at the source and toward the left in the deposition region. The supersaturation—that is, the degree to which the concentrations of species are shifted from their equilibrium values—is controlled by changing the temperatures of the source and substrate. For an endothermic reaction (one in which the gaseous product has a higher free energy than the solid), material is transported from the higher temperature to the lower temperature.

For all of GaAs films grown in this work, water vapor acts as the transport agent for Ga while As sublimates to form As_2 according to the reaction [18]

$$\mathrm{GaAs + H_2O\,(g) \longrightarrow Ga_2O\,(g) + \frac{1}{2}\,As_2\,(g) + H_2\,(g)} \qquad (2.1)$$

This occurs at atmospheric pressure under an H_2 ambient at temperatures varied between 700 and 900 °C and H_2O concentrations of 500–10,000 ppm. GaAs can also be grown using halide transport agents such as HCl and I_2, but H_2O was chosen for this work due to the simplicity of the reactor design as it does not require as much corrosion resistance. An HCl-based reactor is currently under construction and its advantages are discussed in later chapters.

Reactor Design

A schematic diagram of the first-generation CSVT reactor is shown in Fig. 4. High purity (99.9999 %) H_2 gas is used as a carrier, and flow rate is controlled through two separate mass flow controllers (MFCs). MFC 2 is bubbled through H_2O kept at a constant temperature (usually 10 °C). The actual humidity is measured by a hygrometer upstream of the reaction zone. A turbomolecular pump backed by an oil-free diaphragm pump is used prior to the start of deposition and then the reactor is filled with dry H_2 to ensure the conditions during the initial temperature ramp are identical across growths.

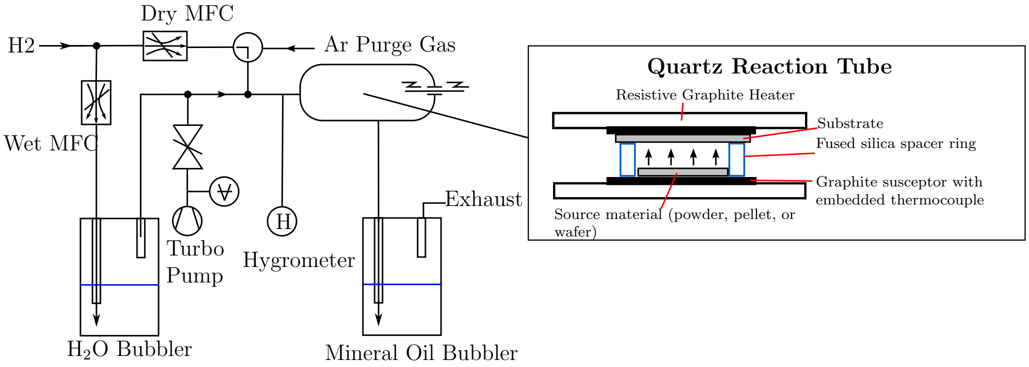

FIGURE 4. Schematic diagram of the CSVT reactor

There are a number of drawbacks to the design of this reactor. First, the source and substrate material are held sandwiched between two graphite blocks which sit inside graphite serpentine-pattern heaters. This requires that the heaters must be removed from the reactor and reassembled for each growth, which allows the source and substrate to be contaminated by atmosphere when performing sequential depositions from different source material. Measurements using time-of-flight secondary ion mass spectrometry (TOF-SIMS) detect increased oxygen and sulfur located at such interfaces [19]. Another drawback to this design is that it incorporates copper wiring and stainless steel screws to attach the heater assembly relatively near to the deposition region. Contamination from such parts should be minimal as they are placed downstream and growth is usually performed with a constant flow of H_2; however, future designs could eliminate this concern by using inductive or radiative heaters at the cost of some simplicity.

Thermodynamics of Growth

CVT has been used historically to synthesize many different materials including semiconductors used for solar energy conversion. A historical review of the development of CVT is given by Binnewies et al. [20] who credit Schäfer with the development of some of the first theoretical models. In particular, Schäfer derived an equation for the rate of mass transport, assuming the transport can be characterized by a single reaction and is limited by diffusive motion:

$$\dot{n} = \frac{i}{j} \cdot \frac{\Delta p}{\sum p} \cdot \frac{\bar{T}^{0.75} \cdot q}{\delta} \cdot 0.6 \times 10^{-4} \, (\mathrm{mol} \cdot \mathrm{hr}^{-1}) \tag{2.2}$$

where i,j are the stoichiometric coefficients of the transport equation, δp is the partial pressure difference of the transporting species, $\sum p$ is the total pressure, $\bar{T}$ is the mean temperature, q is the cross-section of the diffusion path and δ is the length of the diffusion path. The growth is driven by the supersaturation created by the temperature gradient between source and substrate, where supersaturation is often defined as P_i/P_i^0, the ratio between the actual partial pressure of species i and the equilibrium partial pressure. A comparison of CVD and CSVT gas flow and diffusion is shown in Fig. 5.

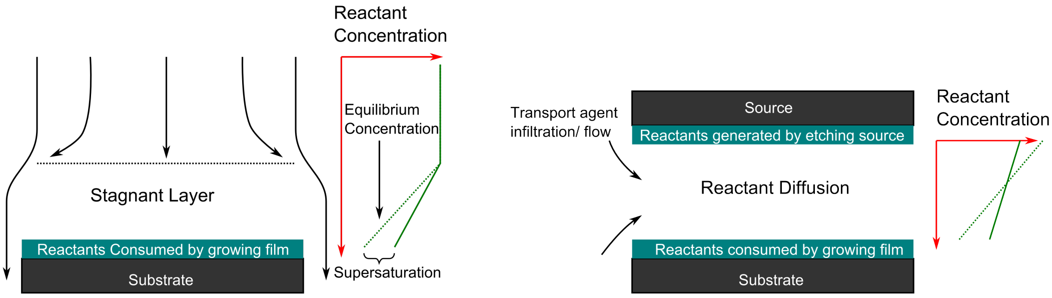

FIGURE 5. Comparison of gas flow and diffusion in CVD and CSVT.

For CSVT, it is usually assumed that the source and substrate are close to equilibrium and therefore the supersaturation is small. Vapor pressures of relevant species can be calculated based on tabulated thermodynamic values and growth rate follows simply by assuming diffusive transport, as in Eq. (2.2). In the model developed by Côté et al., it is assumed that $P_{Ga_2O} = P_{As_2}$ (i.e., Ga and As transport congruently since the reaction zone is confined and source utilization is near 100%) and since the diffusion coefficient for Ga_2O is $D_{Ga_2O} \approx D_{As_2} \leq D_{As_4}$, the rate of growth is limited by the diffusion of Ga_2O. If As_2 is the only As transporting species, the flux is then given by [18]:

$$J_{Ga,As_2} = 2J_{Ga_2O} = 2D_{Ga_2O} \cdot \frac{1}{\delta} \left(\frac{(K(T_1)r)^{1/2}}{RT_1} - \frac{(K(T_2)r)^{1/2}}{RT_2} \right) \tag{2.3}$$

where r is the ratio P_{H_2O}/P_{H_2}, K is the equilibrium constant for reaction 2.1, T_1 is the source temperature and T_2 is the substrate temperature. Note that As_4 also has an appreciable vapor pressure at typical growth temperatures, and this is included in the model of Côté et al. by calculating the fraction $f = P_{As_4}/(P_{As_4} + P_{As_2})$ and considering the equilibrium of the corresponding transport reaction for As_4. Then the overall flux is given by

$$J_{Ga} = f J_{Ga,As_4} + (1-f) J_{Ga,As_2} \tag{2.4}$$

Eqs. (2.2) and (2.3) can both be applied to CSVT, the only difference being that Eq. (2.2) makes assumptions for the value of the diffusion constant and its temperature dependence.

On the basis of these theoretical models, it can be expected that the growth rate changes with water vapor concentration, source/substrate spacing, temperature gradient, and mean temperature. All of these effects have indeed been observed for growth in our reactor, and films have been grown with growth rates ranging from ~10–700 nm min^{-1} in our reactor. Growth rates are partly limited by the temperature gradient achievable, which is ~80 °C at typical source temperatures, while high concentrations of water vapor also increase oxygen incorporation in the films, as discussed in Chapter V. Fig. 6 shows how growth rate increases approximately linearly with ${P_{H_2O}}^{1/2}$ for low water vapor concentrations, and is inversely proportional to δ as expected from Eq. (2.3). A correction is needed at high water concentrations since the As$_4$ flux scales as ${P_{H_2O}}^{2/3}$.

Doping from solid sources

To produce useful photovoltaic devices, it is necessary to grow films with controllable concentrations of n- and p-type dopants, with a range of about 1×10^{17}–1×10^{19} cm^{-3}, with a doping of 1×10^{17} cm^{-3} being used for the light-absorbing layer and 1×10^{19} cm^{-3} or higher used for contact layers. In MOVPE or HVPE, dopants are added by bubbling a carrier gas through a (liquid) organometallic precursor such

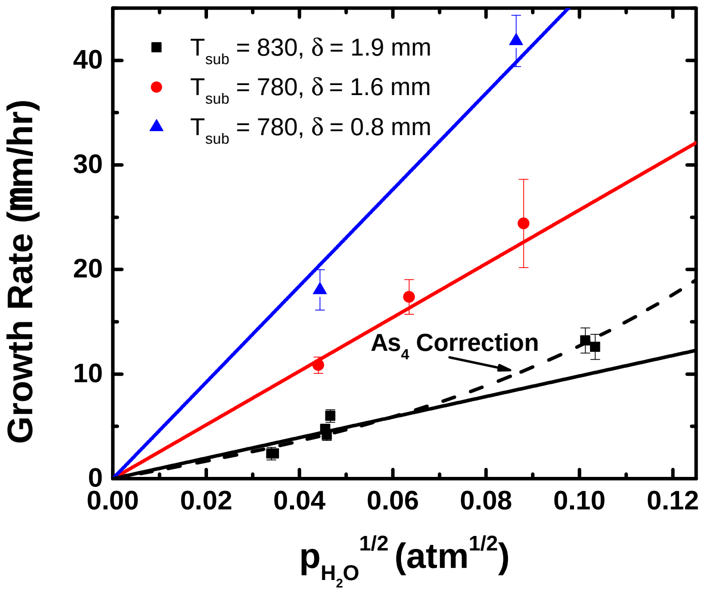

FIGURE 6. Growth rates for CSVT. Rates are given as a function of water vapor concentration and source/substrate spacing for a number of GaAs films grown from pellet sources. The solid lines are linear fits constrained to intersect the origin.

as diethylzinc, or introducing a gas-phase hydride such as SiH_4 in the case of group IV dopants [21, 22]. In MBE, dopants are often incorporated from a separate solid source crucible. Common p-type dopants are Zn, C, and Cd, and common n-type dopants are Te, Si, S, Sn, and Ge. The group IV dopants are amphoteric and can act as n- or p-type dopants depending on whether they incorporate primarily on As sites or Ga sites in the lattice [23, 24].

For CSVT with H_2O as the transport agent, the dopant *oxide* must typically be volatile or it will not be incorporated into the film. In our reactor, Te and Ge have been shown to transport with high efficiency, while Zn transports with less than 1 % efficiency [25], and the other dopants either transport with near zero efficiency (Si, C) or their transport efficiencies have not been established (Cd, Sn, etc.). Dopants can be incorporated directly into the source material, though in some studies of II-VI materials a separate crucible containing the solid dopant material has been utilized [26]. A third method of introducing dopants is through the transport agent; for instance, p-type GaAs has been grown by CSVT using ZnCl [27] which forms the transport agent HCl in situ. In our own studies, dopants are introduced either by using commercial wafers grown by the vertical gradient freeze (VGF) technique and doped by the manufacturer, or by adding metallic dopants directly to GaAs powder [28]. When preparing powder sources, GaAs wafers are ground in a non-porous agate mortar and pestle, which is followed by annealing in a vacuum-sealed quartz ampoule to insure homogeneity when doping with metallic powders. The powder is pressed into a pellet either before or after annealing to produce a flat surface and for ease of handling. When material is annealed after pressing, the films have a lower density of surface defects indicating that particulates may be removed by sintering. This is discussed in more detail in Chapter IV.

Device Fabrication

Contacts

III-V solar cells typically employ a metal grid as a front contact. A metal grid is chosen over a transparent conductive oxide due to the high conductivity of a typical emitter that allows for lateral conduction to the metal grid with little resistive loss. The two contact grids used in this work were designed primarily for ease of processing and both have features that are somewhat larger than is optimal. For the first, a photolithography mask was created with a minimum feature size of 10 µm. The second mask was a stainless steel shadow mask with 50 µm features which allowed for faster processing of cells. Shading losses were estimated to be 1 % and 3 % of J_{sc} respectively.

Microscope images of the grids patterned onto two different cells are shown in Fig. 7. The first was deposited by thermal evaporation of a AuGe eutectic to a thickness of ∼50 nm. Typically, an alloying step under N_2H_2 at 450 °C for 90 s is performed to form a thin, highly-doped region which allows for tunneling current and an ohmic character. Often this step results in balling-up of the AuGe and therefore a more common metalization scheme is AuGeNi, where the addition of Ni improves the surface morphology by either providing a lower surface tension or forming a NiGe alloy with a much higher melting temperature [29–31].

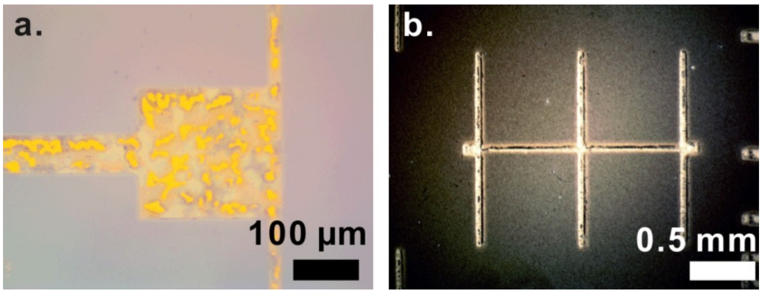

FIGURE 7. *pn* junction contact grids. a) AuGe finger grids deposited using lift-off photolithography patterning displaying discontinuity of the film post-thermal anneal. b) Intact Ni/AuGe finger grid deposited on CSVT film using shadow mask post-thermal anneal.

The front contact grid is usually deposited on top of a degenerately-doped semiconductor layer. This top semiconductor layer would then be mostly etched away, except where the metal grid acts as a mask. A window layer (such as InGaP) would be deposited prior to the degenerately-doped layer to reduce surface recombination and provide an etch stop. In this work, the window layer was not deposited as growth of wide-gap III-V materials has not been fully developed using the CSVT reactor. Thus, devices suffered current loss due to excess doping in the emitter (limiting hole diffusion lengths) or increased contact resistance due to insufficient doping. The photolithography patterns for contact grids and mesa etching are shown in Fig. 8. At the top of the pattern are several contact pads for characterizing the film and contact resistivity using the transfer length method (TLM). The mesa area for each cell is 0.04 cm^2.

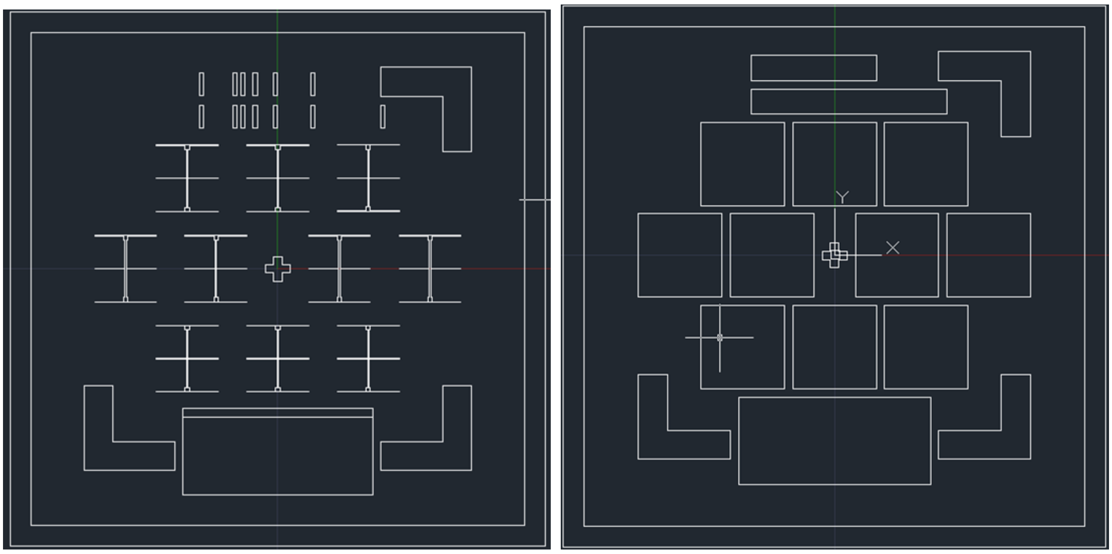

FIGURE 8. Front contact metalization pattern and mesa etching pattern.

Mesa etching was accomplished using a solution of citric acid [$C_3H_4(OH)(COOH)_3 \cdot H_2O$], H_2O and H_2O_2 as described in [32]. The 50 % by weight citric acid:H2O solution was mixed with H_2O_2 in a 5:1 ratio by volume, and had an etch rate of ~0.3 µm/min. Once the emitter layer was fully etched through, the devices are electrically isolated from each other since the junction acts as a barrier for lateral current flow. The small individual device size is desirable since processing for these cells was not carried out in a cleanroom environment, so pinholes and shunt pathways due to dust are only likely to affect one or two cells out of ten fabricated from sequential film depositions.

Device Simulations

A number of software packages are freely available for modelling of solar cells. For this study, PC1D [33] and SCAPS [34] simulation software have been used.

Such simulations are useful both for designing solar cell devices and for explaining experimental results. For instance, a number of simulations were run using the PC1D software package [35] to identify the optimal device designs for our *pn* junction devices and predict their limiting efficiency. Similar results are shown in Fig. 9 using SCAPS. In these simulations, the minority carrier diffusion length for the absorber is varied using a "neutral" defect. Such a defect is non-physical as it only affects the lifetime of carriers as predicted by Eq. (1.5) and not the doping or capacitance of the device due to trapped charge. Nevertheless, the ability to control carrier lifetimes through such a simple model can still be useful. SCAPS fails to converge for L_n greater than ~3 µm, but predicts a limiting value of $V_{oc} \approx 0.95\,\mathrm{V}$ for such diffusion lengths. CSVT material can reach at least 8 µm so even higher V_{oc} should be possible for optimized devices with surface passivation and antireflective coatings.

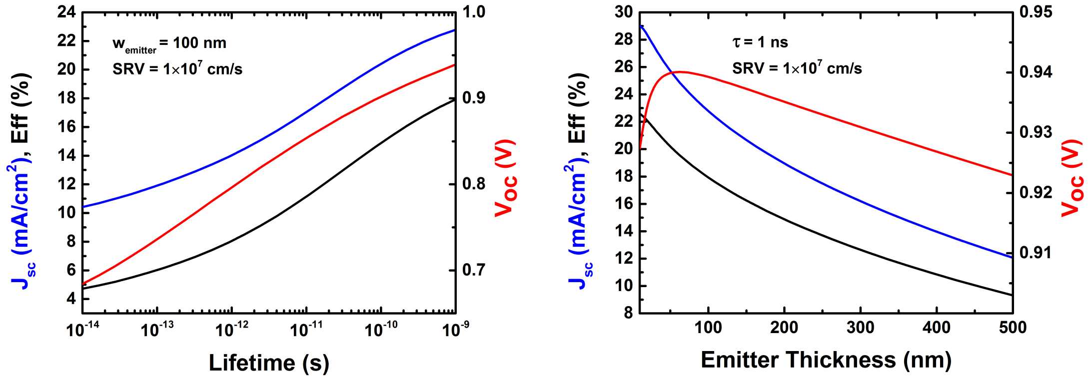

FIGURE 9. Simulations for an n^+p junction. Carrier densities are $n = 1 \times 10^{18}\,\mathrm{cm}^{-3}$ and $p = 1 \times 10^{17}\,\mathrm{cm}^{-3}$. Left: Variation of IV parameters with changing electron lifetime. Right: Variation of IV parameters with changing emitter thickness.

Bridge

Several different characterization techniques can be employed to study both individual films and multi-layer devices. These can be broadly classed as either materials or device characterization, where the former focuses generally on physical structure and chemical composition and the latter is concerned with electronic properties. The next chapter gives a brief background on several of the most important techniques used in this study.

CHAPTER III

CHARACTERIZATION METHODS

Portions of this chapter were taken from Boucher, J.W.; Miller, D.W.; Warren, C.W.; Cohen, J.D.; McCandless, B.E.; Heath, J.T.; Lonergan, M.C.; Boettcher, S.W. Optical response of deep defects as revealed by transient photocapacitance and photocurrent spectroscopy in CdTe/CdS solar cells. Solar Energy Materials and Solar Cells, 2014. It was written entirely by me with editorial assistance of my co-authors. The data was collected by me with assistance from D.W.M and C.W.W..

Materials Characterization

Optical microscopy and profilometry

Film surface morphology was measured using metalurgical microscopes equipped with optics for differential interference contrast (DIC) microscopy, also known as Normarski microscopy. In this mode, differences in optical path length are ultimately viewed as differences in the amplitude of light that reaches the objective of the microscope, giving the sample under inspection the appearance of being illuminated from the side. Reflected light DIC imaging works by passing light through a special prism which causes the light to be split into two orthogonal polarized beams, with one traversing a slightly different optical path. The two beams are brought together through a polarizer, and since the beams reflect off slightly different positions on the sample being imaged, they will interfere differently depending on gradients in the sample height.

Many of the surface defects which can form in GaAs films are surrounded by oval hillocks which are not visible in standard reflected-light microscopy but can readily observed using DIC imaging. An example of such defects is shown in 10, also highlighting the fact that oval defects are typically elongated along one of the cleavage planes of the substrate.

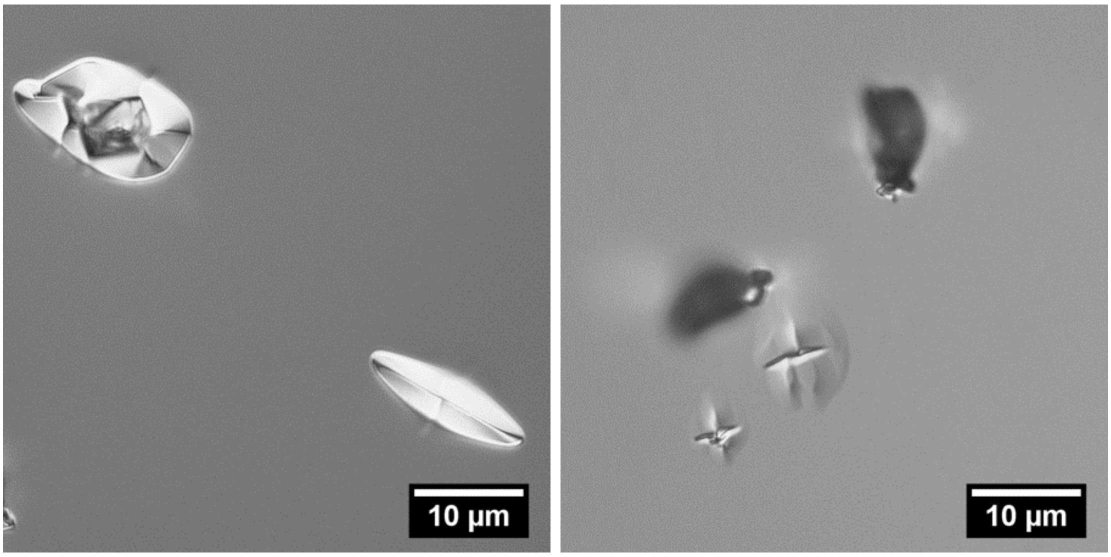

FIGURE 10. Oval defects in a GaAs film. Images are collected using DIC microscopy.

A similar method to DIC imaging is used in optical profilometry, where two coherent light beams are interfered and their interference pattern can be analyzed to quantitatively measure sample height variations. Films grown by CSVT are in contact with a quartz spacer, under which no growth can occur. This allows optical profilometry to be used to measure the thickness of homoepitaxially grown films which would otherwise be very difficult to measure.

Time-of-flight secondary ion mass spectroscopy

Elemental composition of films can be directly determined using ToF-SIMS, which operates by bombarding samples with charged particles and analyzing the secondary ions which are ejected from the sample. In a ToF-SIMS measurement, ions are first excited through a known potential, in the process gaining a kinetic energy

$$U = qV = \frac{1}{2}mv^2 \tag{3.1}$$

After being accelerated, the ions are then allowed to pass through a region without electric field, and their arrival times are measured by a detector. Since the column length is known, the velocity can be determined, and since the accelerating voltage is known, the ratio m/q can also be determined. The mass spectra are then analyzed assuming most of the species are singly charged.

Calculation of actual impurity concentrations requires knowledge of the relative sensitivity factor (RSF) with the relationship

$$C_i = RSF\frac{I_i}{I_m} \tag{3.2}$$

where C_i is the concentration of element i, and I_i and I_m are the ion intensities of the signal for element i and the *matrix* element, respectively. The matrix element should be a primary constituent of the material being measured, such that its intensity is large and its concentration does not change appreciably during sputtering. For GaAs, this is usually chosen to be As, though Ga can also be used (and the RSF depends on the matrix element chosen). The RSF also depends on the sputtering ion chosen, which can be either ${O_2}^+$ or Cs^+. Elements which are mostly ejected as negative ions have lower RSFs and better sensitivity under a Cs^+ due to their higher ion yield [36].

The Ion-ToF spectrometer used in this work is capable of both two- and three-dimensional mapping by destructively sputtering through films. This allows for correlation with microscopy of surface defects as well as depth profiling of interfaces between layers, as described in Chapter IV. Depth profiles are calibrated by measuring the total sputter depth using optical profilometry and assuming a constant sputter rate.

X-ray Diffraction

It is important to be able to probe the crystalline structure of III-V films, particularly when growing heteroepitaxial films which may have varying composition. This can be accomplished by measuring the diffraction of x-rays through the films, since the periodic structure of the lattice causes x-rays to be scattered with high intensities only at certain angles. In three dimensions, scattering of electromagnetic waves can be generally written as [37]

$$I(\boldsymbol{K}) = \frac{|A_0|^2}{R'^2}\Big|\sum_{G}\rho_{\boldsymbol{G}}\int e^{i(\boldsymbol{G}-\boldsymbol{K})\cdot\boldsymbol{r}}d\boldsymbol{r}\Big|^2 \tag{3.3}$$

where A_0 is the intensity of the incident plane wave, $R^{'}$ is the location of the detector, $\boldsymbol{G}$ is a reciprocal lattice vector, $\boldsymbol{K} = \boldsymbol{k} - \boldsymbol{k_0}$ is the difference between the incident and scattered waves, and $\boldsymbol{r}$ is the location at which the wave is scattered. $\rho_{\boldsymbol{G}}$ is called the structure factor which depends on the basis atoms that make up the crystal. The qualitatively important part of Eq. (3.3) is that the integral term can be assumed to be approximately zero except when $\boldsymbol{G} = \boldsymbol{K}$, which is called the Laue Condition. Thus, in an x-ray diffraction (XRD) experiment, a series of peaks can be obtained when the x-ray source and detected are aligned at certain angles with respect to the sample being measured.

A more conceptual picture of XRD was originally given by Bragg and is illustrated in Fig. 11. In this interpretation, diffraction peaks occur due to

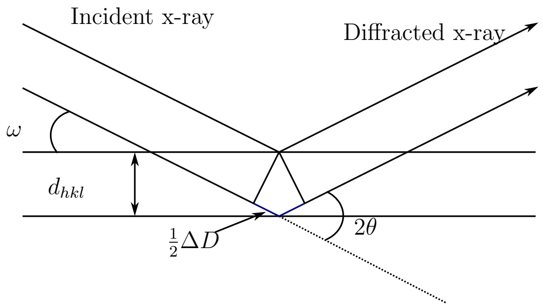

FIGURE 11. Illustration of an XRD experiment. The Bragg condition can be derived by considering the path length difference ΔD, between reflections of the adjacent crystal planes, as shown.

constructive interference due to reflection from adjacent lattice planes, similar to thin film interference. Constructive interference occurs where

$$\lambda = 2d_{hkl}\sin\theta \tag{3.4}$$

with $d_{hkl} = a/\sqrt{h^2+k^2+l^2}$ for a cubic system with lattice spacing a and for the crystal plane with miller indices h, k, and l.

For an epitaxial film, a “coupled” scan is usually performed in which the x-ray source and detector are moved together, changing θ while ω remains fixed and aligned to a certain crystal plane. For instance, for III-V films, substrates are most commonly cut near a [001] orientation so the {001} family of planes can be most easily observed. When films are grown heteroepitaxially, multiple peaks at different values of θ will usually be observed, and these can be used to determine the film composition if the lattice constant as a function of composition is known. After finding a given peak, ω can be scanned with fixed θ such that crystal planes with slight misorientations diffract the incident x-rays. This type of measurement is called a rocking curve. Generally, a wider the rocking curve suggests higher amounts of crystalline disorder.

Device Characterization Methods

Current-Voltage Characteristics

Current-voltage (I-V) curves obtained both under illumination and in the dark provide useful information on the performance of solar cell devices. Under illumination, the efficiency of the solar cell is calculated as the maximum power output divided by the power input. Under one-sun conditions this is $\eta = \frac{J_{mp}V_{mp}}{100\,\mathrm{mW\,cm^{-2}}}$ for the current density and voltage, J_{mp} and V_{mp} at maximum power point. Another useful quantity is the fill factor (FF), which is defined as $FF = \frac{J_{mp}V_{mp}}{J_{sc}V_{oc}}$ and is impacted heavily by factors such as series and shunt resistance. Eq. (1.3) can be modified to include the effects of additional current paths, such as recombination in the depletion region, by adding an *ideality factor*, m, such that Eq. (1.3) becomes:

$$J = J_0 \left[exp\left(\frac{qV}{mkT} \right) - 1 \right] - J_{sc} \tag{3.5}$$

The case where $m = 2$ is derived by assuming that generation and recombination in the depletion region are the dominant source of current, while values between $m = 1$ and $m = 2$ occur when both diffusion and recombination currents are significant. It is common for devices to have $m = 2$ dominating at low bias [38]. An example of two different diodes is shown in Fig. 12. The fact that the second diode has a region at low bias with $m = 2$ suggests that significant recombination centers exist near the Au/GaAs interface.

In addition to the ideality factor, it is important to consider the effects of series resistance and parallel conduction paths through a solar cell. Series resistance in GaAs cells is usually determined by the contact metalization rather than the properties of films, so it is desirable to correct IV curves for the series resistance. In the simplest

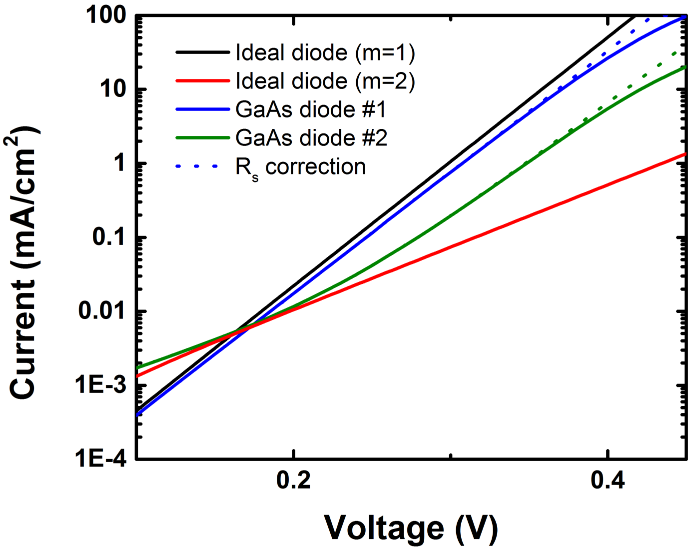

FIGURE 12. Diode IV curves. Curves are for two Au/n-GaAs diodes and ideal diode curves with $m = 1$ and $m = 2$.

case, the series and shunt resistances are independent of voltage and Eq. (3.5) can be written as

$$J = J_0 \left[exp\left(\frac{q\,(V - RJ)}{mkT} \right) - 1 \right] + G(V - RJ) - J_{sc} \tag{3.6}$$

where R is the series resistance and G is the shunt conductance. In practice, the region of interest for an I-V curve is $V > kT/q$ such that $exp(\frac{qV}{mkT}) >> 1$ and so Eqs. (1.3), (3.5) and (3.6) are often written without the "-1" factor.

There are numerous methods for analyzing I-V curves for PN junctions, and reviews of common techniques are given by Hegedus [39] and McIntosh [40]. The series resistance is first extracted since it is usually easy to decouple from the other parameters and can have a large impact on the fill factor of the cell. In this work, the series resistance is calculated by computing the derivative, which follows from

Eq. (3.6)

$$\frac{dV}{dJ} = \frac{1 + \frac{J_0 q}{mkT} R \exp\left(\frac{q}{mkT}(V - RJ)\right) + GR}{\frac{J_0 q}{AkT} \exp\left(\frac{q}{mkT}(V - RJ)\right) + G} \tag{3.7}$$

$$\approx R + \frac{mkT}{q} \left[J_0 0 \exp\left(\frac{q}{AkT}(V - RJ)\right)\right]^{-1} \tag{3.8}$$

$$\approx R + \frac{mkT}{q} \left[J + J_{sc}\right]^{-1} \tag{3.9}$$

The last two lines assume that the shunt conductance is negligible and J_0 is small compared to J and J_L. From this, series resistance is found by plotting $(J + J_{sc})^{-1}$ against $\frac{dV}{dJ}$, as shown in Fig. 13 for a dark IV curve. The shunt conductance can be extracted by calculating $G = dJ/dV\Big|_{V=0}$. In practice, there are usually two complications that arise with this calculation. First, the slope near $V = 0$ is typically very noisy due to the small currents being measured, or due to the variation of the

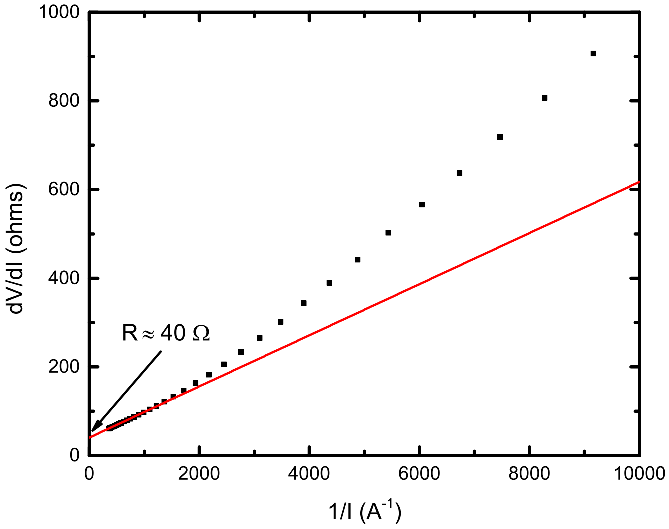

FIGURE 13. Series resistance extraction. Shown is a plot of inverse current against dV/dI for cell S3-140122 (CSVT emitter on VGF wafer absorber) showing the series resistance as the y-axis intercept of the fit line.

light intensity when measuring under solar simulation. Second, shunts do not usually have an ohmic characteristic but instead follow a rectifying behavior in reverse bias. This appears as a peak in the dJ/dV plot, rather than a trend toward a constant value, as shown in Fig. 14. In practice this is not usually a problem as when shunt resistances are high the correction to the IV curve is negligible.

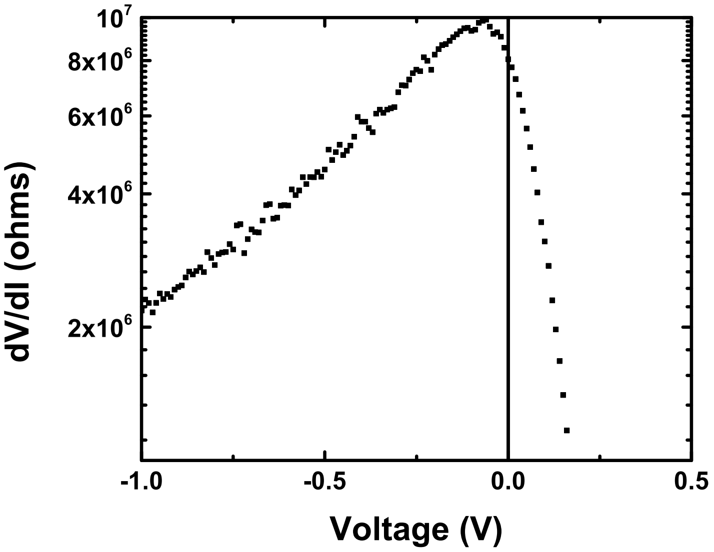

FIGURE 14. Shunt resistance extraction. Shown is a plot of resistance as a function of voltage for cell S3-140122. The apparent shunt resistance is $G^{-1}\approx 8\,\mathrm{M\Omega}$ but has an approximately exponential behavior in reverse bias.

Quantum Efficiency

The external quantum efficiency (EQE, or Φ_{ext}) of a device is simply the number of carriers collected per photon incident on the device. EQE is measured as a function of photon wavelength or energy by using a scanning monochromator and measuring the current output of the device. Since monochromators output relatively low light flux, the light is usually chopped and the (small) output current is measured using a lock-in amplifier. Current is converted to EQE by measuring a reference cell of known

EQE such that

$$\Phi_{ext,dev} = \frac{J_{dev}}{J_{ref}} \times \Phi_{ext,ref} \tag{3.10}$$

Another useful quantity is the internal quantum efficiency (IQE, or Φ_{int}), which is simply the EQE neglecting photons which are transmitted or reflected. Since transmission is nearly zero for the devices in this study which are grown on optically thick substrates, IQE can be calculated as

$$\Phi_{int} = \frac{\Phi_{ext}}{1 - R} \tag{3.11}$$

where R is the reflectance.

In a *pn*-junction, three primary current contributions can be identified: (1) hole current in the *n*-type layer, (2) electron current in the *p*-type layer (3) depletion region current. The depletion region IQE is often taken to be 1 [17], and so only depends on the depletion width and absorption coefficient. The other two contributions are due to diffusion of minority carriers and depend on their diffusion lengths. Additionally, bare GaAs has a high density of surface states which can heavily impact the IQE when light is absorbed near a surface. This is parameterized by a quantity called surface recombination velocity (SRV). SRV is part of a boundary condition specifying that, at steady-state, the rate of recombination at the surface has to equal the rate of diffusion of carriers to the surface. For instance, for holes [17]:

$$qD_p \frac{dp_n}{dx}\bigg|_{x=0} = qS_p[p_n(0) - p_{n0}] \tag{3.12}$$

where S_p is the surface recombination velocity for holes. The devices fabricated in this work are all unpassivated and have low quantum efficiency in the short wavelength part of the spectrum which is absorbed near the front of the cell.

SRV can be limited by chemically passivating the GaAs surface (that is, changing the surface bonds such that recombination centers are minimized). Surface passivation of GaAs is difficult, however, and one of the most effective methods is through the use of sulfur-containing chemicals. Though sulfide layers can provide excellent passivation [41], these layers are not particularly stable in air [42] and thus are not suitable for PV devices. Instead of chemical passivation, it is therefore more common to deposit layers of semiconductors that generate electric fields which reflect minority carriers. For the top layer of the solar cell, this must be a "window" layer with high optical transparency, while the bottom layer can simply contain a more highly-doped region (called a"back surface field").

Hall Effect

For samples on opposite carrier type substrates or semi-insulating substrates, combined Van der Pauw resisitivity and Hall effect measurements can be used for rapid characterization of carrier concentration and mobility. To characterize the background dopant concentration in films grown in the CSVT reactor, films are grown from nominally undoped sources on undoped substrates. The wafers used for this purpose both always have resisitivy $>1 \times 10^7\,\Omega$ and though they are labelled as undoped by the manufacturer they probably have a low concentration of a shallow acceptor as the primary impurity. A compensating acceptor is needed since GaAs grown from a melt otherwise is n-type semiconducting due to native donor levels which have energy levels near mid-gap. A common acceptor used for this purpose is

C, which does not appear to transport appreciably in our reactor (despite the use of graphite heaters); in any case, films grown from undoped material in our reactor are invariably n-type, so the dominant impurities probably do not come from residual doping of the commercial GaAs source material.

The lowest carrier concentrations achieved using our CSVT reactor are $\sim 4 \times 10^{15}\,\mathrm{cm}^{-3}$, though the mobilities for lightly-doped material tend to be well below the theoretical values for uncompensated GaAs [43]. This suggests that these samples were substantially compensated, likely due to contamination of the porous graphite heaters or other reactor parts. We have shown that sulfur is the most common unintentional dopant in our reactor, originating from the graphite heaters [28], though impurities below $1 \times 10^{17}\,\mathrm{cm}^{-3}$ can be difficult to detect using ToF-SIMS. A few compensating acceptor levels have been detected using DLTS and this is discussed in Chapter V.

To characterize the effects of various cleaning procedures on the background dopant concentration, a series of control films have been grown from undoped wafers onto undoped GaAs substrates. The results of the various procedures are shown in Fig. 15. Most notably, the carrier concentration could only be decreased below $1 \times 10^{17}\,\mathrm{cm}^{-3}$ by replacing the quartz reaction tube. Some of the other cleaning processes appear to introduce contaminants as well, such as the use of uncleaned Si wafers as a barrier between the porous graphite and the GaAs source and substrate. Acid cleaning the graphite may leave behind residual impurities even after rinsing and soaking in $18.2\,\mathrm{M}\Omega$ H_2O ten times and baking in an oven at 100 °C, though the temperature cycling up to 850 °C appears to be sufficient to drive off most of the contaminants. Interestingly, growing with no carrier gas flow during either the growth phase or during the entire ramp and growth did not decrease the carrier concentration, though this should limit the amount of gas-phase impurities which could reach the reaction zone from the tube upstream. This suggests that contaminants may be deposited on the quartz tube relatively near to the heaters, and become volatile and diffuse into the reaction zone once the tube reaches a high enough temperature.

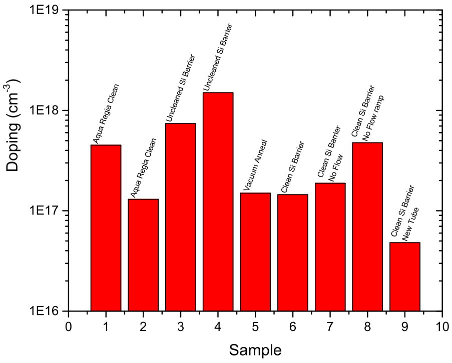

FIGURE 15. Hall background impurity characterization. Shown are carrier concentrations for films grown from undoped GaAs wafers under various reactor conditions designed to minimize background impurities.

Mobilities of these GaAs films are shown in Fig. 16 as black squares. Also shown are empirical mobility curves for uncompensated n- and p-GaAs from Ref. [43] and theoretical curves for compensated n-GaAs from Ref. [44]. At low dopant concentrations, the experimental data deviates significantly from the theoretical curve, indicating a significant amount of compensation. Likely compensating impurities are Cu, Fe, and Cr since the graphite heaters are connected using Cu wires and stainless steel screws. DLTS provides direct evidence of at least Cu and Fe, as discussed in Chapter V.

Capacitance-Voltage

As explained in Chapter I, the depletion capacitance for a one-sided junction depends on the free carrier concentration and the potential across the device.

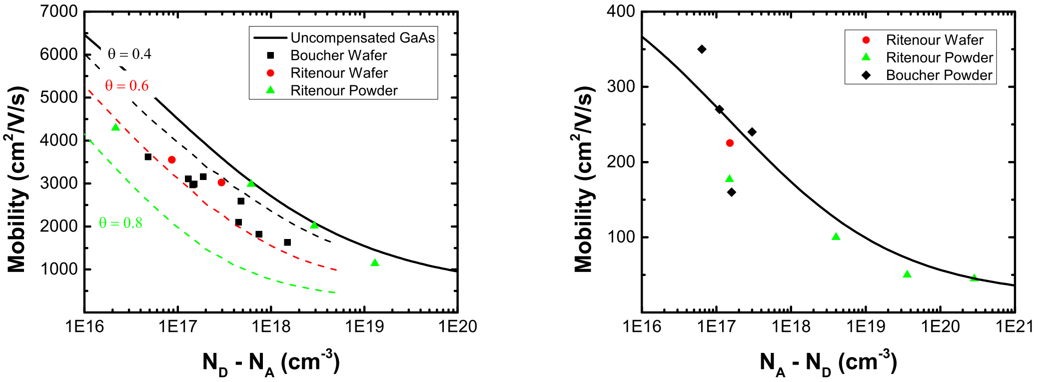

FIGURE 16. *n*- and *p*-type Hall mobilities for films grown in our reactor. Data labeled Ritenour are reproduced from Ref. [28]

Combining equations Eq. (1.7) and Eq. (1.8) and taking a derivative produces

$$\frac{d(1/C^2)}{dV} = \frac{1}{A^2}\frac{2}{\varepsilon q N_D} \tag{3.13}$$

Therefore a plot of $1/C^2$ against applied bias (also called a Mott-Schottky plot) produces a line with slope inversely proportional to N_D. Furthermore, V is given by the total potential across the device, which is the sum of the applied bias and built-in voltage. For that reason, the intercept of the line gives the built-in voltage. This is illustrated for a Au/n-GaAs diode in Fig. 17.

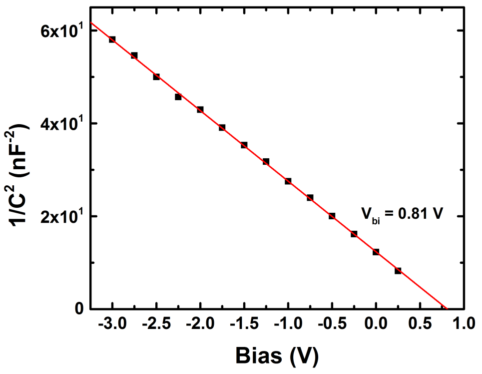

FIGURE 17. Mott-Schottky plot for a Au/*n*-GaAs diode with constant doping.

For devices in which the dopant concentration is not constant, the Mott-Schottky plot can replaced by a free carrier profile, using Eq. (1.7) to calculate the depletion edge position. In practice, one must be careful in interpreting changes in the Mott-Schottky slope. The measurement of depletion capacitance itself is often suspect as it requires an interpretation of the complex impedance of the entire measurement circuit. For instance, it is common to model the device as an ideal capacitor in parallel with an ideal resistor. For cells with low shunt resistance, however, this assumption can be invalid as the series resistance can become non-negligible when current through the cell increases. To further complicate matters, the shunt resistance is often non-ohmic, so at high reverse bias the Mott-Schottky slope may appear to change when in reality the circuit model used to extract depletion capacitance is simply no longer valid. For the same reason, capacitance-voltage (CV) profiles are usually not collected very far into forward bias where conductance of the cell increases.

In addition to the complications described above, deep states can distort the CV profile due to slow charge trapping and emission. This is described in detail by Heath and Zabierowski [45] but will be summarized here. In CV profiling, the capacitance is probed using a high frequency (usually between 1×10^3–1×10^6 Hz) perturbing voltage, while the "D.C." bias is varied much more slowly. Occupation of states at the edge of the band gap can in most cases change rapidly enough to follow the probing voltage, but states near the center of the band gap may only change their occupation in response to the slower D.C. bias sweep. Thus, the interpretation of a CV profile as a profile of the dopant density may be incorrect as the slope may change as charge is trapped or emitted from deep defect states. A modification of the CV technique was developed by Cohen [46] which requires changing the magnitude of the AC probing voltage. This technique, drive-level capacitance profiling (DLCP), allows extraction of only the shallow defect levels which can respond at the AC frequency. In the GaAs devices described in this study, the density of deep defects that can respond to the CV profiling method is typically too small to affect the profile. A comparison of DLCP and CV profiles is shown in Fig. 18 for a device with $N_D = 6 \times 10^{15}\,\mathrm{cm}^{-3}$.

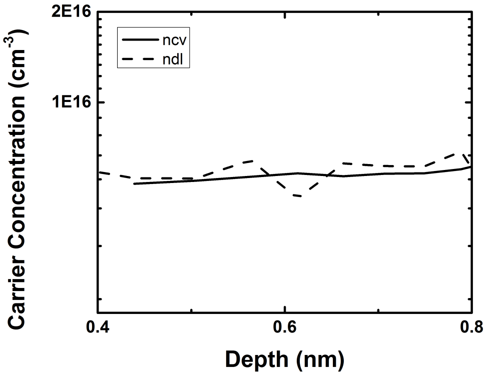

FIGURE 18. DLCP and CV profiles for Au/n-GaAs diode

Deep-level Transient Spectroscopy

Deep-level transient spectroscopy (DLTS) was developed by Lang in 1974 [47] to characterize defects with electronic states in the band gap of semiconductors. At its core, DLTS simply measures the transient changes in the capacitance (or less commonly current) of a one-sided junction which are due to charge emission from defect states. Usually, a voltage pulse in the forward bias direction is applied to change the occupation of defect states, after which the device is held in reverse bias to observe capacitance transients. As the temperature is decreased, these emission processes become slower, and by characterizing the changing emission time constant the apparent energetic location of traps can be extracted.

A DLTS experiment requires a capacitance meter that can operate at high frequency (typically 100 kHz or 1 MHz) and in modern systems a digitizing oscilloscope is used to record and store each capacitance transient. The temperature- and rate-window dependent DLTS signal is given by:

$$S(T) = H \int_{t_1}^{t_2} w(t)C(t)dt \tag{3.14}$$

Where H is a conversion factor to translate oscilloscope values to capacitance (i.e., it has units of pixels/F). Following the filling pulse, the capacitance as a function of time, for a one-sided junction with low trap density, is given for an n^+p junction or n-type Schottky diode by

$$C(t) \approx C_\infty \left[1 - \frac{N_T}{2N^-} \exp(-e_p t)\right] \tag{3.15}$$

Where N_T is the trap density, N^- is the space charge (doping) and e_p is the hole emission rate for the trap. The emission rate is derived from a detailed balance consideration (emission and capture rates for each process must be equal in thermal equilibrium) and from Fermi-Dirac statistics for trap occupancy, with the result

$$e_p = \sigma_p \langle v_p \rangle \frac{g_1}{g_0} N_v \exp(-\frac{E_t - E_v}{kT}) \tag{3.16}$$

with σ_p the capture cross section, $\langle v_p \rangle$ the RMS hole thermal velocity, and g_1 and g_0 the electron occupied and unoccupied degeneracy of the trap (usually taken as equal). Both N_v and $\langle v_p \rangle$ are temperature-dependent with a combined proportionality of T^2, while σ_p may be exponentially dependent on temperature (assuming a multiphonon emission process [48]):

$$\sigma_p(T) = \sigma_\infty \exp(-\frac{\Delta E_\sigma}{kT}) \tag{3.17}$$

The temperature dependence is then combined to form

$$e_n(T) = \gamma T^2 \sigma_{pa} \exp(-\frac{E_{pa}}{kT}) \tag{3.18}$$

with σ_{pa} the *apparent* capture cross section (the actual capture cross section extrapolated to $T = \infty$), and E_{pa} the *apparent* activation energy, $(E_c - E_t) + \Delta E_\sigma$.

The weighting function used for this study is the linear ramp, given by

$$w(t) = \left[\frac{-2t}{t_2 - t_1} + \frac{2t_1}{t_2 - t_1} + 1\right] \tag{3.19}$$

Note that this function integrates to zero over t_1 to t_2. We further define $S'(T)$ as the DLTS signal with units F s, that is

$$\begin{aligned}
S'(T) &= \int_{t_1}^{t_2} w(t)C(t)dt \\
&= C_\infty \int_{t_1}^{t_2} \left[\frac{-2t}{t_2 - t_1} + \frac{2t_1}{t_2 - t_1} + 1\right] \left[1 - \frac{N_T}{2N^-} \exp(-e_p t)\right] dt \\
&= C_\infty \left[\int_{t_1}^{t_2} w(t)dt - \frac{N_T}{2N^-} \int_{t_1}^{t_2} \left[\frac{-2t}{t_2 - t_1} + \frac{2t_1}{t_2 - t_1} + 1\right] \exp(-e_p t)\right] \\
&= \frac{C_\infty N_T}{2N^-} \left[\frac{2}{t_2 - t_1} \int_{t_1}^{t_2} t \exp(-e_p t)dt - \left(\frac{2t_1}{t_2 - t_1} + 1\right) \int_{t_1}^{t_2} \exp(-e_p t)dt\right] \\
&= \frac{C_\infty N_T}{2N^-} \left[\frac{-2}{{e_p}^2(t_2 - t_1)} \left[e^{-e_p t_2}(1 + e_p t_2) - e^{-e_p t_1}(1 + e_p t_1)\right]\right. \\
&\left. -\frac{1}{e_p} \left(\frac{2t_1}{t_2 - t_1} + 1\right) (e^{-e_p t_1} - e^{-e_p t_2})\right]
\end{aligned} \tag{3.20}$$

An alternative approach, which is conventionally used [49] is to use a coordinate transformation $t \rightarrow t + t_1$ such that $C'(t) = C(t + t_1)$ and $w'(t) = w(t + t_1)$. This simplifies the calculation somewhat. In that case,

$$\begin{aligned}
S'(T) &= \int_0^{t_m} C'(t)W'(t)dt \\
&= \int_0^{t_m} C_\infty \left[1 - \frac{N_T}{2N^-}\exp(-e_pt_1)\exp(-e_pt)\right] w'(t)dt \\
&= \frac{-C_\infty N_T}{2N^-}\exp(-e_pt_1)\left[\frac{2t}{t_m}\left(\frac{1+e_pt_m}{{e_p}^2}\exp(-e_pt_m) - \frac{1}{{e_p}^2}\right) - \frac{1}{e_p}\exp(-e_pt_m) + \frac{1}{e_p}\right] \\
&= \frac{-C_\infty N_T}{2N^-}\frac{\exp(-e_pt_1)}{e_p} \\
&\left[\frac{2}{t_me_p}\left(\exp(-e_pt_m) + e_pt_m\exp(-e_pt_m) - 1\right) - \left(\exp(-e_pt_m) - 1\right)\right]
\end{aligned} \tag{3.21}$$

where $t_m = t_2 - t_1$ is the total integration time. If t_1 is taken to be zero, then a numerical calculation shows that $S'(T)$ has a maximum where $t_m \approx \frac{2.688}{e_p}$. In practice it might be desirable to have t_1 be non-zero due to the instrumentation (e.g., since it takes time for the capacitance meter to recover following the filling pulse). However, if the condition $e_pt_1 << 1$ is not met, then the relationship between t_m and e_p is not constant, leading to error in the Arrhenius fit if it is not somehow corrected. This also manifests as a distortion in the DLTS peaks, as shown in the simulations in Fig. 19.

With the preceding assumptions, the maximum signal is given by Eq. 3.20 as

$$\begin{aligned}
S'_{max} &= S'(T_{max}) \\
&= \frac{C_\infty N_T}{2N^-}\left[\frac{-2}{2.688e_p}\left[e^{-e_pt_2}(1+e_pt_2) - e^{-e_pt_1}(1+e_pt_1)\right] - \frac{1}{e_p}\left(\frac{2t_1e_p}{2.688}+1\right)\left(e^{-e_pt_1} - e^{-e_pt_2}\right)\right] \\
&= \frac{C_\infty N_T}{2N^-}\left[\frac{-2}{2.688e_p}\left[A(t_1)\right] - \frac{1}{e_p}\left(\frac{2t_1e_p}{2.688}+1\right)\left(B(t_1)\right)\right]
\end{aligned} \tag{3.22}$$

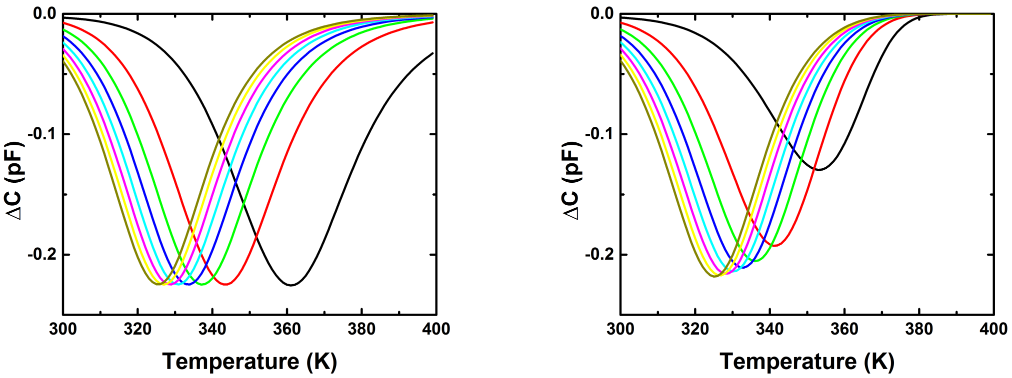

FIGURE 19. Simulated DLTS peaks. Curves are calculated from Eq. (3.21) for a 0.83 eV defect with various t_m with Left: $t_1 = 0$, Right: $t_1 = 1\,\text{ms}$.

Where

$$\begin{aligned} A(t_1) &= e^{-2.688} e^{-e_p t_1}(1 + 2.688 - e_p t_1) - e^{-e_p t_1}(1 + e_p t_1) \\ &\approx -0.75 \end{aligned} \tag{3.23}$$

and

$$\begin{aligned} B(t_1) &= e^{-e_p t_1} - e^{-2.688} e^{-e_p t_1} \\ &\approx 0.93 \end{aligned} \tag{3.24}$$

The approximation assumes that $e_p t_1 \ll 1$. Carrying out the arithmetic, the maximum signal is approximated

$$S'_{max} \approx -0.371 \frac{C_\infty N_T}{e_p N^-} \tag{3.25}$$

Note that the signal calculated from the raw data must be divided by H since $S = HS'$.

A slight correction—often called the “lambda” correction—to the above formula should be used in cases where either the position where the trap level crosses the Fermi level is not near the depletion edge or where the depletion width at quiescent reverse bias is not much greater than the depletion depth during the filling pulse [50]. In those cases

$$S'_{max} \approx -0.371 \frac{x_1^2 - x_2^2}{x_d^2} \frac{C_\infty N_T}{e_p N^-} \tag{3.26}$$

where x_2 and x_1 are the positions (with $x = 0$ at the junction) where the trap crosses the fermi level during the filling pulse and in quiescent bias, respectively, and x_d is the depletion edge position in quiescent bias. x_1 and x_2 can be calculated with respect to the transition distance from the depletion edge at their respective biases:

$$\lambda = \left\{ \frac{2\epsilon\epsilon_0}{e^2 N_d} (E_F - E_t) \right\}^{\frac{1}{2}} \tag{3.27}$$

such that, e.g., $x_2 = x_0 - \lambda$ with x_0 the depletion edge position during the filling pulse. The trap level can be approximated as the activation energy of the defect extracted from DLTS (though strictly speaking this is not exactly the trap level since the Arhennius plot gives the enthalpy and not the Gibb’s free energy). The Fermi level can be calculated from the free carrier density given by a CV measurement.

Experimental Considerations

Accurate measurement of temperature is extremely important in DLTS. Temperature sensors should be mounted as close as possible to the device under test, or at a location on the stage where the temperature is known to be identical. In these studies, an internal thermocouple is embedded within the temperature-controlled stage, but even the temperature gradient across the metal stage is enough to cause error in the measurement of E_a and σ_a. Thus a separate thermocouple is clamped to the surface of the device to provide a more accurate measurement. A comparison between data points extracted from the two different sensor locations is shown in Fig. 20.

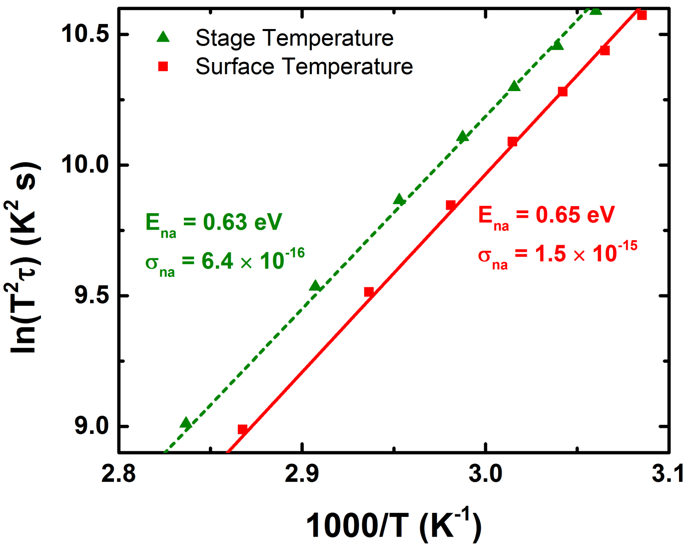

FIGURE 20. Comparison of Arrhenius fits for different sensor locations. Data shown is for a diode made from Au on Te-doped n-GaAs wafer. At these temperatures, the error caused by the temperature gradient between the stage and sample most heavily impacts the value of capture cross section.

As mentioned in the preceeding section, choosing to start the integration at some time after the end of the pulse can introduce artifacts into the Arrhenius fits. This is shown in Fig. 21. For small values of t_1, the Arrhenius plots can still appear to be linear but with overestimated E_a. For that reason all of the Arrhenius plots in this study are generated with t_1 coinciding with the end of the filling pulse.

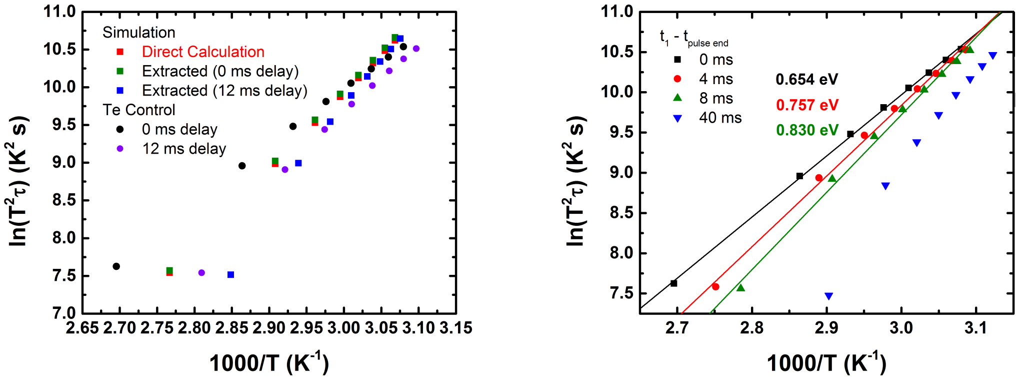

FIGURE 21. Effect of integration start time. Left: Experimental data for a Au/n-GaAs diode ($1 \times 10^{17}\,\mathrm{cm}^{-3}$ Te-doped wafer) and simulated data for trap parameters extracted from simulated data with 12 ms delay. The direct calculation differs slightly as the data points are extracted using Gaussian fits to the simulated data. Right: Experimental data and Arrhenius fits given different values of t_1 showing the significant change in extracted activation energies.

Transient Photocapacitance and Photocurrent Spectroscopy

A logical extension of the DLTS technique is to apply the measurement under various states of illumination. In minority carrier DLTS, for instance, above gap light is provided as a replacement or in addition to voltage pulses such that minority carrier traps are also filled. Extending this method further, a monochromator can be used to characterize the energies at which optical transitions occur. This is the basis for transient photocapacitance (TPC) and photocurrent (TPI) spectroscopy.

TPC was initially developed to characterize sub-bandgap defects in doped amorphous silicon [51]. Since then, the technique has been applied to a variety of materials such as Cu(In,Ga)Se_2 (CIGS) [52], transparent oxide semiconductors [53], and more recently $Cu_2ZnSn(Se,S)_4$ (CZTS) [54]. TPC spectra are similar to sub-gap absorption spectra. However, because the signal is due to carrier dynamics in the depletion region the spectra can be obtained in a complete PV device, without measuring transmittance. Furthermore, the sign of the signal indicates whether a majority or minority carrier transition is responsible for the absorption.

Unlike DLTS, TPC and TPI use monochromatic light to enhance the emission of carriers during the transient. After collecting a transient with the light on, a second transient is immediately collected under the same conditions but with the light removed. The actual TPC signal is then calculated as

$$P_{raw} = \int_{t_1}^{t_2} V_{light}(t)dt - \int_{t_1}^{t_2} V_{dark}(t)dt \tag{3.28}$$

where $V_{light/dark}(t)$ represent the transient capacitance signals (measured as a voltage from the lock-in amplifier output), with $t = 0$ corresponding to the end of each filling pulse. This raw signal must then be normalized by the incident light flux, and care must also be taken to ensure that the signal varies linearly with light flux.

Increased carrier emission in the light increases the change in capacitance and therefore the signal. Thus, the signal depends on the number of transitions that are accessible for a given optical energy; for instance, transitions between the valence band and defect band produce a positive signal contribution of the form

$$P_{v-d}(E_{opt}, T) = K(T) \int_{E_v+E_e}^{E_v+E_{opt}} |\langle i|\, ex\, |f\rangle|^2 g_d(E) g_v(E - E_{opt}) dE \tag{3.29}$$

where g_d and g_v are the density of states in the defect band and valence band, respectively and $|\langle i|\, ex\, |f\rangle|$ is the optical matrix element. The factor E_e represents the depth at which holes are able to escape thermally during the measurement, as described in [52]. The proportionality constant $K(T)$ encompasses any effects that are not dependent on the optical energy. Since the emission of majority carriers causes the depletion region to contract, while the emission of minority carriers causes it to expand, the overall signal is proportional to $p - n$, the number of majority carriers minus the number of minority carriers emitted. The TPI measurement is nearly identical except when measuring current all the terms contributing to the signal are positive (i.e., electrons emitted from the defect to the conduction band have a positive contribution in TPI but negative in TPC). The TPI signal therefore is roughly proportional to $p + n$, though different spatial sensitivities for majority carrier and minority carrier collection may affect this value if carriers are not generated uniformly throughout the depletion region [55].

Bridge

The characterization techniques described in this chapter are applied to homojunction solar cell devices in the next chapter.

CHAPTER IV

DEVICE PERFORMANCE RESULTS

Portions of this chapter were taken from Boucher, J.W.; Ritenour, A.J.; Greenaway; A.L., Aloni, S.; and Boettcher, S.W. Homojunction GaAs Solar Cells Grown by Close Space Vapor Transport. Proc. 40th IEEE Photovolt. Spec. Conf., 2014. It was written entirely by me with editorial assistance of my co-authors. Some of the data was collected with A.J.R.

Portions of this chapter were also taken from Boucher, J. W.; Greenaway, A. L.; K. E. Egelhofer, K. E.; Boettcher, S. W. Analysis of performance-limiting defects in pn junction GaAs solar cells grown by water-mediated close-spaced vapor transport epitaxy. Accepted manuscript in Solar Energy Materials and Solar Cells, 2016. It was written entirely by me with editorial assistance of my co-authors. Some of the data was collected by K.E.E. under my direction.

The lock-in thermography image of a GaAs cell was collected by Steve Johnston at NREL.

Early Device Results

Initial characterization of films grown in our CSVT reactor was performed using photoelectrochemical (PEC) cells. For those experiments, electrodes were fabricated with a metalized ohmic back contact, while the front contact was made to an electrolyte solution containing a redox couple of known concentration. Such a cell behaves essentially like a semitransparent Schottky diode, and so IV, CV, and QE measurements can be performed. While the V_{oc} in these cells is limited by a high density surface states which pin the Fermi level [56], the photocurrent and QE are

TABLE 1. Films grown and fabricated into solid state solar cells.

Film Number	T_{src} (°C)	T_{sub} (°C)	**Source Doping**($\mathrm{cm^{-3}}$)	**Substrate** ($\mathrm{cm^{-3}}$)	**Notes**
1	850	830	Te $1 \times 10^{18}\,\mathrm{cm^{-3}}$	Zn $1 \times 10^{18}\,\mathrm{cm^{-3}}$	
2	850	830	Te $1 \times 10^{18}\,\mathrm{cm^{-3}}$	Zn $1 \times 10^{18}\,\mathrm{cm^{-3}}$	
3	845	830	Te $1 \times 10^{18}\,\mathrm{cm^{-3}}$	Zn $1 \times 10^{18}\,\mathrm{cm^{-3}}$	
4	850	830	Te $1 \times 10^{18}\,\mathrm{cm^{-3}}$	Zn $1 \times 10^{18}\,\mathrm{cm^{-3}}$	
5	850	830	Te $1 \times 10^{18}\,\mathrm{cm^{-3}}$	Zn $1 \times 10^{18}\,\mathrm{cm^{-3}}$	
6	850	830	Te $1 \times 10^{18}\,\mathrm{cm^{-3}}$	Zn $1 \times 10^{17}\,\mathrm{cm^{-3}}$	
7	850	830	Te $1 \times 10^{18}\,\mathrm{cm^{-3}}$	Zn $1 \times 10^{17}\,\mathrm{cm^{-3}}$	Etched Substrate
8	850	830	Ge $1 \times 10^{18}\,\mathrm{cm^{-3}}$	Zn $1 \times 10^{17}\,\mathrm{cm^{-3}}$	
9	850	830	Ge $1 \times 10^{18}\,\mathrm{cm^{-3}}$	Zn $1 \times 10^{17}\,\mathrm{cm^{-3}}$	On etched CSVT film
10	760	720	Te $1 \times 10^{18}\,\mathrm{cm^{-3}}$	Zn $1 \times 10^{17}\,\mathrm{cm^{-3}}$	
11	780	720	Te $1 \times 10^{18}\,\mathrm{cm^{-3}}$	Zn $1 \times 10^{17}\,\mathrm{cm^{-3}}$	
12	800	740	Te $1 \times 10^{18}\,\mathrm{cm^{-3}}$	Zn $1 \times 10^{17}\,\mathrm{cm^{-3}}$	
13	820	760	Te $1 \times 10^{18}\,\mathrm{cm^{-3}}$	Zn $1 \times 10^{17}\,\mathrm{cm^{-3}}$	

comparable to what is expected in a solid-state device. In particular, fitting the long-wavelength QE region to the Gärtner model [57] yielded minority carrier diffusion lengths as high as 3 µm for *n*-type material and 8 µm for *p*-type material [28].

The first series of solid-state devices was fabricated with only the emitter deposited by CSVT and the *p*-type wafer substrate acting as the absorber. These film growths are summarized in table 1. Initially, all films were grown on cleaved pieces of epi-ready wafers with no surface treatment, except for film 7 for which a 30 s etch in 10:1:0.5 H_2O:NH_4OH:H_2O_2 was performed prior to film growth. This was subsequently adopted as a standard processing step, followed by rinsing and spin-drying with H_2O and isopropanol (IPA). There was no deterioration in device performance for this sample, and the sequence of etching and rinsing appears to minimize pinholes which can form due to dust. Films 1-5 gave similar average IV characteristics, with $V_{oc} = 490 \pm 40\,\mathrm{mV}$, $J_{sc} = 7.80 \pm 0.65\,\mathrm{mA\,cm^{-2}}$, $FF = 62.0 \pm 2.2\,\%$, and $\eta = 2.4 \pm 0.2\,\%$. The variation in these parameters is largely due to the varying emitter thickness (200-300 nm as measured by stylus and optical profilometry), which is influenced by the temperature gradient and source/substrate

TABLE 2. Average IV characteristics of devices fabricated from films 6-13.

Film	V_{oc} **(mV)**	J_{sc} **(mA cm^{-2})**	η(%)	FF **(%)**
6	845 ± 44	7.9 ± 0.6	4.8 ± 0.7	72 ± 7
7	872 ± 8	8.5 ± 0.4	5.5 ± 0.1	75 ± 2
8	402 ± 91	5.7 ± 0.6	1.3 ± 0.2	60 ± 8
9	320 ± 153	6.9 ± 1.3	1.1 ± 0.6	46 ± 7
10	834 ± 42	12.3 ± 0.2	7.1 ± 0.7	69 ± 4
11	868 ± 35	8.3 ± 0.8	4.8 ± 1.9	64 ± 23
12	863 ± 35	11.9 ± 0.5	7.6 ± 0.4	74 ± 2
13	783 ± 20	10.7 ± 0.8	5.7 ± 0.4	68 ± 1

spacing. Transmission line measurements (TLM) on some of the films yielded resistivities of 0.005 - 0.007 cm, which corresponds to a carrier concentration of 2×10^{17}–$3 \times 10^{17}\,\mathrm{cm}^{-3}$ for uncompensated n-GaAs [43, 58] Since this is lower than the source doping, it suggests that the films may be compensated by Zn diffusion from the substrates (which are doped $1 \times 10^{18}\,\mathrm{cm}^{-3}$ for these films).

Since the IV characteristics were very similar, films 6-13 were grown with much larger changes in the growth parameters including the use of both a different source and substrate. A lower p-type doping level for the substrate was expected to improve the emitter quality by minimizing diffusion of Zn. We also grew one Ge-doped emitter on a Zn-doped CSVT film with a known diffusion length $> 5\,\mu\mathrm{m}$ (film 9). The IV parameters from these devices are shown in . A minimum of 5 devices were averaged for each film. Up to 2 outlier devices were removed from each film, which were typically devices at the very edge with contacts shunted to the substrate. The front contact for all of these devices was ohmic without annealing, suggesting the carrier concentration was high. TLM data was inconclusive due to film inhomogeneities. A few devices were chosen from each film for quantum efficiency measurements. Fig. 22 shows typical internal quantum efficiency curves (Φ_{int}) for films 6 and 12, which are calculated from the external quantum efficiency by using the known reflectance of planar GaAs [59] and accounting for grid shading. The thickness of film 6 is around 300 nm, which is much larger than optimal since a large fraction of the light is absorbed before reaching the junction. In contrast, film 12 has an emitter only ∼100 nm thick and shows an improvement in Φ_{int} for all devices measured, particularly for short wavelengths. Passivation with Na_2S on film 6 yielded only marginal improvement in response below 450 nm. This suggests that the hole diffusion length in the emitter, and not surface recombination, is the present limitation to photocurrent in that wavelength region.

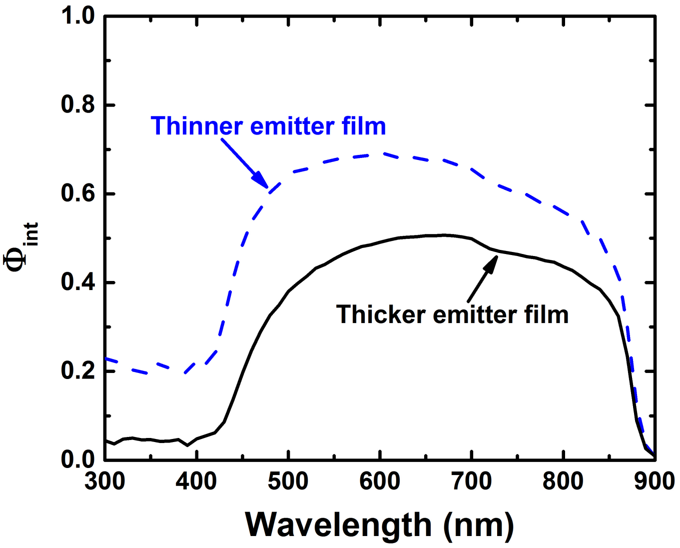

FIGURE 22. Internal quantum efficiency for two devices. Shown are a device on film 6 (black solid curve), and film 12 (blue dashed curve) showing improved response for the thinner emitter film.

The Ge-doped emitters had lower efficiencies than those doped by Te. However, the peak Φ_{int} is actually much higher for the Ge emitter grown on a CSVT absorber, which is expected given that the CSVT absorber material typically has a much longer electron diffusion length than the wafer substrates [28]. Since this emitter thickness was also >300 nm, one of its devices was etched in a solution of H2O, NH4OH, and

H2O2 in a ratio of 90:10:0.25 to observe Φ_{int} as a function of emitter thickness Fig. 23. The etch rate was measured by optical profilometry on bare GaAs wafers and was approximately 5 /s.

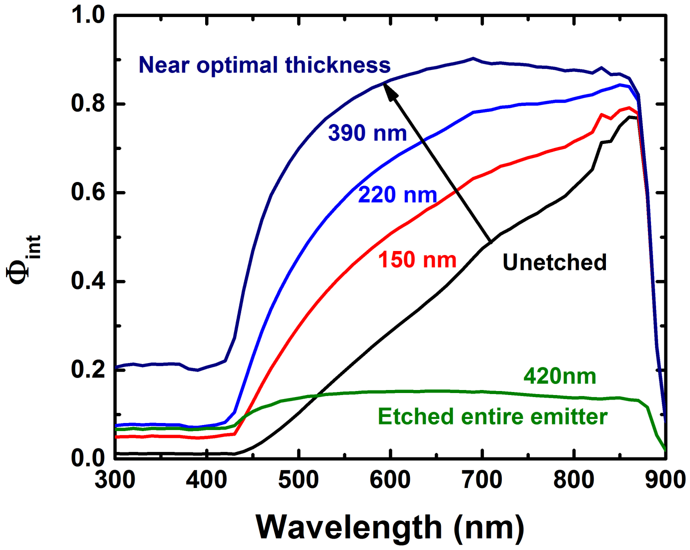

FIGURE 23. Internal quantum efficiency for etched device. QE curves are shwon at various etch depths for a device on film 9, Ge-doped $1 \times 10^{19}\,\mathrm{cm}^{-3}$ on Zn-doped $1 \times 10^{17}\,\mathrm{cm}^{-3}$ CSVT film. The labels indicate the depth etched on the emitter and show that response improves with thinning of the emitter.

A portion of film 9 was sent to Qspec Technology, Inc. for measurement of Zn and Ge concentrations using magnetic sector secondary ion mass spectrometry (SIMS). The SIMS profile (Fig. 24) shows that both Zn and Ge drop below the detection limit over a depth of 100 nm. Capacitance-voltage profile for a device on this film gives a carrier concentration of $4 \times 10^{16}\,\mathrm{cm}^{-3}$. Comparison with the SIMS Zn concentration suggests that the p-type film is compensated by n-type dopants to $6 \times 10^{16}\,\mathrm{cm}^{-3}$. This is consistent with the known sulfur background for this reactor measured by time-of-flight SIMS on a number of previously grown GaAs films.

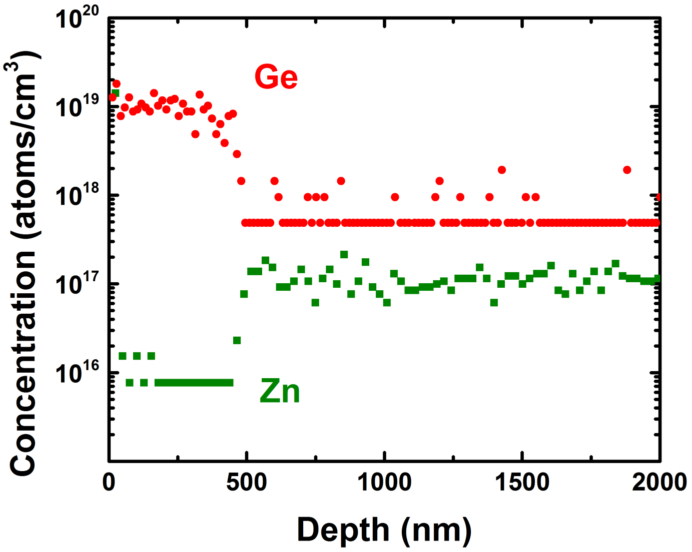

FIGURE 24. Magnetic sector SIMS of *pn* junction (collected by Qspec Technology, Inc.). The device had emitter doped by Ge optimized for detection of Zn, showing concentration matching target of $1 \times 10^{17}\,\mathrm{cm}^{-3}$.

It was found that devices with $V_{oc} > 900\,\mathrm{mV}$ had emitters doped heavily with Te. The surface of these layers in characterized by elongated hillocks, which is probably due to a surfactant effect that has been reported for Te [60]. These hillocks probably have the same origins are the surface defects discussed in the next chapter, but they tend to have smoother tops and are probably less likely to cause shunting. Nevertheless, we have detected at least one isolated shunt by using a lock-in thermography technique which can images localized heating. An optical microscope image of the surface morphology and the thermography result is shown in Fig. 25. Though the shunt cannot be conclusively tied to a surface defect it is clearly the cause of the V_{oc} deficit in that mesa cell compared to the surrounding cells which have high V_{oc}.

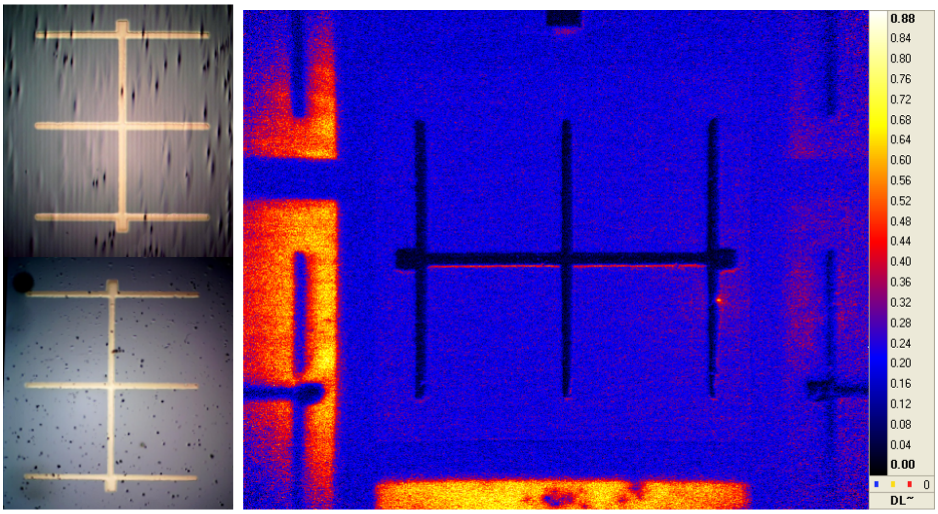

FIGURE 25. Surface morphology and shunting. Left: Comparison of surface defects in heavily Te (top) and Ge (bottom) doped films. Right: Shunt detected by lock-in thermography that is probably attributable to a surface defect.

Refined Device Properties

The devices fabricated are homojunction n^+p-type solar cells without passivation or antireflective coatings. Such devices are simple to fabricate and as a benchmark can be readily compared with results from other deposition techniques. The IV curve and IQE of the highest-efficiency (unpassivated) GaAs homojunction cell we have produced by CSVT is shown in Fig. 26 (measured prior to contact annealing, as discussed below). Integration of the EQE curve predicts $J_{sc} = 14.6\,\mathrm{mA\,cm^{-2}}$ for the AM 1.5G spectrum, which is in good agreement with the IV measurement of $13.9\,\mathrm{mA\,cm^{-2}}$, given the effect of grid shading. This J_{sc} compares favorably with HVPE homojunction devices fabricated at NREL which reach $14.2\,\mathrm{mA\,cm^{-2}}$ for similar structures [6, 61]. However, since the devices in the study are unpassivated (and therefore have poor short-wavelength response) and lack antireflective coating, the primary figure of merit is the open-circuit voltage (V_{oc}) which reflects the overall quality of the junction and should not depend strongly on J_{sc}. This also minimizes the impact of emitter thickness (which typically varies between 50–200 nm) in interpreting our results. Thickness uniformity could be improved by substituting machined graphite for the quartz spacers which are not precisely cut; it may also be influenced by temperature variations across the heaters as the uniformity of the heaters has not been evaluated. The maximum V_{oc} produced for CSVT devices is 916 mV, compared to 936 mV reported for an unpassivated HVPE cell [6] and 960 mV reported for an unpassivated HVPE cell with antireflective coating [7]. Further improvement is needed to compete with standards set by MBE and MOVPE, for which cells can attain $V_{oc} > 1\,\mathrm{V}$.

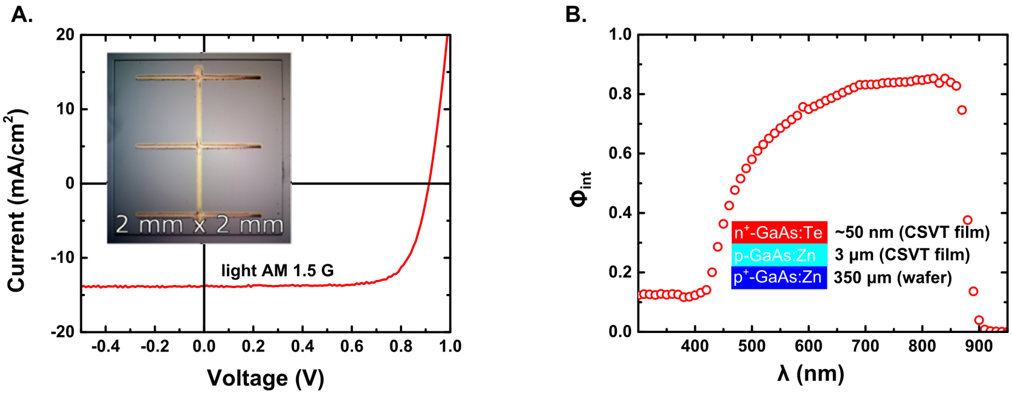

FIGURE 26. Record IV and QE curves. (A) JV curve for record efficiency device with unannealed contacts under one-sun simulated illumination. (B) Internal quantum efficiency for the same device.

The ToF-SIMS and magnetic sector SIMS depth profiles of two *pn* junctions are shown in Fig. 27. The emitter/absorber interface can be distinguished by the decrease in Te and S as well as an interfacial O spike which arises from the exposure to atmosphere between growths. Te concentration decreases by a factor of 10 over 20 nm, similar to the junction abruptness reported for recent Si-doped HVPE *pn*-GaAs structures with a growth interruption step between layers [61]. The elevated S concentration in the emitter is due to the use of a different graphite heater assembly and quartz tube; cleaning or replacing these parts decreases the unintentional n-type background to $1 \times 10^{16}\,\mathrm{cm}^{-3}$ based on Hall effect measurements of undoped films. The detection of O by SIMS is not surprising given H_2O is used as a transport agent, though its concentration could not be determined since a relative sensitivity factor was not available for the conditions used to collect this depth profile. Oxygen is known to be related to a defect level near the middle of the GaAs bandgap. However, while O has been detected in CSVT films at a concentration $1 \times 10^{16}\,\mathrm{cm}^{-3}$ by SIMS [19], the midgap state has only been reported by deep-level transient spectroscopy (DLTS) when O_2 was intentionally introduced into the reactor [62]. This is discussed further in Chapter VI. Increasing water vapor concentrations during growth have also been correlated with degraded photoluminescence [7, 63], although in our own work with electrochemical cells J_{sc} was only degraded at very high water concentrations (>4000 ppm) [11].

In our experience, specular films are produced by CSVT rarely and unpredictably when using commercial GaAs wafers as source material. Smooth film morphology in CSVT has previously been attributed to a reaction of water vapor with the substrate surface just prior to growth [64], suggesting that small variations in the growth atmosphere during temperature ramping can have a large impact on surface roughness. Since we have found that pressed powder sources almost always produce specular films, all of the solid-state devices here have been grown from powder sources rather than a wafer. However, these typically have a higher density of surface defects, often with an oval or circular aspect. Oval defects have not been observed in the specular films we grow from wafer sources. The source of these defects could therefore be GaAs particulates or a contaminant in the powder.

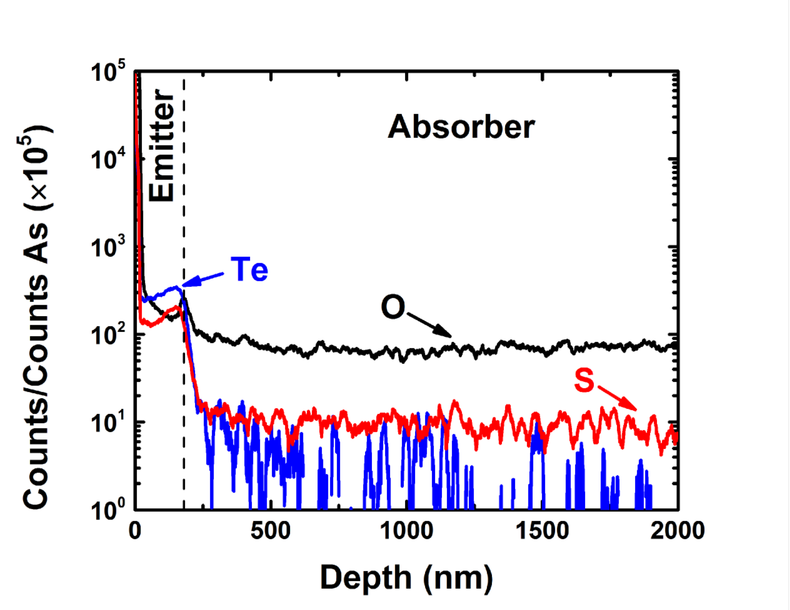

FIGURE 27. ToF-SIMS profile of *pn*-junction with emitter doped by Te. Concentrations are in arbitrary units (counts normalized to As)

Due to the difficulty in growing multiple layers in our simple research reactor, devices in this study do not use a highly-doped (typically $>1 \times 10^{19}\,\mathrm{cm}^{-3}$) contact layer which is common in III-V devices, though we have shown that these carrier concentrations are achievable using Zn and Te [28]. The lowest possible contact resistance to the $N_D \approx 1 \times 10^{18}\,\mathrm{cm}^{-3}$ emitter layers could only be obtained with an annealing step to form a tunneling contact. The device shown in Fig. 26 was subsequently annealed but this degraded the V_{oc}. On other devices annealed under the same conditions pits were observed at the edges of contact grids after annealing (shown in Fig. 28), consistent with contact spiking, which is known to occur at these temperatures due to formation of AuGa alloys [65, 66]. Since the contact resistance or presence of a contact barrier do not significantly affect V_{oc}, we focus on the characterization of unannealed devices in this study. In a more advanced

CSVT reactor design with multiple sources, passivation and contact layers could be developed more readily to optimize these aspects of device performance.

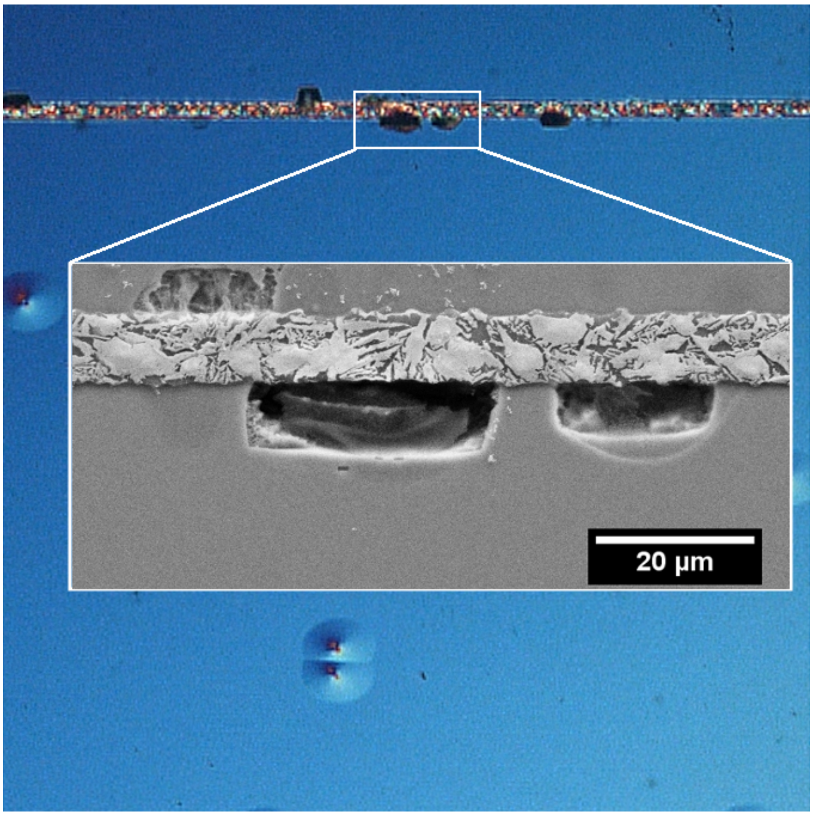

FIGURE 28. Contact spiking. Shown is DIC image of an annealed Ni/AuGe contact line and SEM image (inset) showing pits due to contact spiking. Also visible in the DIC image is the pair of oval defects which were later examined using SIMS.

Fig. 29 shows the variation of V_{oc} with surface defect density for 9 different samples and 90 individual mesa-etched devices with absorber films grown from three separately-prepared source pellets, all grown with the same substrate temperatures but with varied water vapor concentration. It is clear that surface defects have a major impact on V_{oc}. There is also a strong relationship between the source pellet preparation and the surface defect density N_{SD}. Film morphology and V_{oc} was best for the later growths when unannealed source powders were used. For the two films with highest V_{oc}, the source had been prepared by addition of Zn metal to undoped GaAs and was annealed in pellet form at 1200 °C in an evacuated quartz ampoule. These results are evidence that a majority of the defects observed are due to particulate transfer from the source. Small particulates are likely consumed by vapor transport, sintering during annealing, or the repeated thermal cycling during multiple film depositions, thereby improving the film quality. Reduction in surface defects with source pellet reuse was also observed in investigations of $GaAs_{1-x}P_x$ growth by CSVT [67].

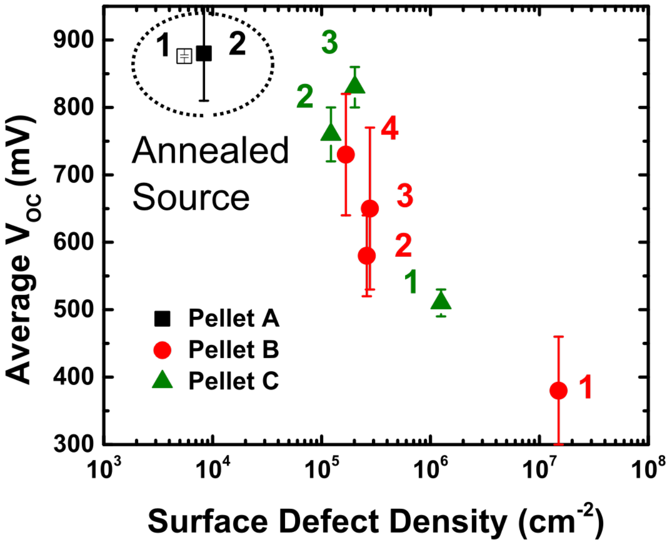

FIGURE 29. Effect of surface defects on V_{oc}. Different colors/symbol shapes represent different absorber source pellets, while the numbers indicate the order in which the samples were grown from that source. Averages are for the 10 mesa-isolated devices for each pn junction and error bars represent a single standard deviation. The single open square was collected on a device with annealed contacts.

It is interesting to note that the best performing devices were grown from a pellet annealed in an evacuated ampoule with no As overpressure. The resulting source material is therefore somewhat Ga-rich, yet still produces films with high minority carrier diffusion lengths as evidenced by IQE and J_{sc} measurements. This is interesting since the concentration of intrinsic defects such as the EL2 defect (which is related to an AsGa antisite point defect) would be expected to vary with source stoichiometry. The effect of substrate temperature on EL2 in CSVT GaAs has previously been studied using DLTS [68], but no studies have investigated the effect of changes in source composition which might occur over time due to incongruent loss of As and Ga from the source material. Such an effect could be minimized in a carefully engineered reactor where gas leakage from within the reaction zone would be small. In the current reactor the quartz ring separating source and substrate must have small gaps to allow infiltration of the transport agent since there is no mechanical mechanism to separate the source and substrate in situ.

CV measurements were performed to determine the hole concentration in the absorbers (Fig. 30). The water vapor concentration was not identical for all growths but did not appear to have an effect on dopant density. Pellet A is the annealed source referenced above, which was doped by addition of Zn powder to undoped GaAs powder, while the other two pellets were prepared by grinding wafers which were doped by the wafer manufacturer. For each source, the first deposition was a control film on an undoped substrate which was characterized by Hall effect. Both Hall effect and capacitance measurements show a trend of decreasing hole concentration as a pellet is reused for multiple growths, to the point that the last two films from pellet B had an n-type Hall effect response. One possible explanation for the decreased doping efficiency is that water vapor reacts with Zn to form oxides which are less volatile [69] and that over several growth cycles oxygen diffuses throughout the source material. The lack of volatility of ZnO makes Zn doping by this method less feasible, especially in a manufacturing context. In contrast to Zn, Te has been reported to transport with unity efficiency [25], likely due to the higher volatility of its oxides, and we have not observed a decrease in the Te doping with source reuse. Consistent Zn doping is probably achievable using HCl as a transport agent because zinc chloride species have high vapor pressures at the growth temperatures, and thus would be expected to have high utilization.

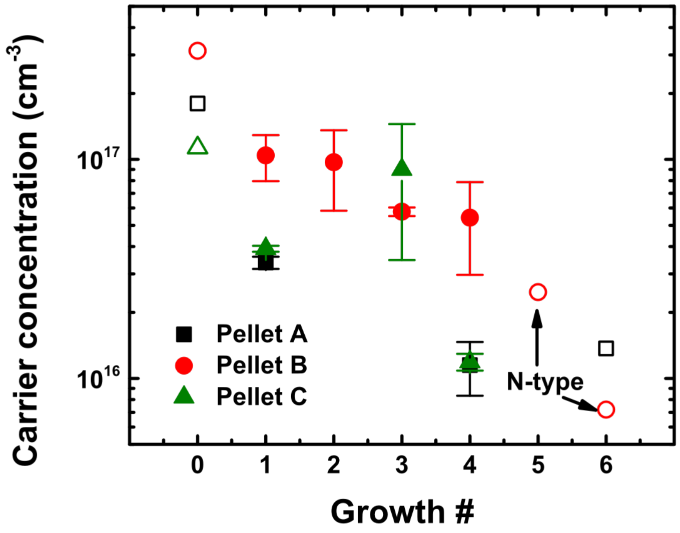

FIGURE 30. Carrier concentration over sequential growths from a given source pellet. Open symbols represent Hall effect measurements performed on control samples deposited on undoped substrates. For some growths carrier concentrations could not be determined and are omitted from the figure.

Origin of Surface Defects

Oval defects have been extensively studied in films grown by MBE, and are often associated with the Ga source due to spitting or oxide formation, but can also arise from substrate contamination or particulate transfer [70–75]. Oval defects have been previously reported in CSVT GaAs grown from single-crystal wafer sources and were attributed to surface contamination of the substrate prior to growth [64]. We have observed that residue left after surface preparation can lead to the formation of elongated polyhedral pits originating at the substrate interface these are easily distinguishable from the defects studied here which are surrounded by hillocks and can form far from the substrate/film interface. In the CSVT reactor used here, particulates are a likely source of these defects due to the use of powder sources in close proximity to the substrate. Oxide-related defects are also possible due to the use of H_2O as a transport agent.

In order to better understand the origin of the performance-limiting surface defects, we chose two samples with relatively high N_{SD} for detailed study. Sample A was a device with both absorber and emitter grown by CSVT, and with $N_{SD} = 3 \times 10^5\,\text{cm}^{-2}$. Sample B was an n-type emitter film grown by CSVT on a commercial p-type wafer which was Zn-doped to $5 \times 10^{17}\,\text{cm}^{-3}$ and with $N_{SD} = 8 \times 10^4\,\text{cm}^{-2}$. For Sample A, the H_2O concentration was measured to be 2400 ppm and 1900 ppm for the absorber and emitter films, respectively, while Sample B was grown with a concentration of 4000 ppm. Processing of these cells was identical except that the contacts for Sample B were annealed and therefore some of the devices from Sample B have better fill factors due to a lower series resistance. The IV characteristics for the mesa-etched cells fabricated on these films are shown in Fig. 31. The large scatter in V_{oc} is attributed to shunting through differing numbers of surface defects. The best devices for the wafer absorber sample in Fig. 31B have higher V_{oc} than the best CSVT absorber devices in Fig. 31A due to the lower number of surface defects in that sample, and therefore a lower likelihood of shunting. Devices with CSVT absorbers have a higher current since the minority carrier diffusion lengths are higher in CSVT material than in the wafer substrates (which are produced by the vertical gradient freeze technique) [12, 28].

Optical images of two defect sites analyzed by ToF-SIMS are shown in Fig. 33. The defects which are mostly present on the Sample A have large pits with irregularly-

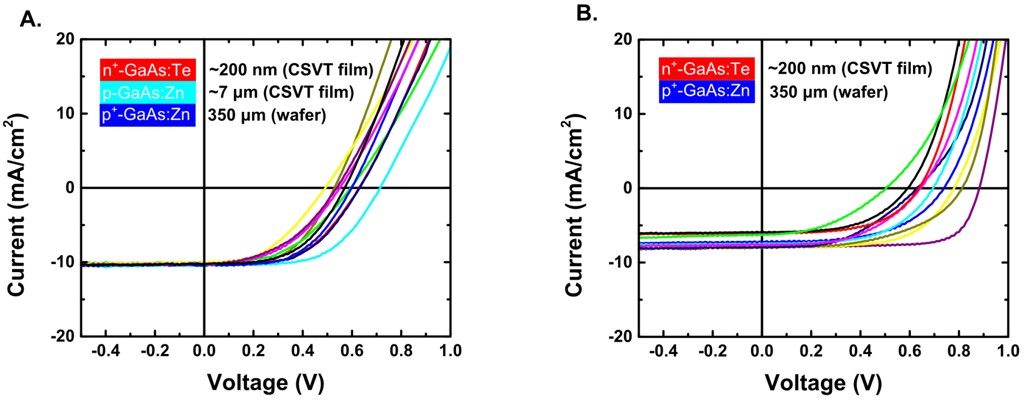

FIGURE 31. IV curves for cells chosen for surface defect characterization. (A) emitter and absorber films grown on a wafer substrate, (B) emitter film grown by CSVT using wafer substrate as the absorber layer.

shaped spikes near the center of the hillocks, including some which are present underneath the front contact (Fig. 32) and can contribute to device shunting. The difference in morphology between Sample A and B is at least partially attributable to the thickness of the CSVT absorber film (7 µm) which has probably grown around sites of contamination. We refer to defects such as those in Fig. 33A as particulate-related defects based on morphology and the SIMS, SEM, and TEM analyses of similar defects. For Sample B, most of the defects are morphologically similar those in Figure 6B; that is, consistently-shaped hillocks with relatively small central cores just visible by optical microscopy. We refer to these as oxide-related defects based on EDS analysis below.

A comparison of the SIMS spectra for a number of defect sites and defect-free regions revealed that Si is present only in the particulate-related defects (Fig. 34), while both defect types had elevated concentrations of oxygen and hydrocarbon species compared to defect-free regions. The mass spectrum in Figure 7 is constructed from a 75 × 75 µm total area with 300 nm sputter depth but excludes data from the first 25 nm to avoid detection of adventitious surface species. In our experiments,

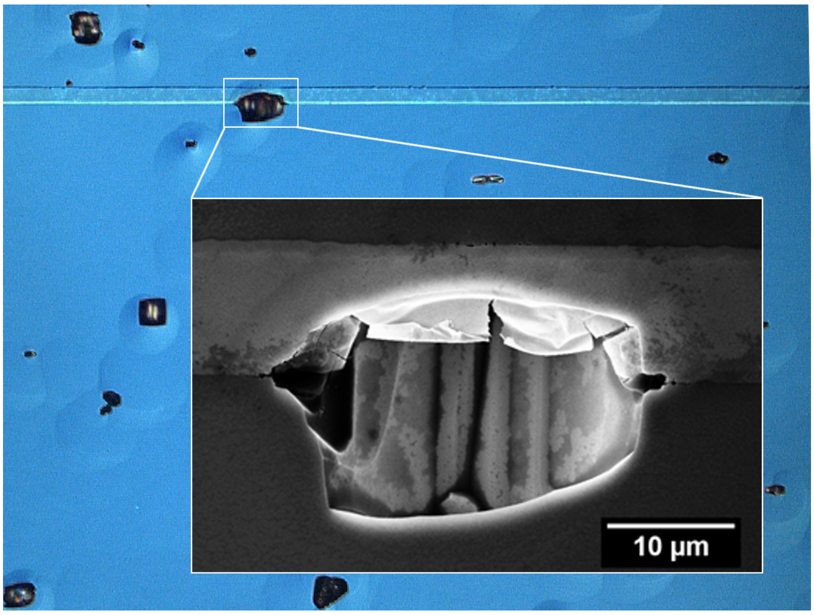

FIGURE 32. DIC and SEM image (inset) of a pitted defect underneath the contact grid of a solar cell with CSVT-grown absorber and emitter.

we have never detected Si in defect-free regions of CSVT-grown GaAs films even when both Si and fused quartz are present in the hot zone of the reactor, or when intentionally Si-doped source material was utilized [28]. Si is only likely to transport as SiO at very low rates in very dry H2 [76]. Si has a vapor pressure several orders of magnitude lower than ZnO at 900 °C [77], so the transport efficiency of Si should be substantially lower than Zn (which is $< 1\%$). The Si detected in defective regions is thus very likely transported in the solid phase as a particulate. The origin of Si in the source material might be contamination during grinding in the agate mortar and pestle.

Composition and morphology of the two types of defects were compared under SEM by creating cross-sections using FIB milling. In addition, the particulate-caused defect was thinned and lifted out for TEM analysis. A comparison of the SEM images and EDS maps is shown in Fig. 35. For the defects believed to be caused by particulates (i.e. those defects that reduce in density with source pellet annealing),

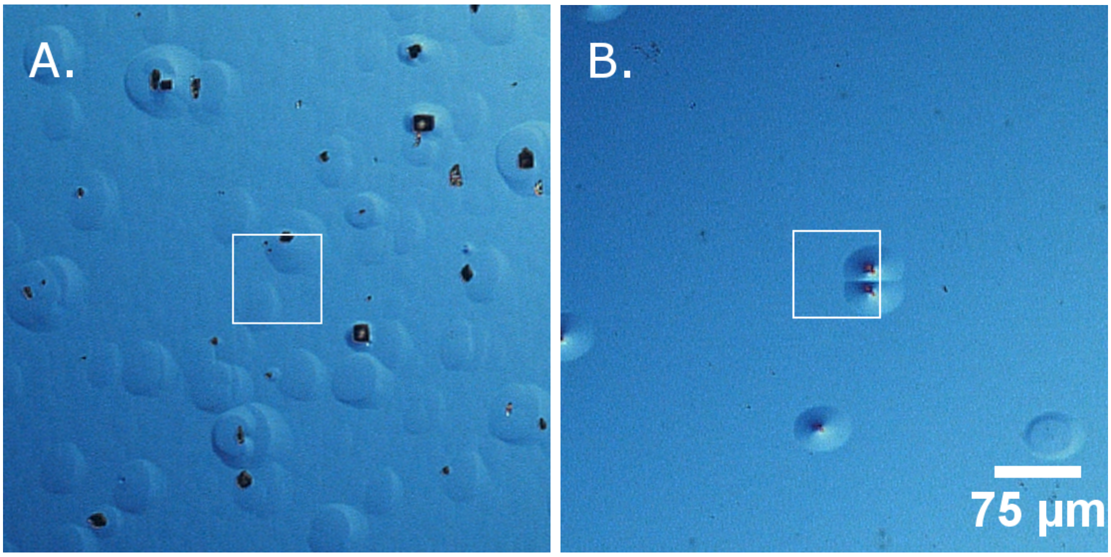

FIGURE 33. Differential interference contrast images of the film surfaces. Images were taken prior to SIMS measurement. A) Defects with irregular cores found on Sample A. B) Defects found on Sample B with more regular morphology. The white boxes indicate the approximate SIMS analysis regions.

the defective region has very little contrast compared to the epitaxial film in the SEM image and the composition is identical to the film within detection limits of the EDS. In contrast the oxide-related defects (as in the optical image in Fig. 33B) on Sample B have increased oxygen concentration and arsenic deficiency, indicating that the central portion is likely a GaO_x phase. The higher water concentration during deposition for Sample B (4000 ppm) as compared to Sample A (2000 ppm) may account for the higher proportion of oxide-related defects. The small number of particulate-related defects in Sample B is probably due to the limited deposition time as well as the variability of the source pellet properties.

Fig. 36 shows the bright-field TEM image of the same particulate-caused defect as shown in Fig. 35A. There is a clear grain boundary between the defect and the epitaxial film, and at least three grains are apparent within the defect. This might indicate that the particulate consisted of several sintered crystallites which grew into

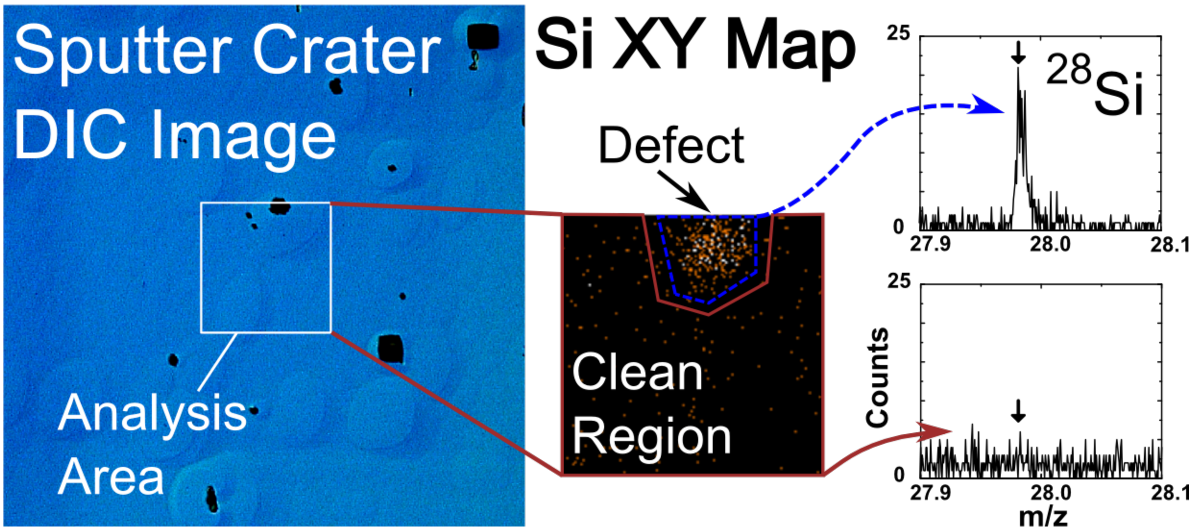

FIGURE 34. DIC image, Si XY map, and Si mass spectrum peak for a region on the CSVT sample collected from the bulk of the emitter. The mass spectra indicate that Si counts within the clean region are attributable to background noise.

a polycrystalline mass during film deposition. EDS linescans performed on the TEM across the grain boundary again showed no compositional difference between the epitaxial film and the defect.

Strategies for Defect Mitigation

Elimination of particulate-caused surface defects will require either an alternative source preparation technique or a method to block particulates from transferring in the growth chamber. The latter strategy may be possible by integrating a thin ceramic membrane between source and substrate, but may decrease growth rate which is driven by diffusion in CSVT. Particulate-free source material might be prepared cheaply through a hot-pressing technique. The fact that specular films can be grown more easily from powder sources than from wafer sources merits further investigation but is likely related to the increased surface area of the powder since the powder is produced by grinding sections of the same wafers. For instance, the transport rate of

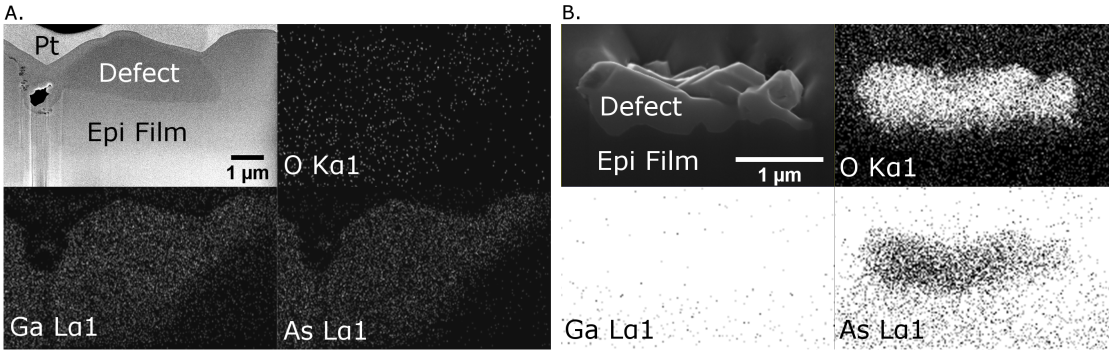

FIGURE 35. SEM images and EDS mapping of the central core defects. A) a particulate-related defect and B) an oxide-related defect and EDS intensity maps of O, Ga, and As for cross sections prepared by FIB. The SEM image and the EDS elemental maps are of identical regions and the scale is the same.

Ga at the start of growth from a pellet might be higher due to the increased surface available for oxidation.

Oxide-related defects appeared in high density only in the emitter film grown directly on a wafer, and so their formation may be related to the higher water concentration used for that growth. This suggests that, while increasing water vapor concentration increases growth rate, the water concentration must be kept below some threshold value to prevent formation of these defects (at least at substrate temperatures used for the emitter depositions). Thus, the high growth rates desired for a high-throughput CSVT process are best achieved by minimizing source/substrate spacing or by increasing the temperature gradient between source and substrate. Alternatively, replacing H_2O with HCl should eliminate oxide-related defects, at the cost of more stringent requirements on reactor components to avoid corrosion and film contamination. The use of HCl for transport is still an attractive option since the chlorides of metals of interest for III-V growth have much higher vapor pressures than their corresponding oxides. Zn doping efficiency, for example, should

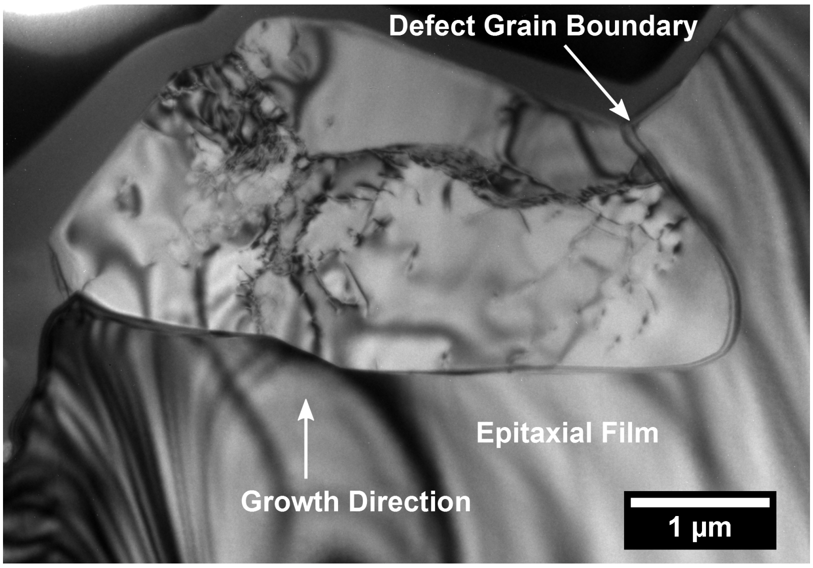

FIGURE 36. Bright-field TEM image of a particulate-caused defect.

be improved in an HCl system, and growth might be achieved at lower substrate temperatures typical of MOVPE or HVPE.

Bridge

Given the appearance of oxide phases in some of the films, it is important to consider the concentration of microscopic defects due to oxygen. These defects and other extrinsic or intrinsic defects can serve as recombination centers if they create energy levels which lie far from either band edge, and therefore can limit the performance of cells, assuming the large morphological defects are eliminated. The next chapter describes a study using DLTS which particularly focuses on the defect concentrations as H_2O concentration and growth temperature are changed.

CHAPTER V

ELECTRICAL DEFECT CHARACTERIZATION

Introduction

Defects in semiconductors can be either native (or intrinsic) or extrinsic depending on whether they originate from the material itself or a foreign impurity. In compound semiconductors like GaAs, native defects include vacancies (missing atoms), interstitials (atoms existing between crystal lattice sites), and antisite defects (Ga on an As site, or vice versa). Some of these defects can give rise to localized electronic states within the band gap, and those which lie near the middle of the gap can serve as effective recombination centers. Since GaAs has been heavily studied for many decades, the origin of many such states has been conclusively tied to chemical impurities or native defects. However, in some cases the chemical or structural origin of widely identified states is still debated. In any case, these states depend strongly on the method of growth since temperatures can range from a ~300 °C to the melting point, and different precursors and growth chamber materials determine the common impurities. Some of these extrinsic defects can be chemically identified, using for instance SIMS. For CSVT, we have established that S is the most common unintentional n-type dopant, and O has been conclusively identified only near the substrate interface. Other impurities exist in concentrations too low to measure by ToF-SIMS, or are associated with surface contamination (e.g., K, Na) and are not present in the bulk of the films.

Transient capacitance or current measurements provide a method to probe very low concentrations of defects, though without direct chemical identification. Linking defect states detected using these measurements to their physical origin can be accomplished by intentional addition of an impurity, by modelling the expected incorporation on the basis of kinetic or thermodynamic growth processes, or by modelling the electronic structure of suspected defects (e.g., using density functional theory). It is not well understood how changing growth conditions in CSVT affects the concentrations of mid-gap defects which may limit solar cell performance, particularly when targeting high growth rates and low substrate temperatures which are desirable for photovoltaic processing.

Of particular interest is the family of electron traps referred to as EL2, which are attributed to the isolated arsenic antisite ($\mathrm{As_{Ga}}$) defect [78, 79] or a complex involving $\mathrm{As_{Ga}}$ [80–82]. Defects given the label EL2 are always electron traps with energy around $E_c - 0.8\,\mathrm{eV}$. Early work also considered oxygen as the origin of EL2 [83], but it is more generally accepted that a distinct level, labelled ELO, is associated with oxygen and was in some cases misidentified as EL2 [84]. Given the position deep in the band gap, these trap levels are expected to negatively impact minority carrier lifetimes and degrade the efficiency of photovoltaic devices. Accordingly, recent work has found that an EL2 center is the primary minority-carrier trapping defect in p-type MOVPE-grown GaAs when growth rates are increased to $1\,\mu\mathrm{m\,min^{-1}}$ at typical growth temperatures [85]. The trend of increasing EL2 concentration ([EL2]) with growth rate has been reported in both HVPE [86] and CSVT films [87, 88] as well. This increase in [EL2] with growth rate is not surprising for MOVPE and HVPE which typically operate in a kinetically-limited growth regime with significant arsine overpressures. At increased temperatures, however, [EL2] has been observed to decrease both for MOVPE growths with substrate temperatures slightly elevated from 640 °C to 680 °C [85] and for HVPE growths carried out at 800 °C. In the latter case,

[EL2] was found to be independent of growth rate, indicating a thermodynamically-limited growth process [86].

In H_2O-mediated CSVT, growth temperatures are most often in excess of 800 °C, and growth is often analyzed assuming the source and substrate are in near-equilibrium conditions. For this reason, [EL2] in CSVT is expected to have low values similar to HVPE-grown material, neglecting possible interactions with oxygen. Several DLTS studies of H_2O-mediated n-type CSVT films have been previously published [62, 68, 87–91], finding in all cases one or two peaks near 300 K with E_a ~0.8 eV. Unfortunately, studies which found a possible correlation with oxygen for the lower temperature peak also employed Al barriers for their Schottky devices [62, 68, 89, 90] which may have impacted the results due to oxygen diffusion from the metal layer. Furthermore, none of these studies consider the variation of trap concentration with changing water vapor concentration ($[H_2O]$), though this should increase the amount of oxygen incorporated in the films. Omission of $[H_2O]$ in some publications also makes reports of changing [EL2] in CSVT films grown at different temperatures difficult to assess. In this study, we report of the detection of two separate trap levels in CSVT GaAs films which we assign to ELO and EL2.

We find that the oxygen-related center, ELO, is in fact the dominant electron trap in H_2O-mediated CSVT GaAs for most growth conditions and consider the effects of changing growth conditions on both EL2 and ELO. Furthermore, the ELO center is the most strongly dependent on $[H_2O]$, providing evidence that this is the primary oxygen-associated trap in GaAs. We use a simple equilibrium model to predict the dependence of [ELO] on [H2O] and determine that [ELO] trends are best explained if it is not an isolated substitutional oxygen center but instead a defect complex with two As_{Ga} as has been predicted in theoretical studies. Because of this complexing,

[EL2] is typically lower in CSVT films compared to MOVPE or HVPE films. We propose strategies for achieving high growth rate in CSVT while minimizing defect concentrations.

section 5.1 provides a summary of the films grown for this study. The water vapor concentration during growth, [H_2O], is taken as the average value measured by the hygrometer during the last ten minutes of growth, though the variation is only 5 % after the first few minutes of wet H_2 flow. Other values given are δ, the spacing between source and substrate, and T_{src} and T_{sub}, the source and substrate temperatures, respectively. Film thicknesses were measured optical profilometry, and reported thicknesses are an average of four measurements at widely-spaced locations around the edge of the films. Uncertainties are the standard deviation of the thickness measurements. Growth rates are calculated from the thickness measurement and growth time.

Oxygen in CSVT GaAs

Oxygen incorporation in GaAs has been studied extensively in crystals grown by a wide variety of techniques. Defect structures and energy levels associated with oxygen have also been the subject of a number of theoretical studies [92–95] which have concluded that the most likely stable defects are an interstitial (O_i) and a Ga-O-Ga structure, which may be a defect complex with O on an As site binding to two As antisites [$(As_{Ga})_2$ - O_{As}] [96, 97]. While the interstitial is agreed to be electrically inactive (and therefore not detected in DLTS measurements), the substitutional form has been implicated in a number of deep states detected by DLTS [84, 90, 98–105]. Additionally, studies of localized vibrational modes using infrared absorption have suggested that the two donor levels associated with O_{As} are situated at 0.14 eV and

TABLE 3. Growth parameters for the films studied. All films were grown from the same undoped polycrystalline GaAs source material, either directly from a cleaved piece or from a pellet made by grinding and hydraulic pressing.

Sample ID	**[H_2O] (ppm)**	**δ (mm)**	**growth rate (nm min^{-1})**	**T_{src} (°C)**	**T_{sub} (°C)**	**thickness (µm)**
	Pellet 1					
S1-160725	10700	1.9	210 ± 20	850	830	8 ± 1
S1-160726	2200	1.9	100 ± 10	850	830	3.9 ± 0.4
S2-160726	1150	1.9	40 ± 10	850	830	1.5 ± 0.4
S2-160727	10200	1.9	220 ± 20	850	830	4.4 ± 0.5
S1-160728	2100	1.9	70 ± 9	850	830	2.8 ± 0.4
S2-160729	1100	1.9	40 ± 4	850	830	2.3 ± 0.2
	Pellet 2					
S1-160831	2070	1.6	79 ± 5	850	830	3.2 ± 0.2
S1-160901	1940	1.6	180 ± 13	850	780	5.4 ± 0.4
S2-160901	4030	1.6	290 ± 27	850	780	7.2 ± 0.7
S2-160902	7750	1.6	407 ± 70	850	780	8.1 ± 1.4
S3-160902	1970	0.8	301 ± 32	850	780	9.0 ± 1.0
S1-160903	7470	0.8	700 ± 40	850	780	14.0 ± 0.8
	Wafer					
S3-161011	8000	1	720 ± 160	850	780	14 ± 3
S1-161012	4200	1	410 ± 130	850	780	12 ± 4
S2-161013	1900	1	430 ± 80	850	780	8 ± 2

0.57 eV below the conduction band [99, 102] with the latter possibly detected by DLTS (in Bridgman-grown GaAs) and labelled EL3 [101]. On the other hand, Lagowski et al. were the first to identify the 0.8 eV DLTS peak as ELO by adding oxygen during Bridgman-growth of GaAs [84] and there is significant experimental evidence for this being the dominant oxygen-related trap in GaAs.

To determine whether ELO is affected by the water vapor concentration, the films listed in Table 1 were grown with varying [H_2O]. For pellet 1, a series of three [H_2O] values was also repeated to examine whether reuse of the source material would affect any trap concentrations (e.g., due to contamination or changing stoichiometry) and to confirm repeatability of the DLTS measurement. For growths with low [H_2O], two peaks are clearly resolved slightly above room temperature. At higher [H_2O], the lower temperature peak increases significantly and obscures the other peak. DLTS spectra for three of these films is shown in Fig. 37. By simultaneously fitting the two peaks to the theoretical curves , we find the activation energies and capture cross sections to have mean values (based on the six films grown from pellet 1) of $Ea_1 = 0.789 \pm 0.006\,\text{eV}$, $\sigma_1 = 1.6 \pm 0.4 \times 10^{-12}\,\text{cm}^2$, $Ea_2 = 0.82 \pm 0.02\,\text{eV}$, and $\sigma_2 = 1.1 \pm 0.8 \times 10^{-13}\,\text{cm}^2$ which are consistent with the literature values for ELO and EL2, respectively [79].

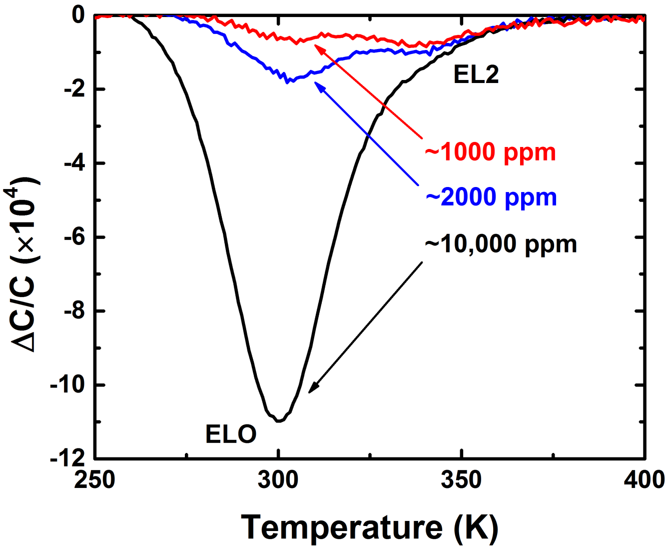

FIGURE 37. DLTS spectra for films grown with different [H_2O]. All films were grown at $T_{src} = 850\,^\circ\text{C}$ and $T_{sub} = 830\,^\circ\text{C}$, and the rate window is 0.372 s. The 300 K peak increased in magnitude with [H_2O] for all growths.

Given experimental and theoretical reports of the EL3 defect associated with oxygen, we have evaluated the DLTS spectra of a few films over an extended temperature range down to 100 K. There is in fact a small peak detectable in some of the spectra which is consistent with the EL3 trap, but its concentration does not increase significantly with [H_2O], as shown in Fig. 38. For the film with [H_2O] = 1190 ppm we estimate its density to be $N_T \approx 4 \times 10^{12}\,\text{cm}^{-3}$. The fact that this peak overlaps with the minority carrier signal strongly observed samples grown at higher

[H_2O] from pellet sources (discussed below) makes determination of its concentration uncertain, but we estimate [EL3] ¡ $4 \times 10^{13}\,\mathrm{cm}^{-3}$ (Fig. 38B). In films grown from a wafer source, we found this trap in a larger range from 10×10^{13}–$1 \times 10^{14}\,\mathrm{cm}^{-3}$, but its concentration decreased monotonically as the source wafer was reused, indicating it could be associated with an impurity other than O. In all cases [ELO] is much larger than [EL3] and so we focus our analysis on ELO as the dominant O-related center. A shallow trap was also detected at 110 K for some samples, with $E_{na} = 0.189 \pm 0.006\,\mathrm{eV}$, $\sigma_{na} = 7 \pm 4 \times 10^{-15}\,\mathrm{cm}^2$, but this also could not be correlated with [H_2O].

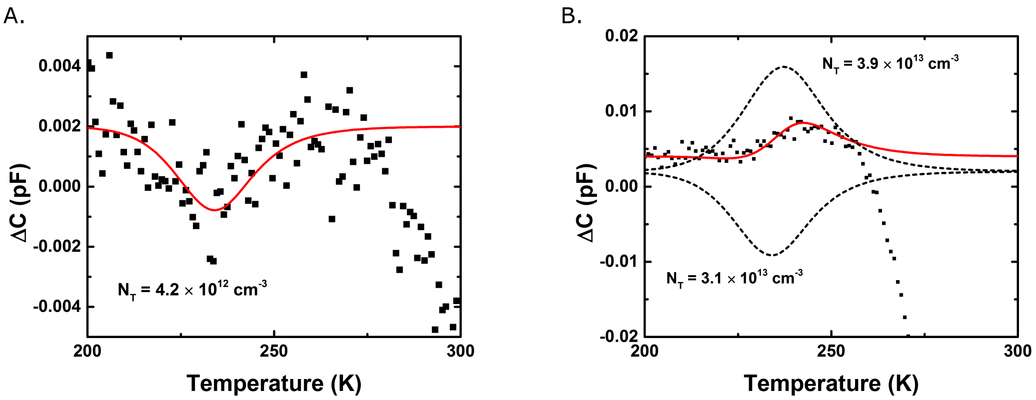

FIGURE 38. 230 K peak. A) Sample S2-160728 (1190 ppm growth) and theoretical curve for a defect with $E_{na} = 0.57\,\mathrm{eV}$ and $\sigma_{na} = 4 \times 10^{-13}\,\mathrm{cm}^2$ and constant offset assumed to be an instrumental artifact or small minority emission signal. Reported values for an oxygen-related trap are $E_{na} = 0.58\,\mathrm{eV}$ and $4 \times 10^{-13}\,\mathrm{cm}^2$ [101]. B) Same region in spectrum for S2-160727 (10,200 ppm growth) with plausible overlapping minority and majority carrier peaks. The majority carrier peak has the same trap parameters as in (A) while the minority carrier peak has parameters based on the Arrhenius fit in other films.

The effect of substrate temperature on ELO was also investigated. For this series, a second source pellet was prepared and the first film was grown at conditions used for two of the films from pellet 1. The results are shown in table 4 along with all of the other trap densities calculated for the films grown from pellets. The trap

TABLE 4. Film free electron and trap concentrations calculated from CV and DLTS measurements for films grown with $T_{src} = 850\,°\text{C}$ and $T_{sub} = 830\,°\text{C}$. The lambda correction has been applied to the trap densities. Standard errors in trap density are based on the results of the fitting routine.

Film	**[H_2O] (ppm)**	**growth rate ($\mu\text{m}\,\text{h}^{-1}$)**	**N_D (cm^{-3})**	**N_{ELO} (cm^{-3})**	**N_{EL2} (cm^{-3})**
S1-160725	10700	13 ± 1	5.5×10^{15}	$2.89 \pm 0.08 \times 10^{14}$	$1.7 \pm 0.8 \times 10^{13}$
S1-160726	2200	6 ± 0.6	9.0×10^{15}	$5.1 \pm 0.3 \times 10^{13}$	$1.5 \pm 0.3 \times 10^{13}$
S2-160726	1150	2.4 ± 0.6	6.5×10^{15}	$1.8 \pm 0.2 \times 10^{13}$	$2.3 \pm 0.2 \times 10^{13}$
S2-160727	10200	13 ± 1	13×10^{15}	$7.0 \pm 0.2 \times 10^{14}$	$7.6 \pm 0.2 \times 10^{13}$
S1-160728	2100	4.2 ± 0.5	5.8×10^{15}	$4.46 \pm 0.09 \times 10^{13}$	$2.3 \pm 0.1 \times 10^{13}$
S2-160728	1190	2.4 ± 0.2	4.1×10^{15}	$1.5 \pm 0.1 \times 10^{13}$	$2.4 \pm 0.1 \times 10^{13}$
S2-160831	2070	4.8 ± 0.3	14×10^{15}	$5.7 \pm 0.2 \times 10^{13}$	$1.4 \pm 0.2 \times 10^{13}$
S1-160901	1940	10.8 ± 0.8	14×10^{15}	$1.59 \pm 0.03 \times 10^{14}$	$2.4 \pm 0.3 \times 10^{13}$
S2-160901	4030	17 ± 2	12×10^{15}	$7.20 \pm 0.04 \times 10^{14}$	*
S2-160902	7750	24 ± 4	25×10^{15}	$2.6 \pm 0.5 \times 10^{15}$	*
S3-160902	1970	18 ± 2	9.8×10^{15}	$1.40 \pm 0.02 \times 10^{14}$	$8 \pm 2 \times 10^{12}$
S1-160903	7470	42 ± 2	16×10^{15}	$3.40 \pm 0.02 \times 10^{15}$	*
S3-161011	8000	43.2 ± 9.6	9.1×10^{15}	$1.08 \pm 0.01 \times 10^{15}$	$2.13 \pm 0.08 \times 10^{14}$
S1-161012	4200	24.6 ± 7.8	5.5×10^{15}	$5.74 \pm 0.06 \times 10^{14}$	$1.10 \pm 0.06 \times 10^{14}$
S2-161013	1900	25.8 ± 4.8	9.5×10^{15}	$2.27 \pm 0.02 \times 10^{14}$	$4.60 \pm 0.02 \times 10^{13}$

*Not calculated, see text

concentrations for film 1 grown from pellet 2 were essentially identical to the previous growths, although the background electron concentration was somewhat higher for all films grown from pellet 2. When the substrate temperature was lowered to 780 °C for the next five growths, ELO increased substantially but had a similar trend with varying [H_2O]. This is consistent with the fact that Ga_2O has a low volatility which decreases with temperature and so should be more likely to remain incorporated in the film at lower temperatures.

Arsenic Antisite Defects

High growth rates are expected to provide significant cost benefit [3] for manufacturing, providing an additional motivation for lowering the substrate temperature since the temperature gradient partly determines film growth rate. Additionally, two of these films were grown with a significantly smaller source/substrate spacing (∼0.8 mm, as shown in table 4) providing growth rates up to 700 nm min^{-1}. With the smallest spacing, the temperature gradient of 70 °C is very near the maximum achievable in our reactor (i.e., the point at which the substrate is heated entirely by the source heater). As discussed in Chapter II and shown in Fig. 6, growth rates for the films studied here are roughly proportional to $\sqrt{P_{H_2O}}$ and inversely proportional to δ as expected for diffusion-limited growth. The dependence of growth rate on temperature is more complicated as it depends on the equilibrium constants for the transport reactions as well as diffusivity of reactants, but generally is expected to increase with average temperature and temperature gradient.

For the films grown from the first pellet at relatively low growth rates, the DLTS spectra are fit well by the model with activation energies and capture cross sections near published values. Fits for two of the films with very different [ELO] are shown in Fig. 39. On the other hand, films grown at high growth rate have more complex DLTS spectra. In particular, the ELO peak is broader than expected given the model, although the activation energy obtained from an Arrhenius plot using the peak center is near the expected value. An example of a poor fit is shown in Fig. 40. EL2 values are only calculated for films where the model produced a good fit, while ELO values are reported for all the films; the spectra are fit as a single trap for the films with broadened peaks.

In addition to peak broadening, a minority carrier signal (corresponding to hole emission) is detectable for some samples around 250 K with an activation energy of approximately 0.55 eV. It is uncommon to observe minority carrier peaks without optical excitation or forward-bias injection pulses using a pn-junction, but previous studies have reported such a phenomenon [106, 107]. Modelling of the Au/n-GaAs

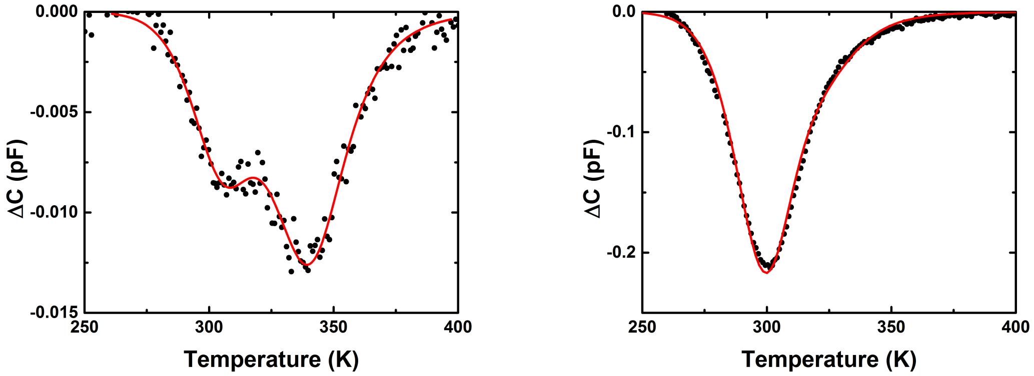

FIGURE 39. DLTS curve fitting. Left: fit to DLTS peaks for film S2-160728 with parameters $E_{ELO} = 0.79\,\text{eV}$, $\sigma_{ELO} = 1.5 \times 10^{-12}\,\text{cm}^2$, $E_{EL2} = 0.85\,\text{eV}$, $\sigma_{EL2} = 3.5 \times 10^{-13}\,\text{cm}^2$. Right: fit to DLTS peaks for film S1-160725 with parameters $E_{ELO} = 0.79\,\text{eV}$, $\sigma_{ELO} = 3.0 \times 10^{-12}\,\text{cm}^2$, $E_{EL2} = 0.83\,\text{eV}$, $\sigma_{EL2} = 7.4 \times 10^{-13}\,\text{cm}^2$.

junction using SCAPS software suggests that there is a thin region near the junction over which a trap may cross the hole quasi-Fermi level , making it likely that the signal is due to defects near the metal/semiconductor interface. The size of this peak appears to decrease with growth cycles as shown in Fig. 41. The fact that the peak becomes much smaller for later growths, even when the same water vapor concentration is used, indicates that it is dependent on the aging of the source material. A likely culprit is surface defects caused by particulates transported from the pressed powder source material, which we have previously reported for both GaAs and $\text{GaAs}_x\text{P}_{1-x}$ films grown from powder sources. After several growth cycles, the surface defect density is reduced due to sintering of the pellet. At the same time, films deposited at high growth rates have larger surface defects with higher density, though this is at least partially due to the greater thickness of those films. The minority defect signature could therefore be due either to the higher density of structural defects (stacking faults, dislocations, etc.) present in the polycrystalline regions of the surface defects, or due to impurities which only transfer through a solid particulate but are not volatile.

A number of films were grown using a wafer source to test the hypothesis that the minority carrier signal and peak broadening are due to surface defects. The resulting DLTS spectra have no minority carrier signal, and significantly improved fits for the EL2 peak (Fig. 40).

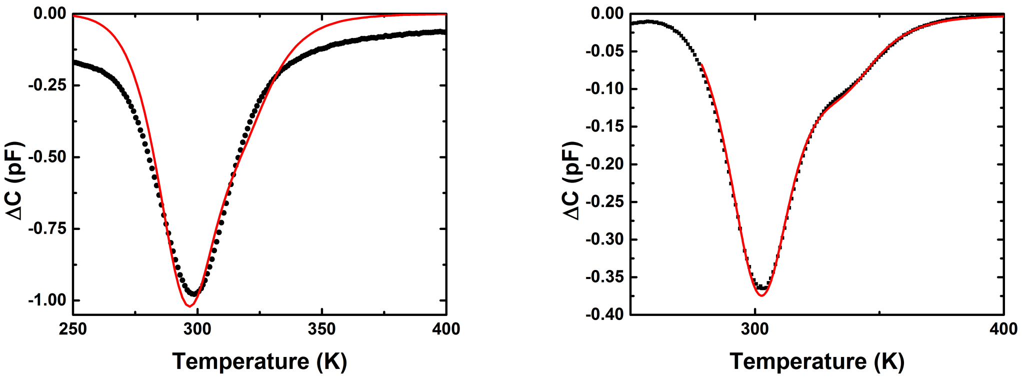

FIGURE 40. Fit to DLTS peaks for two films grown with [H_2O] ~8000 ppm. Left: Peaks for film S1-160903 grown from pellet source, with poor fit ascribed to defect bands associated with surface defects. Right: Peaks for film S3-161011 grown from wafer source with significantly improved fit.

ELO and EL2 Defect Model

Before attempting to calculate defect equilibrium concentrations, it is useful to consider the CSVT process in more detail. In MOVPE or HVPE, the arsenic vapor pressure can be set independently of the source temperature by varying arsine flow rate. For CSVT (assuming near-equilibrium growth conditions) P_{As_2} is set by the source and substrate temperatures, and growth occurs according to Eq. (2.1), where

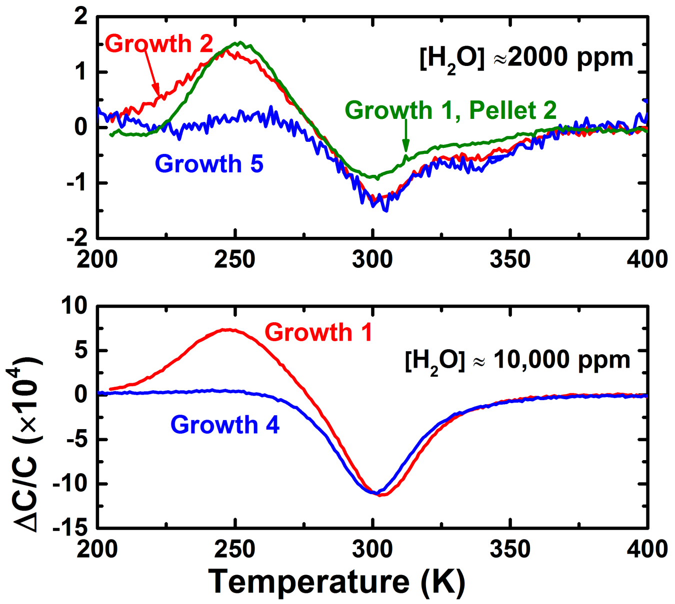

FIGURE 41. DLTS minority carrier peak. Top: DLTS spectra for films grown with [H_2O] 2000 ppm. Bottom: DLTS spectra for films grown with [H2O] 10000 ppm. The minority peak decreases between successive growths from the same pellet regardless of water vapor concentration.

the equilibrium constant is given by

$$K_{eq} = \exp\frac{-G}{kT} = \frac{P_{Ga_2O}P_{As_2}}{r} \tag{5.1}$$

An analogous reaction can also be written for the formation of As_4 and this should be considered since it also consumes Ga_2O and affects the equilibrium in Eq. (2.1). Eq. (2.1) will be used as a first approximation in the following analysis since As_2 is more prevalent than As_4 at typical growth temperatures. In the model of Cote and Dodelet [18], $r = P_{H_2}/P_{H_2O}$ is assumed to be constant throughout the reaction zone, and GaAs is assumed to be etched/deposited congruently (i.e., no reactants are deposited outside the reaction zone) such that $P_{Ga_2O}(T) = P_{As_2}(T) = P(T)$.

Congruent transport suggests that P_{As_2} depends on P_{H_2O}, which has implications for the formation of $\mathrm{As_{Ga}}$ as discussed below.

The concentration of neutral $\mathrm{As_{Ga}}$ can be calculated using the model of Hurle [86, 108, 109] as

$$[As_{Ga}] = \bar{K}_{AG} P_{As_2} \tag{5.2}$$

with the equilibrium constant given by

$$\bar{K}_{AG} = \exp \frac{T\Delta S - \Delta H}{kT} \tag{5.3}$$

Using $\Delta S = -3.17 \times 10^{-3}\,\mathrm{eV\,K^{-1}}$ and $\Delta H = -2.18\,\mathrm{eV}$ [86], $[\mathrm{As_{Ga}}]$ tends to decrease with increasing temperature if P_{As_2} is kept constant. For equilibrium with GaAs at 850 °C (neglecting reaction with water vapor), $P_{As_2} = 0.0027\,\mathrm{atm}$ [110] which is similar to that expected given the $\mathrm{AsH_3}$ flow for HVPE growth in [86]. Using Hurle's model, the neutral $\mathrm{As_{Ga}}$ concentration can be calculated assuming that P_{As_2} is set by equilibrium at the source or substrate temperature. This is shown in Fig. 42 alongside experimental data for HVPE and MOVPE films, and the CSVT films from this study (using an error weighted average for the films grown with identical nominal conditions).

As mentioned, $P_{Ga_2O} = P_{As_2}$ is assumed in the growth model. Since growth is limited by Ga transport, this means that the actual P_{As_2} must be different than its equilibrium value in the absence of water vapor. This explains both the slight change in [EL2] with $[\mathrm{H_2O}]$ and the decrease in [EL2] at lower growth temperatures, where P_{Ga_2O} is also decreased. The fact that [ELO] reaches values much higher than $[\mathrm{As_{Ga}}]$ calculated by the model suggests that P_{As_2} is higher in the presence of water vapor than without, assuming that ELO is a complex with $\mathrm{As_{Ga}}$. While [EL2] is almost independent of [H2O] at $T_{sub} = 830\,^{\circ}\mathrm{C}$, it is strongly dependent on [H2O] for growths from a wafer source at $T_{sub} = 780\,^{\circ}\mathrm{C}$. Further work would be necessary to determine if this is due to the use of a wafer source or due to the lower growth temperature.

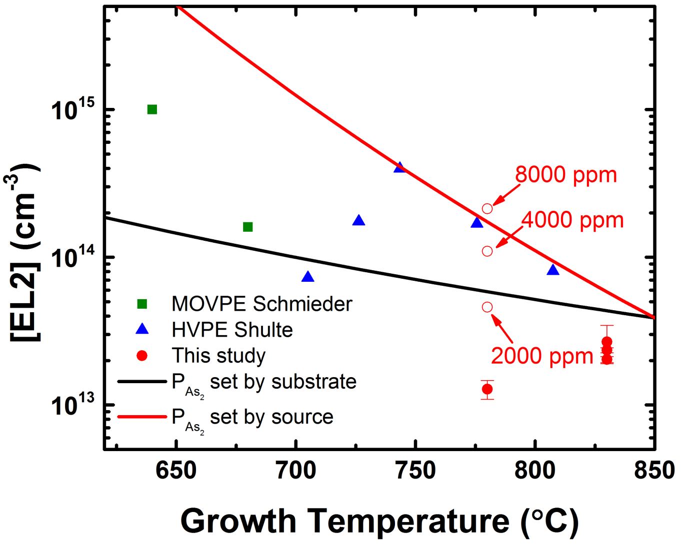

FIGURE 42. Concentration of the neutral As antisite. Solid lines are the theoretical curves assuming equilibrium As_2 values for the source (upper red) and substrate (lower black). Measured data points are plotted from [85] for MOVPE films grown at $56\,\mu\mathrm{m\,h^{-1}}$, from [86] for HVPE films at constant P_{AsH_3}, and this study with constant $T_{src} = 850\,^{\circ}\mathrm{C}$. Open symbols represent films grown from a wafer source, with $[H_2O]$ indicated.

We can also consider the formation of O_{As} in a similar manner. If we assume that the growing surface is near equilibrium with the gas phase, then a number of mass-action formulas can be written. The equilibria for substitutional and interstitial oxygen defects are:

$$\mathrm{H_2O} + \mathrm{V_{As}} = \mathrm{O_{As}} + \mathrm{H_2} \tag{5.4}$$

with the mass-action formulas

$$[\mathrm{O_{As}}] = \mathrm{K_s}\,[\mathrm{V_{As}}]\mathrm{r}| \tag{5.5}$$

$$[\mathrm{O_i}] = \mathrm{K_i\, r} \tag{5.6}$$

We have also assumed that the interstitial is not detected by DLTS, while the ELO peak arises from the substitutional, and therefore we would assume that the concentration of ELO is equal to the concentration of $\mathrm{O_{As}}$. The concentration of As vacancies can be related by

$$\frac{1}{2}\,\mathrm{As_2\,(g) = As_i} \tag{5.7}$$

$$\mathrm{As_{As} = As_i + V_{As}} \tag{5.8}$$

such that

$$[\mathrm{V_{As}}] = \mathrm{K_{av}K_{ai}}^{-1}\mathrm{P_{As_2}}^{-1/2} = \mathrm{K_{av}K_{ai}}^{-1}\mathrm{K_{eq}}^{-1/4}\mathrm{r}^{-1/4} \tag{5.9}$$

Combining Eq. (5.5) with Eq. (5.9) predicts a dependence of $r^{3/4}$ on [ELO]. However, empirically we find that the actual dependence is best fit for r^n with $n \approx 1.8$. This could be explained if ELO is not an isolated $\mathrm{O_{As}}$ but is instead a complex with two As antisites, which is the most energetically favorable defect complex as predicted by Colleoni and Pasquarello [96]. In that case, the corresponding equilibrium and mass action formula for the complex formation are

$$\mathrm{O_{As} + 2\,As_{Ga} = O_{As2}As_{Ga}} \tag{5.10}$$

$$[\mathrm{O_{As2}As_{Ga}}] = \mathrm{K_{OG}}[\mathrm{O_{As}}][\mathrm{As_{Ga}}]^2 \tag{5.11}$$

Since $[O_{As}]$ is proportional to $r^{3/4}$ and $[As_{Ga}]$ is proportional to $r^{1/2}$ this gives an overall $r^{7/4}$ dependence. Fits to this model are shown in Fig. 43. However, the largest [ELO] values are over an order of magnitude higher than $[As_{Ga}]$ expected based on equilibrium calculations. This suggests that the addition of water vapor significantly increases the As_2 partial pressure compared to its value above GaAs in an inert ambient.

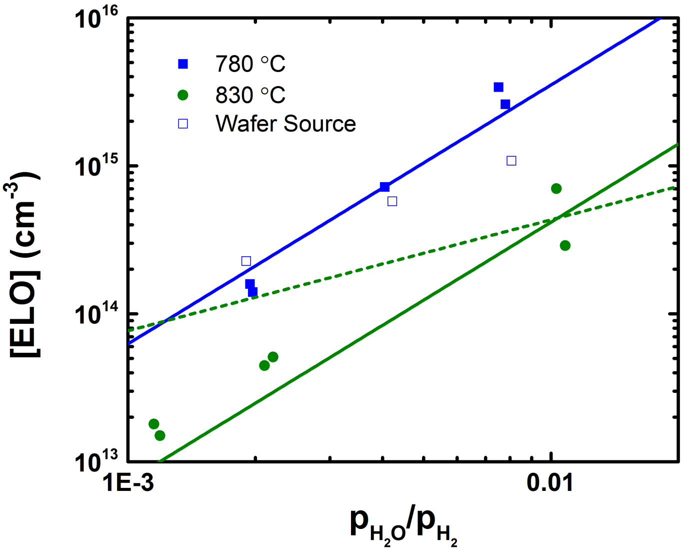

FIGURE 43. [ELO] concentrations as a function of r. All films were grown with $T_{src} = 850\,°C$. Green circles are for films grown at $T_{sub} = 830\,°C$ and blue squares are for films grown at $T_{sub} = 780\,°C$. The solid lines have a slope of 1.75 while the dashed line has a slope of 0.75 and is shown for comparison.

Defects in *p*-type CSVT GaAs

Three distinct peaks have been detected in DLTS of a few of the n^+p junction solar cells. The peaks are shown for one device in Fig. 44 along with the Arrhenius plots with the trap parameters. Though no trends have been established between these peaks and growth parameters, we have assigned tentative chemical origins based on published literature (see the Appendix for a list of published trap signatures). The highest temperature peak is most closely matches HB3 and HL2, which are associated with Fe. A likely source of contamination is the stainless steel screws used to attached the graphite heaters. The middle peak most closely matches HB4 and HL4, and is probably due to copper transported from the wiring. The origin of the lower temperature peak is still unknown but will have less of an impact on carrier lifetimes since it is relatively shallow and has a lower concentration than the other two. The concentration of Cu and Fe in this sample is quite high and would be expected to have significant impact on the carrier lifetimes.

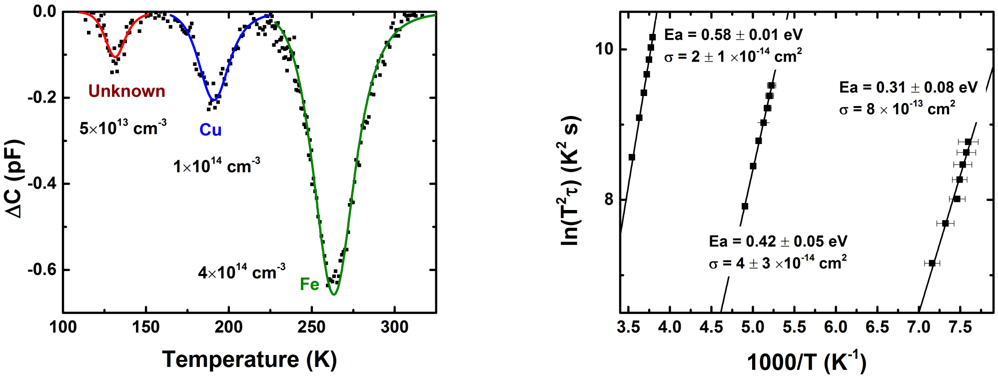

FIGURE 44. *p*-type DLTS spectrum. Left: DLTS spectrum of *pn* junction sample S1-150724 with curve fits, approximate trap concentrations, and possible chemical origins indicated. Right: Arrhenius plots for the three peaks with extracted peak parameters.

TPC Comparison of GaAs Deposited by Various Methods

To date, no III-V materials have been studied using TPC and TPI, though a number of reports have studied the optical absorption of bulk material, particularly to observe the magnitude of the EL2 defect which has an identifiable metastability signature [111]. Since TPC and TPI are used on completed solar cells, it can be a useful tool to study the effects of the later stages of processing such as epitaxial liftoff (ELO), in which the thin film is released from the wafer substrate by lateral etching of a sacrificial layer. To establish a baseline for comparison, several GaAs homojunction cells were examined by TPC and TPI. Each cell had an N+/P architecture, with similar doping of 10^{17}cm^{-3} for the absorber. HVPE and MBE samples were fabricated at NREL, while an MOVPE ELO cell was provided by Microlink Devices, and CSVT cells were fabricated at UO. The HVPE, MBE, and CSVT samples contained several mesa-etched cells, and for each of these a cell with $V_{oc} > 0.9$ mV was chosen to minimize effects of defects caused by sample processing rather than the growth technique. This also insured that the cells under study had high shunt resistance, which is important to acquire low noise TPC and TPI spectra and allows for a larger range of voltage biases to be probed.

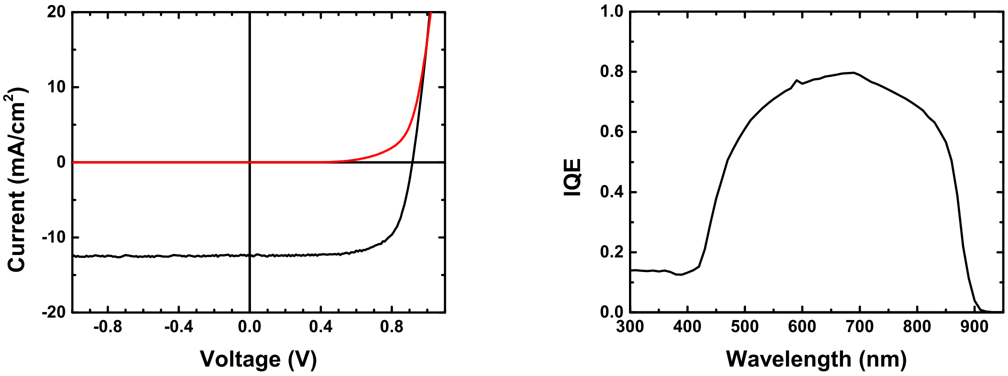

FIGURE 45. Dark and one-sun current-voltage and internal quantum efficiency. Curves are for a CSVT device for which TPC spectra were collected.

TPC spectra for an HVPE cell are shown in Fig. 46. The prominent feature is a defect band centered at 0.710 eV associated with a minority (electron) trap. The spectrum is completely flat over a large range of optical energies, indicating that no other centers are detected between 0.710 eV and the band edge. In this case, since the lightly doped side of the junction is p-type, holes are captured during the filling pulse and the transient corresponds to thermal emission of these holes to the valence band, which is enhanced by light absorption. The relative defect signal decreases at elevated temperatures, possibly due to competition of emission of electrons to the conduction band.

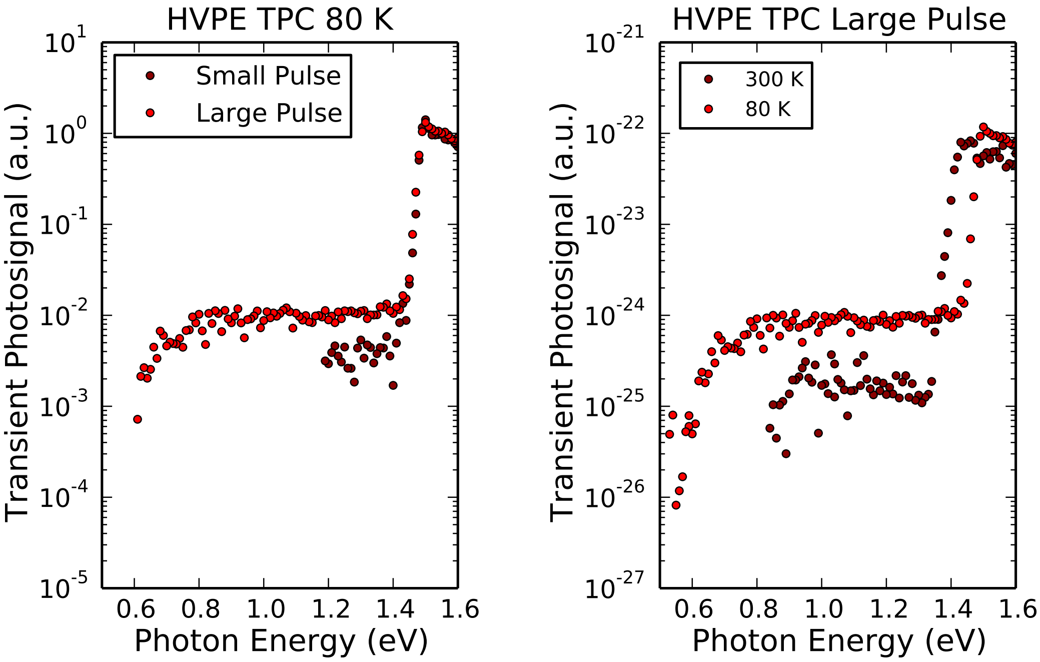

FIGURE 46. HVPE cell TPC spectra. Left: TPC collected at 80 K for an HVPE cell with pulses from -0.1V to 0V and -1V to 0V. Right: Comparison with TPC spectrum taken at 300 K with the large voltage pulse.

Transient photocapacitance (TPC) and photocurrent (TPI) spectra were measured at 80 K and 300 K for cells grown by MOVPE, MBE, HVPE, and CSVT. All of the devices show an optically enhanced capacitance and current transient corresponding with majority carrier (hole) emission. The most striking characteristic is an 80 K TPC defect band in the MOVPE and HVPE devices, which correspond to a Gaussian density of states centered at 0.71 and 0.72 eV above the valence band respectively. The additional similarity in the TPI spectra between the HVPE and MOVPE cells provides additional evidence that the absorber material quality is similar between the two growth methods, despite a discrepancy in their power conversion efficiencies (PCEs) (the MOVPE cell has PCE ~20 % due to its AR coating and passivation). In contrast, the TPC spectrum for the CSVT cell is not fit well to a single Gaussian, which suggests a number of defect centers may be active at similar concentration, consistent with the DLTS results.

CSVT and MOVPE Cells

All of the cells are n^+p architecture, with similar absorber doping ($\sim 10^{17}$ cm^{-3}) and with $V_{OC} > 0.9$ V. The CSVT cell was only 1 micron thick, and there is a broadening of the band tail region for the transient photocurrent (TPI) spectra which appears to originate from carriers generated in the substrate or at the interface with the substrate (see Fig. 48a). A similar broadening might be occurring in the MBE cell though less pronounced. The MOVPE cell is an epitaxial liftoff (ELO) device and therefore has no substrate contribution.

TPC Results

The best transient photocapacitance (TPC) spectra were collected at 80 K and are shown in Fig. 47. At 300 K, TPC signal is suppressed for all the devices owing to the better minority carrier collection at higher temperatures; signal in TPC is proportional to $p - n$, the number of majority carriers minus the number of minority carriers which are collected from the depletion region in the time scale of the measurement.

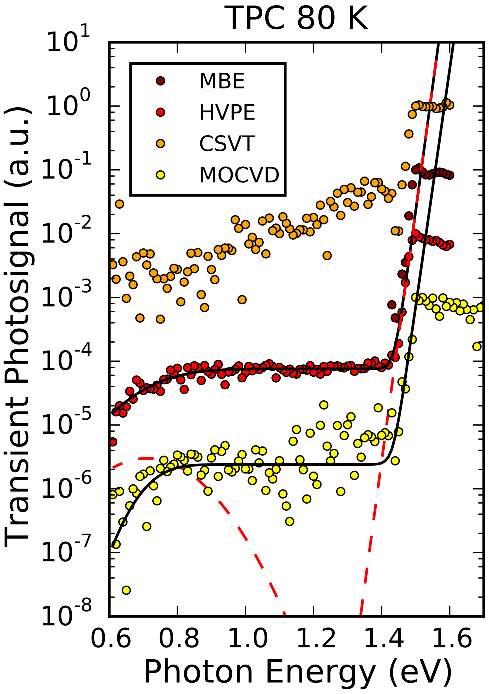

FIGURE 47. TPC spectra taken at 80 K for different cells. Curves are offset for clarity. Defect band and Urbach edge fits for the MOVPE and MBE cells are shown as solid curves, and the corresponding optical DOS (in arbitrary units) for the HVPE cell is shown as a dashed curve. Pulsing conditions were not identical leading to different sensitivities for detecting defect bands.

At 80 K, the HVPE response is remarkably constant over a large range of energies, which suggests that the response is dominated by a single defect center at those energies. Though the MOVPE response is noisier, it has a very similar defect band centered at approximately the same energy (0.72 eV). In all cases, the TPC signal is positive, which corresponds to a majority carrier (hole) transition in which a hole is optically excited into the valence band from the defect band. It was observed in the HVPE cell that the magnitude of this defect band increases with increased bias pulsing, and it may be possible to extract a defect concentration from the bias dependence of the pulse, assuming the concentration is spatially uniform. It is also important to note that the voltage bias conditions in Fig. 47 were not identical for all the samples, and the HVPE cell was subjected to a larger bias pulse than the other samples.

TPI Results

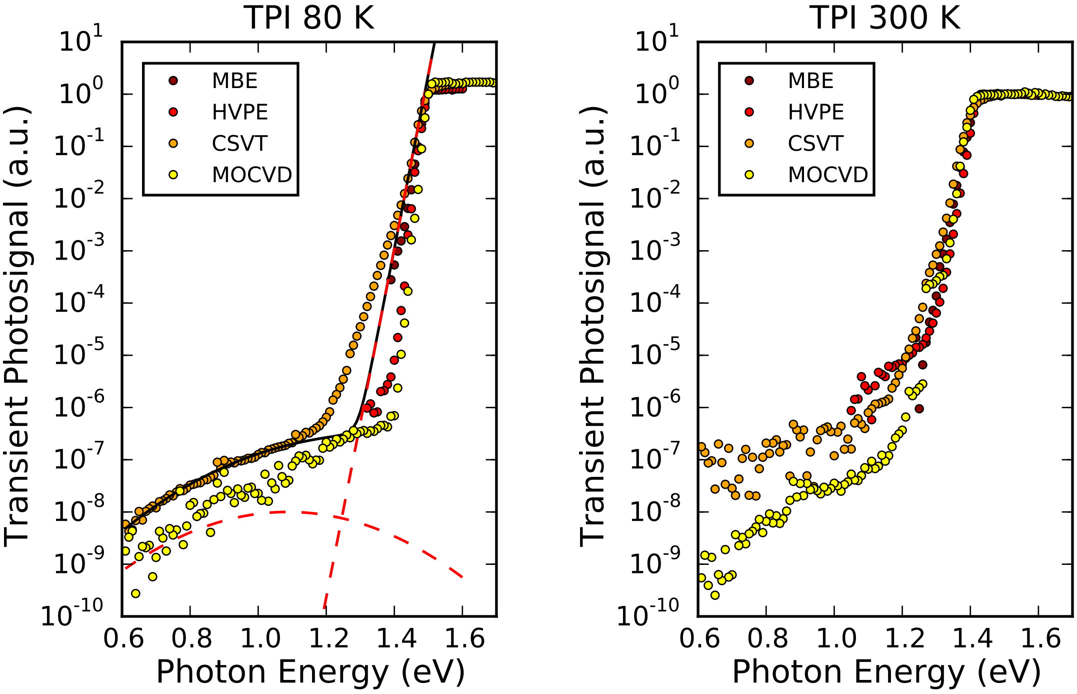

(a) (b)

FIGURE 48. TPI spectra at different temperatures. Curves are collected at (a) 80 K and (b) 300 K for the different cells, in this case aligned to the above gap response. The fit to the 80 K CSVT spectrum (solid curve) and density of states (dashed line) is also shown. The jump in the 300 K MOVPE spectrum at 1.27 eV is due to stray above gap light.

The signal to noise ratio was not high enough for the HVPE cell to determine a fit for the defect band in TPI, though it appears qualitatively different than the TPC defect band. One obvious feature in the TPI for CSVT cells is the broadened band edge. The fact that this does not appear in the ELO device suggests that it is associated with defects in the GaAs substrates, most likely dislocations or other structural/intrinsic defects that occur during melt growth. It does not appear in the TPC spectra, most likely because carriers *emitted* from defects in the substrate will not affect the depletion width (and capacitance), while carriers absorbed in the substrate near the growth interface may diffuse to the junction and contribute to the photocurrent. A TPI spectrum for a cell fabricated with a CSVT emitter and a wafer absorber ($n \approx 5 \times 10^{17}\,\mathrm{cm}^{-3}$) is shown in Fig. 49 and shows that the broadening is much more pronounced when the entire depletion region exists within the substrate.

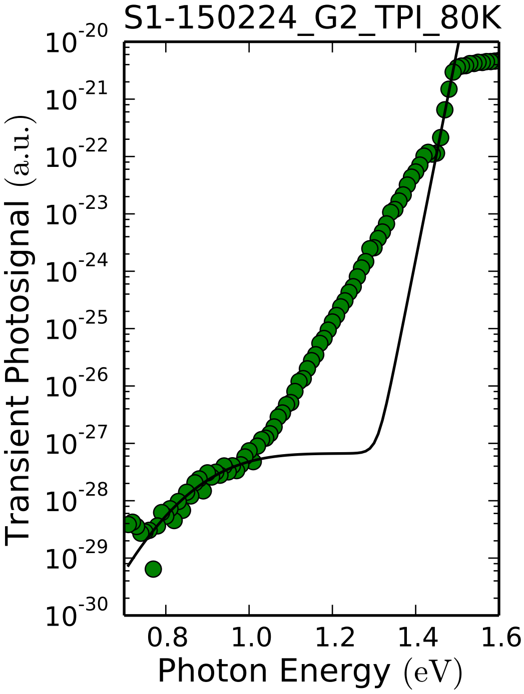

FIGURE 49. TPI of device with wafer absorber. The band edge broadening is much more pronounced, indicating it is associated with the substrate.

Defect Bands and Urbach Energies

A summary of the fits to the spectra is shown in table 5. The Urbach energies were calculated from a fit between 1.43 and 1.49 eV at 80 K and 1.32 eV and 1.39

eV at 300 K. The Urbach energies for the CSVT devices are slightly overestimated due to the bandtail broadening from the substrate, though the energy range chosen for the fit minimizes this effect.

TABLE 5. Defect band and Urbach energy fits

Cell	Spectra	E_d (eV)	FWHM (eV)	E_u (meV)
HVPE	TPC 80 K	0.71	0.17	11.1
HVPE	TPI 80 K	ND	ND	8.8
HVPE	TPI 300 K	NF	NF	11.5
MOVPE	TPC 80 K	0.72	0.09	11.9
MOVPE	TPI 80 K	~1.1eV*	*	6.7
MOVPE	TPI 300 K	NF	NF	9.8
MBE	TPC 80 K	ND	ND	9.8
MBE	TPI 80 K	ND	ND	10.7
MBE	TPI 300 K	ND	ND	13.2
CSVT	TPC 80 K	NF	NF	10.9
CSVT	TPI 80 K	1.09	0.30	14.1
CSVT	TPI 300 K	NF	NF	14.0

ND: Not detectable
NF: Not fit–poor fit to single Gaussian band
*Unreliable–affected by stray light

The most obvious candidate for the defect detected in the MOVPE and HVPE samples is EL2. The band gap of GaAs is $\sim$1.5 eV at 70 K, so the energetic location of 0.7 eV above E_v is in good agreement with the DLTS value of 0.8 eV below E_c. Furthermore, a direct comparison can be made between published absorption data for bulk *p*-type GaAs, as the TPC signal is proportional to the number of photons absorbed:

$$P(\lambda) = \Delta p \approx A \Delta t I_0 (1 - e^{\alpha(\lambda) x_d}) \tag{5.12}$$

where $P(\lambda)$ is the wavelength-dependent TPC signal, A is the illuminated area, Δt is the time during which the sample is illuminated, I_0 is the flux incident on the surface of the sample, α is the absorption coefficient, and x_d is the depletion width (since only absorption within the depletion region will contribute to the signal). The depletion width is calculated from a CV measurement, and ignoring the constant value $A\Delta t I_0$, a TPC equivalent signal can be directly calculated from the absorption coefficient which may be measured on a bulk sample. A comparison is shown in Fig. 50. The sub-bandgap absorption coefficient data was measured at 5 K for p-type Bridgman-grown GaAs material by Skowronski [99] with features which were attributed to the EL2 center.

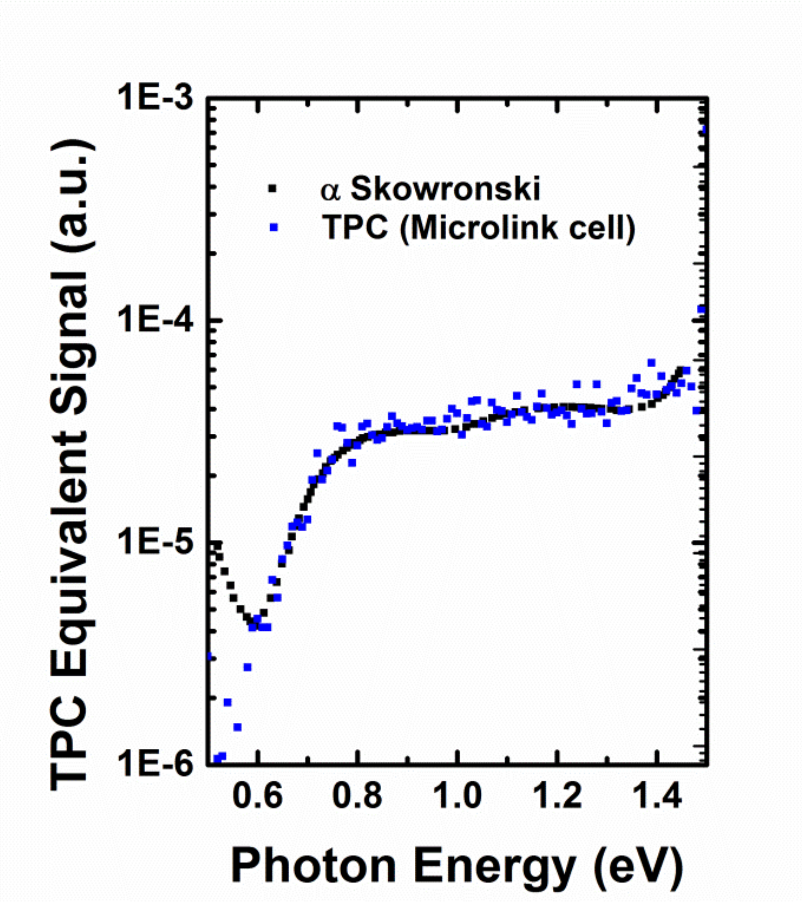

FIGURE 50. TPC equivalent signal calculated from absorption data extracted from [99] for Bridgman grown bulk p-type GaAs at 5 K overlaid with TPC data collected at 80 K for an epitaxial liftoff GaAs solar cell fabricated by Microlink, with p-type absorber. The absorption features in [99] are attributed to transitions involving the EL2 center suggesting the defect band detected in TCP is also due to EL2.

Defect Study Conclusions

Notably, the MOVPE cell has the smallest Urbach energies extracted from TPI (6.7 meV at 80 K and 9.8 meV at 300 K). Smaller Urbach energies are typically associated with lower structural and thermal disorder, and in polycrystalline materials has been correlated with the open circuit voltage deficit [54]. Urbach energies extracted from TPC are subject to larger uncertainty in this case due to the lower signal to noise ratio, which might explain why they do not show a significant trend across growth techniques.

Using variable bias pulse conditions could allow a direct comparison of the defect concentrations by calculating the change in the depletion width and defect band magnitude. Additionally, it might reveal a defect band in the MBE cells for which the sensitivity was not as good. This would be useful to better establish whether the TPC/TPI response of the MBE cell is similar to the MOVPE and HVPE cells, which might not be expected since the growth technique is very different. The ability to measure [EL2] using TPC could be useful in a manufacturing environment, since it would not require acquisition of an entire spectrum but only a data point at one sub-gap energy and a few voltage biases.

Overall, the defect character of H_2O-mediated CSVT GaAs films is quite interesting in comparison with MOVPE and HVPE films. It might be expected that the use of H_2O would cause the films to invariably have high concentrations of O, which would degrade the performance too much for the films to be of use in PV devices. However, as we have shown, ELO can be controlled over a rather wide range of concentrations depending on the growth conditions. This electron trap is the most sensitive to changing [H_2O] and most likely involves O_{As}; this is in contrast to previous reports linking EL3 to O_{As}. It is possible, however, that EL3 is related to some impurity that transports more efficiently with increased [H_2O] or which complexes with O. ELO is detected at highest concentrations for growths at lowest temperatures, reaching $3 \times 10^{15}\,\mathrm{cm^{-3}}$ at 780 °C and [H_2O] = 8000 ppm. The solubility limit of oxygen in GaAs is not precisely known, but is likely below $1 \times 10^{16}\,\mathrm{cm^{-3}}$ [112–115], so the concentrations detected are consistent with the observation of oxide phases in solar cell emitters grown at low temperature.

A secondary goal of this study was to determine the impact of source reuse on DLTS spectra. While the reuse was limited in this study, it is interesting to note that the concentrations of the unidentified traps decrease when the source material is reused. This might indicate that impurities introduced during grinding or handling of source wafers are gradually transported and deposited elsewhere in the reactor or are somehow chemically passivated during growth cycles. It is also encouraging that the ELO and EL2 concentrations were reproducible after source cycling, suggesting that small changes in stoichiometry of the source due to As loss have little impact on the film quality. In a manufacturing process, source material would most likely be recycled but this indicates that a large fraction of the source might be used before recycling is necessary.

The EL2 and ELO concentrations reach values lower than those found in MOVPE or HVPE films, so there is currently no reason to believe minority carrier lifetimes in H2O-mediated CSVT films must necessarily be lower than those achieved in MOVPE or HVPE. Considering the need for high growth rates, however, [H_2O] must be substantial or growth temperatures and temperature gradient must be high. At high temperatures ELO is suppressed and the overall concentration of [ELO] + [EL2] is comparable to the value of [EL2] found in MOCVD and HVPE films, so high temperature growths provide the best material quality. The ELO defect could be eliminated entirely by using HCl as a transport agent in place of H_2O, and this is also motivated by the difficulties in Zn-doping using H_2O. However, based on the model presented here, ELO appears to be a complex with As_{Ga}, so changing transport agents would cause a commensurate increase in [EL2]. Thus, high growth temperatures might still be required to minimize [EL2] in an HCl-based process.

Optimizing growth conditions in H_2O-mediated CSVT is complex challenge that involves tradeoffs between growth rate and defect concentrations. [H_2O] should be limited to moderate values since gains in growth rate from increased [H_2O] can easily be offset by increases in [ELO]. Substrate temperatures above 800 °C are probably necessary to limit both EL2 and ELO formation, and these elevated temperatures also increase growth rate. Defect concentrations do not appear to be strongly linked to source-substrate spacing, so the best strategy for achieving high growth rate is to use the smallest spacing possible, though this ultimately will limit the maximum achievable temperature gradient and therefore has an optimal value. Following these guidelines, it is likely that growth rates and defect densities similar to those found in MOVPE and HVPE films can be achieved using CSVT.

Bridge

While both morphological and microscopic defect concentrations can be minimized in homojunction GaAs cells, it remains to be seen if CSVT can be cost-competitive with commercialized deposition techniques. In particular, commercialized III-V solar cells employ additional layers (e.g., ternary III-V materials) that have not yet been demonstrated or optimized using CSVT. The cost of the substrate used in the current study is also substantial. The next chapter discusses future directions for CSVT growth which could address these concerns.

CHAPTER VI

FUTURE DIRECTIONS

Portions of this chapter were taken from Boucher, J.W.; Greenaway, A.L.; Ritenour, A.J.; Davis, A.L.; Bachman, B. F.; Aloni, S.; and Boettcher, S.W. Low-Cost Growth of III-V Layers on Si Using Close-Spaced Vapor Transport. It was written entirely by me with editorial assistance of my co-authors. Data was collected by myself or B.F.B under my direction.

Multi-junction designs

While single junction GaAs solar cells have been commercialized, the cells on the market today are all ELO devices which are desirable because they are flexible and lightweight. Additionally, the limiting efficiency for a non-concentrated GaAs solar cell is only 30 %. Since low-cost growth methods for III-V are still in their infancy, other technologies may exceed this efficiency before single-junction GaAs could be cost competitive for large-scale energy generation. CSVT is therefore most desirable if it can be used to produce multijunction devices with higher theoretical efficiencies, and there are a number of possible approaches for that goal.

Multi-junction devices have been fabricated in a number of different ways. In many cases, they are grown monolithically, but high-efficiency devices have also been produced by mechanical stacking and in a process called wafer bonding. WHen they have only two terminals and the junctions are connected in series, the device must be designed such that current from each cell is approximately the same, as overall current is limited by the subcell that produces the least current. In other cases, three or more terminals may be used such that devices can generate current independently.

Needless to say, these different device architectures produce very different constraints on the choice of material. Mechanically stacked devices are less constrained by the lattice constant of the different layers, and three or four terminal devices are less constrained by band-gap and current matching.

Monolithic, two-terminal devices are advantageous because they require only a single substrate, which is a significant part of the cost of a cell. Architectures with additional terminals also require more complicated interconnects. However, in monolithic designs the materials must be chosen carefully to minimize defects which can form during heteroepitaxial growth. These defects form due either to lattice-mismatch or due to the growth of a polar semiconductor (from the III-V family) on non-polar semiconductor (from the group IV family). In the former case, defects called dislocations (missing rows of atoms) form due to the strain in the crystal once the layer reaches a critical thickness. In the latter case, defects called antiphase boundaries can form since, roughly speaking, growth can be initiated in different locations with either the group III or the group V element when growing on a group IV substrate.

Fig. 51 shows the lattice constant and band gap curves for $\mathrm{In}_x\mathrm{Ga}_{1-x}\mathrm{P}$ and $\mathrm{GaAs}_x\mathrm{P}_{1-x}$ along with the values for Si and Ge. The GaAs lattice-matched composition for $\mathrm{In}_x\mathrm{Ga}_{1-x}\mathrm{P}$ is also indicated, as this is particularly useful since it can be grown on GaAs substrates with minimal defects. Due to the lattice matching, three-junction InGaP/GaAs/Ge cells have been fabricated and in fact used to hold the record one-sun cell efficiency [116] though this has been superceded by a InGaP/GaAs/InGaAs cell [117].

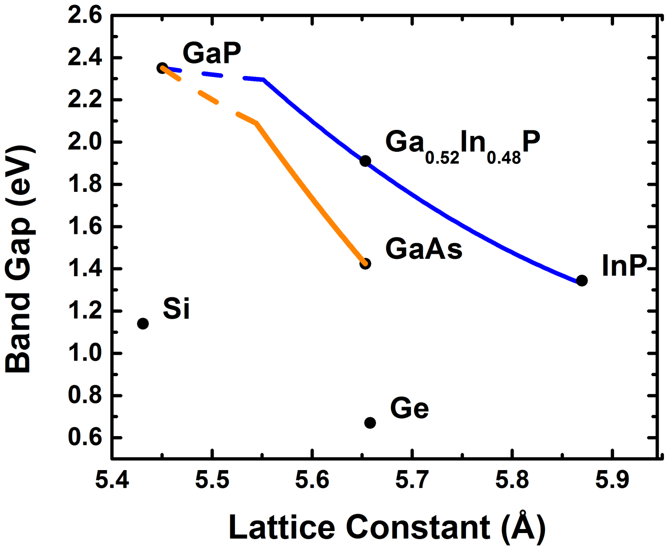

FIGURE 51. Lattice constant and band gap for several relevant PV materials.

Growth of Ternary III-V Alloys

One possible device architecture is to use $GaAs_xP_{1-x}$ with appropriate band gap in a tandem device with a Si bottom cell. Such a structure could in theory leverage existing Si fabrication facilities and would have a maximum efficiency >39 % [118] Both $In_xGa_{1-x}P$ and $GaAs_xP_{1-x}$ can be growth by H_2O-mediated CSVT, though the primary challenge is the control of composition. Growth of $GaAs_x$P1-x by CSVT has been reported in several studies using H_2O [119, 120] and $ZnCl_2$ [27] as transport agents. Source material in these studies is prepared by mixing GaP and GaAs powders.

We have reported more extensive electronic characterization of $GaAs_xP_{1-x}$ films grown on GaAs and found reasonable electronic quality despite the significant lattice-mismatch [67]. Moreover, composition was relatively well-controlled; after an initial annealing step, films had essentially constant composition when grown at the same temperature. Nevertheless, some P loss was observed, indicating that source material would require recycling after a number of growths, or an additional P source would need to introduced into the reactor.

To the best of our knowledge, growth of $\mathrm{In}_x\mathrm{Ga}_{1-x}\mathrm{P}$ by CSVT has not been previously reported, although both InP [121] and GaP [122] have been grown by CSVT. Growth of this material is desirable not only because it can be used in a multijunction device, but also because it has been used as a passivating layer for GaAs solar cells, for instance as reported in recent HVPE work [7]. Unfortunately, this is inherently more challenging than growing $\mathrm{GaAs}_x\mathrm{P}_{1-x}$ since it must be lattice-matched for full benefit. Also, growth of InP and GaP have previously been performed at very different temperatures and this appears to be problematic as In transports at a higher rate than Ga over the full temperature range we have studied. Fig. 52 shows how the composition of films changes as a function of source and substrate temperature for a source pellet with $x \approx 0.5$. At low temperatures, only In transports, whereas at high temperatures the film is still not lattice-matched to GaAs.

Substrate Cost

Single-crystal GaAs substrates are too expensive for non-concentrator applications unless they are reused many times. Many multijunction cells are grown on Ge substrates, but these are also too expensive. Si substrates are the cheapest single-crystal option, but as shown in Fig. 51 the lattice mismatch is too large to grow high quality III-V films easily. Several approaches have been used, however, with varying success. One such method is to grow a a buffer layer of Ge, which is then annealed to cause dislocations to annihilate near the interface. The process is further improved by patterning the Ge into small islands, such that the thermal strain introduced (which can cause film cracking) is minimized and at the same time

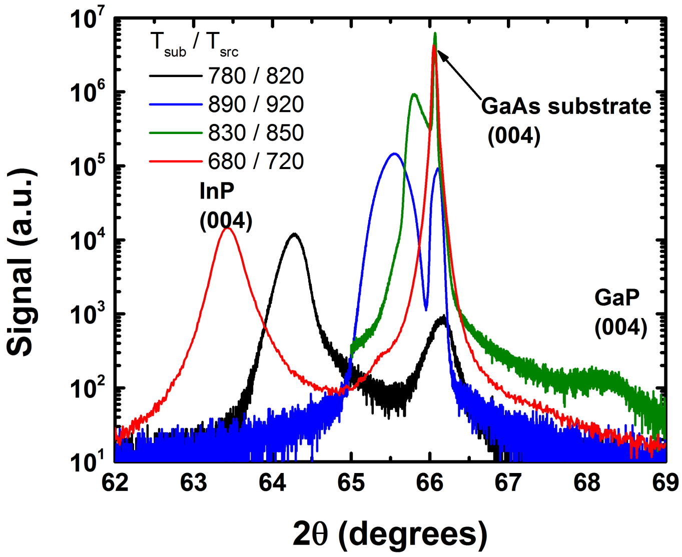

FIGURE 52. XRD of $In_xGa_{1-x}P$ films. Coupled scans aligned to the (004) peak for films grown on (001) GaAs. The trends are consistent with the literature which indicates GaP transports only at high temperatures.

dislocations are more likely to terminate at the edge of an island rather than the surface.

Growth on such islands has also allowed us to identify the ideal nucleation conditions simply based on morphology. Specifically, it has been reported that a "temperature inversion" step is required to grow GaAs epitaxially on Ge using CSVT. During this step, the substrate is held at a higher temperature than the source, driving off the native oxide. The resulting structures grown on Ge islands have more regular facets, as shown in Fig. 53.

These "virtual Ge" substrates are not perfect, however, as the Ge layer parasitically absorbs much of the light that would be absorbed in the Si. Fig. 54 shows the amount of light transmitted by a continuous, planar film of Ge as a percentage of thickness, using absorption coefficients found in [59]. The calculation is performed assuming AM1.5G light in the range of 0.73–1.12 µm is usable for the Si bottom cell (i.e., a 1.7 eV top cell absorbs light below 0.73 µm and light below the Si band gap is not absorbed by the bottom cell). Thicknesses of 50 nm are practical to grow, and transmit ~85 % of the usable light, but it is unlikely that this thickness would be sufficient for dislocations to terminate at the edge of islands during annealing processes.

Growth of GaAs directly on Si using CSVT has also been reported [123], though these claims are dubious as in our own studies we have found that growth is inhibited by formation of a stable oxide layer on the surface of the Si. Growth of Ge, in contrast, can procede because the oxide is volatile, and in fact there are reports of Ge epitaxy by H_2O-mediated CSVT [124]. Using an alternate transport agent could prevent this oxide formation, however, and could enable growth of III-V layers directly on Si.

HCl as Transport Agent

There are few reports of HCl being employed for vapor transport of GaAs [125], and to our knowledge no reports of HCl-mediated CSVT of GaAs except indirectly using $ZnCl_2$ [126]. Still, the chloride transport of Ga and other group III elements is well-established, both in reactors using $AsCl_3$ [127] and in HVPE [7]. In addition to allowing growth directly on Si, an HCl-based process is attractive due to the increased volatility of metal chlorides compared to metal oxides and for eliminating oxide precipitates, as mentioned in Chapter IV.

We have begun the design and construction of a deposition system compatible with HCl. This system will also be capable of depositing films from up to three different sources, without exposing the source or substrate to atmosphere. The spacing of the source and substrate in this reactor will be achieved using precision-machined graphite parts, allowing for better gas confinement and film uniformity.

As mentioned in Chapter V, it is expected that films grown in the new reactor will have a different defect character than those grown by the H_2O process. The ELO peak should be entirely eliminated in DLTS spectra, while the EL2 peak may grow substantially. Extrinsic impurities such as Fe and Cr, may still be incorporated in films due to corrosion of the deposition chamber, though this will hopefully be avoided by water-cooling the chamber walls, and constructing the hot region almost entirely of graphite or carbon composites. Overall, an HCl-based process should increase the flexibility of CSVT, allowing better transport efficiency for dopants and group III elements without sacrificing materials utilization or film quality.

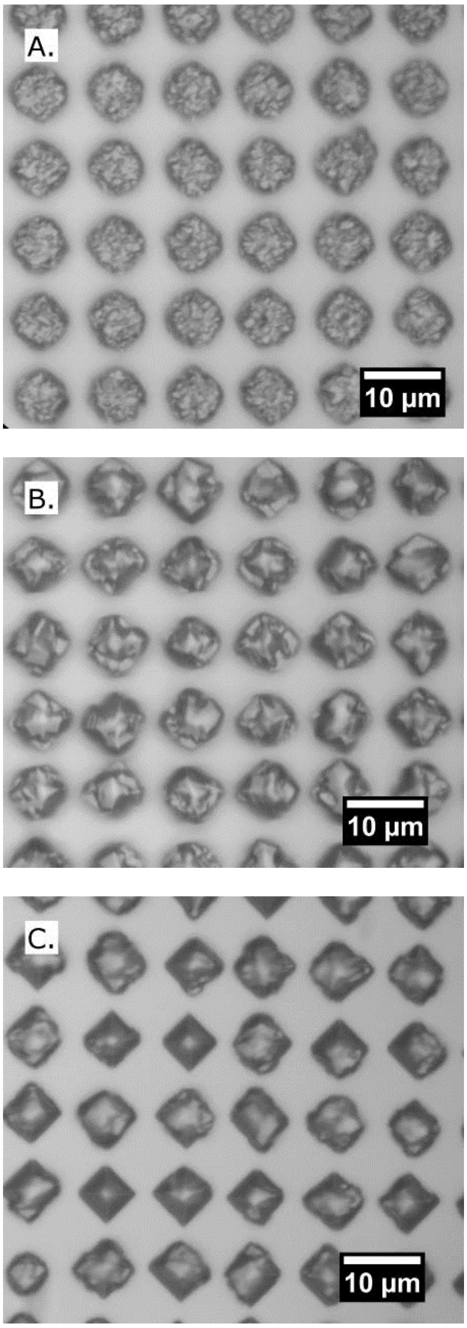

FIGURE 53. Optical microscope image of GaAs islands grown on 5 μm square Ge islands on (100)-oriented Si. A) No temperature inversion step. B) Temperature inversion for 8 min. C) Temperature inversion for 8 min with water vapor injected just prior to the end of the temperature inversion step.

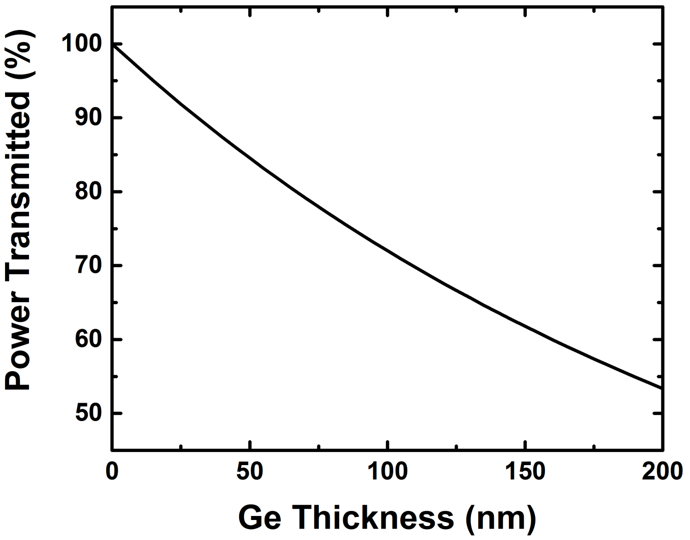

FIGURE 54. Light transmitted through a continuous Ge interlayer as a function of thickness, assuming a top cell with a band gap of 1.7 eV.

APPENDIX

DLTS TRAP PARAMETERS

Tables 6 and 7 give parameters and possible chemical or structural origin (when known) of a number of electron and hole traps which were reported in DLTS studies of GaAs. Growth techniques are also stated where available, as well as the approximate temperature at which a DLTS peak is expected for a given rate window.

TABLE 6. Selected majority electron traps in GaAs.

Label	**E_a (eV)**	**σ_n (cm^2)**	**Possible Origin**	**Growth Technique**	**Approx. Temperature (K)**	**Rate Window (s)**	**Reference**
ELO	0.825 ± 0.005	$(4.8 \pm 0.6) \times 10^{-13}$	$\mathrm{O_{As}}$	Bridgman	350	0.039	[84]
EL2	0.815 ± 0.002	$(1.2 \pm 0.1) \times 10^{-13}$	$\mathrm{As_{Ga}}$	Bridgman	375	0.039	[84]
M1*	0.18	1×10^{-15}	Impurity+Dislocations	MBE	100	0.01	[128–130]
M2*	0.22	$> 4 \times 10^{-17}$		MBE	140	0.01	[128–130]
M3*	0.3	1.5×10^{-14}	Impurity+Dislocations	MBE	175	0.01	[128–130]
M4*	0.5	2.8×10^{-13}	Impurity+Dislocations	MBE	225	0.01	[128–130]
E3**	0.37	$3 \times 10^{-15} - 2 \times 10^{-13}$		MBE	210	0.01	[128]
E4**				MBE	300	0.01	[128]
E5	0.83			MBE	278	0.01	[129]
EL3	0.58	4×10^{-13}	$\mathrm{O_{As}}$		255		[101]
ELCS1	0.78	4.9×10^{-12}		CSVT	300	0.125	[90]
EL5	0.42	5×10^{-15}		VPE	278		[131]
EL11***	0.17	2×10^{-15}		VPE	100		[131]
EC1 (EL2)	0.8	6.6×10^{-14}		Bridgman	380	0.0086	[132]
EC2 (EL3)	0.6	6.4×10^{-13}		Bridgman	270	0.0086	[132]
EC3	0.48	1.35×10^{-14}	Ni	Bridgman	260	0.0086	[132]
EC4 (EL5)	0.37	2.0×10^{-14}		Bridgman	200	0.0086	[132]
EC5 (EL6)	0.35	1.0×10^{-13}	$\mathrm{V_{Ga}}$–$\mathrm{V_{As}}$	Bridgman	160	0.0086	[132]
EC6 (EL9,EL14)	0.215	2.3×10^{-15}		Bridgman	150	0.0086	[132]
EC7 (EL10,EB8)	0.18	1.3×10^{-14}		Bridgman	120	0.0086	[132]

*Reported for GaAs grown on Si [130] as well as homoepitaxially-grown GaAs

**Electron-irradiated GaAs

***Actual (not apparent) capture cross section reported

TABLE 7. Selected majority hole traps in GaAs

Label	**E_a (eV)**	**σ_p (cm^2)**	**Possible Origin**	**Growth Technique**	**Approx. Temperature (K)**	**Rate Window (s)**	**Reference**
HL1	0.886	1×10^{-14}	Cr	LPE	400	0.1854	[133]
HT1	0.44	1.2×10^{-14}		VPE			[134, 135]
HS1	0.58	2×10^{-19}		LPE			[134, 135]
HS2	0.64	4.1×10^{-16}		LPE			[134, 135]
HS3	0.44	4.8×10^{-18}		LPE			[134, 135]
HB1	0.78	5.2×10^{-16}	Cr	LPE			[134, 136]
HB2	0.71	1.2×10^{-14}		LPE			[134, 136]
HB3	0.52	3.4×10^{-16}	Fe	LPE			[134, 136]
HB4	0.44	3.4×10^{-14}	Cu	LPE	200[128]	0.01	[134, 136]
HB5	0.40	2.2×10^{-13}		LPE			[134, 136]
HB6*	0.29	2.0×10^{-14}		LPE			[134]
HL1	0.94	3.7×10^{-14}		VPE			[134]
HL2	0.73	1.9×10^{-14}		LPE			[134]
HL3	0.59	3.0×10^{-15}	Fe	VPE	300[128]	0.01	[134]
HL4	0.42	3.0×10^{-15}	Cu	VPE	200[128]	0.01	[134]

*Electron-irradiated GaAs

REFERENCES CITED

[1] O. Ma, S. Capanna, F. Joseck, J. Nathwani, T. Nguyen, C. Richard, P. Spitsen, L. Boyd, C. Marcy, E. Doe, J. Davis, S. Esterly, D. Feldman, R. Fu, C. Johnson, E. Lantz, A. Livecchi, J. Logan, D. Mooney, R. Newmark, G. Porro, P. Schwabe, A. Smith, T. Tian, T. Williams, and K. Wipke. 2014 Renewable Energy Data Book. Technical report, National Renewable Energy Laboratory, 2014.

[2] D. B. Needleman, J. R. Poindexter, R. C. Kurchin, I. M. Peters, G. Wilson, and T. Buonassisi. Economically Sustainable Scaling of Photovoltaics to Meet Climate Targets. *Energy & Environmental Science*, 9:2122–2129, 2016.

[3] M. Woodhouse and A. Goodrich. A manufacturing cost analysis relevant to single- and dual-junction photovoltaic cells fabricated with III-Vs and III-Vs grown on Czochralski silicon. Technical report, NREL, 2013.

[4] S. W. Bedell, D. Shahrjerdi, B. Hekmatshoar, K. Fogel, P. A. Lauro, J. A. Ott, N. Sosa, and D. Sadana. Kerf-less removal of Si, Ge, and III-V layers by controlled spalling to enable low-cost PV technologies. *IEEE Journal of Photovoltaics*, 2(2):141–147, 2012.

[5] E. D. E. Kosten, J. H. J. Atwater, J. Parsons, A. Polman, and H. A. Atwater. Highly efficient GaAs solar cells by limiting light emission angle. *Light: Science & Applications*, 2(1):1–6, 2013.

[6] J. Simon, D. Young, and A. Ptak. Low-Cost III-V Solar Cells Grown by Hydride Vapor-Phase Epitaxy. *40th IEEE Phot. Spec. Conf.*, pages 538–541, 2014.

[7] J. Simon, K. L. Schulte, D. L. Young, N. M. Haegel, and A. J. Ptak. GaAs Solar Cells Grown by Hydride Vapor-Phase Epitaxy and the Development of GaInP Cladding Layers. *IEEE Journal of Photovoltaics*, 6:191–195, 2016.

[8] M. Zheng, H.-P. Wang, C. M. Sutter-Fella, C. Battaglia, S. Aloni, X. Wang, J. Moore, J. W. Beeman, M. Hettick, M. Amani, W.-T. Hsu, J. W. Ager, P. Bermel, M. Lundstrom, J.-H. He, and A. Javey. Thin-Film Solar Cells with InP Absorber Layers Directly Grown on Nonepitaxial Metal Substrates. *Advanced Energy Materials*, 5(22), 2015.

[9] K. Chen, R. Kapadia, A. Harker, S. Desai, J. Seuk Kang, S. Chuang, M. Tosun, C. M. Sutter-Fella, M. Tsang, Y. Zeng, D. Kiriya, J. Hazra, S. R. Madhvapathy, M. Hettick, Y.-Z. Chen, J. Mastandrea, M. Amani, S. Cabrini, Y.-L. Chueh, J. W. Ager III, D. C. Chrzan, and A. Javey. Direct growth of single-crystalline IIIV semiconductors on amorphous substrates. *Nature Communications*, 7:10502, 2016.

[10] F. Nicoll. The use of close spacing in chemical-transport systems for growing epitaxial layers of semiconductors. *J. Electrochem. Soc.*, 110(11):1165–1167, 1963.

[11] A. J. Ritenour, R. C. Cramer, S. Levinrad, and S. W. Boettcher. Efficient n-GaAs photoelectrodes grown by close-spaced vapor transport from a solid source. *ACS Appl. Mater. Interfaces*, 4:69–73, 2012.

[12] A. J. Ritenour and S. W. Boettcher. Towards high-efficiency GaAs thin-film solar cells grown via close space vapor transport from a solid source. In *38th IEEE Phot. Spec. Conf.*, pages 913–917, 2012.

[13] A. J. Hurd, R. L. Kelley, R. G. Eggert, and M.-H. Lee. Energy-critical elements for sustainable development. *MRS Bull.*, 37(04):405–410, 2012.

[14] U. Wurfel, A. Cuevas, and P. Wurfel. Charge carrier separation in solar cells. *IEEE Journal of Photovoltaics*, 5(1):461–469, 2015.

[15] W. Shockley. The Theory of p-n Junctions in Semiconductors and p-n Junction Transistors. *Bell Syst. Tech. J.*, 28(3):435–489, 1949.

[16] W. Shockley and H. J. Queisser. Detailed Balance Limit of Efficiency of p-n Junction Solar Cells. *Journal of Applied Physics*, 32(3):510, 1961.

[17] S. Sze and K. K. Ng. *Physics of Semiconductor Devices*. Wiley, 3 edition, 2007.

[18] D. Côté, J. Dodelet, B. Lombos, and J. Dickson. Epitaxy of GaAs by the close-spaced vapor transport technique. *Journal of The Electrochemical Society*, 133(9), 1986.

[19] M. Gandouzi, J. Bourgoin, J. Mimila-Arroyo, C. Grattepain, and C. Grattepain. Impurity incorporation during epitaxial growth of GaAs by chemical reaction. *Journal of Crystal Growth*, 218(2-4):167–172, sep 2000.

[20] M. Binnewies, R. Glaum, M. Schmidt, and P. Schmidt. Chemical Vapor Transport Reactions - A Historical Review. *Zeitschrift für anorganische und allgemeine Chemie*, 639(2):219–229, feb 2013.

[21] R. Glew. Zinc doping of MOCVD GaAs. *Journal of Crystal Growth*, 68:44–47, 1984.

[22] X. Tang, H. Lochs, P. Hageman, M. de Croon, L. Giling, and a.J. Bons. Si-doping of MOCVD GaAs: Closer analysis of the incorporation process. *Journal of Crystal Growth*, 98(4):827–837, 1989.

[23] a. De Vita, M. J. Gillan, J. S. Lin, M. C. Payne, I. Tich, and L. J. Clarke. Defect energetics in MgO treated by first-principles methods. *Physical Review B*, 46(20):12964–12973, 1992.

[24] D. Reynolds, C. Litton, E. Smith, P. Yu, and K. Bajaj. Photoluminescence studies of the amphoteric behavior of carbon and germanium in GaAs. *Solid State Communications*, 42(11):827–830, 1982.

[25] C. Le Bel, D. Cossement, J. P. Dodelet, R. Leonelli, Y. DePuydt, and P. Bertrand. Doping and residual impurities in GaAs layers grown by close-spaced vapor transport. *J. Appl. Phys.*, 73(3):1288, 1993.

[26] R. Castro-Rodriguez. Close-spaced vapor transport combined with free evaporation for doping of semiconductor thin films. *Journal of Vacuum Science & Technology A: Vacuum, Surfaces, and Films*, 11(3):730, may 1993.

[27] P.-a. Hoss, L. Murray, and J. Rivera. The CloseSpaced Growth of Degenerate PType GaAs, GaP, and Ga (As x, P 1 x) by ZnCl2 Transport for Tunnel Diodes. *Journal of The Electrochemical . . .*, 115(5):7–10, 1968.

[28] A. J. Ritenour, J. W. Boucher, R. DeLancey, A. L. Greenaway, S. Aloni, and S. W. Boettcher. Doping and electronic properties of GaAs grown by close-spaced vapor transport from powder sources for scalable IIIV photovoltaics. *Energy Environ. Sci.*, 8:278–285, sep 2015.

[29] C. Lin and C. P. Lee. Comparison of Au/Ni/Ge, Au/Pd/Ge, and Au/Pt/Ge Ohmic contacts to n-type GaAs. *J. Appl. Phys.*, 67(1):260, 1990.

[30] H. R. Kawata, T. Oku, A. Otsuki, and M. Murakami. NiGe-based ohmic contacts to n-type GaAs. II. Effects of Au addition. *J. Appl. Phys.*, 75(5):2530, 1994.

[31] H. Lin and S. Senanayake. Optimization of AuGe-Ni-Au ohmic contacts for GaAs MOSFETs. *IEEE T. Electron. Dev.*, 50(4):880–885, 2003.

[32] M. Otsubo, T. Oda, H. Kumabe, and H. Miki. Preferential etching of GaAs through photoresist masks. *J. Electrochem. Soc.*, pages 676–680, 1976.

[33] D. A. Clugston and P. A. Basore. PC1D version 5: 32-bit solar cell modeling on personal computers. *26th IEEE Phot. Spec. Conf.*, pages 4–7, 1997.

[34] M. Burgelman, P. Nollet, and S. Degrave. Modelling polycrystalline semiconductor solar cells. *Thin Solid Films*, 361:527–532, 2000.

[35] J. Boucher, A. Ritenour, and S. Boettcher. Towards low-cost high-efficiency GaAs photovoltaics and photoelectrodes grown via vapor transport from a solid source. *Proc. SPIE*, 8725, 2013.

[36] R. Wilson, F. Stevie, and C. Magee. *Appendix E of Secondary Ion Mass Spectrometry: A Practical Handbook for Depth Profiling and Bulk Impurity Analysis.* Wiley, New York, 1989.

[37] H. Ibach and H. Luth. *Solid-State Physics*. Springer, New York, 2009.

[38] J. Nelson. *The physics of solar cells*. Imperial College Press, 2003.

[39] S. S. Hegedus and W. N. Shafarman. Thin-film solar cells: device measurements and analysis. *Progress in Photovoltaics: Research and Applications*, 12(23):155–176, mar 2004.

[40] K. R. McIntosh. *Lumps, humps and bumps: Three detrimental effects in the current-voltage curve of silicon solar cells*. PhD thesis, University of New South Wales, 2001.

[41] E. Yablonovitch, C. J. Sandroff, R. Bhat, and T. Gmitter. Nearly ideal electronic properties of sulfide coated GaAs surfaces. *Applied Physics Letters*, 51(6):439–441, 1987.

[42] C. J. Sandroff, M. Hegde, and C. Chang. Structure and stability of passivating arsenic sulfide phases on GaAs surfaces. *Journal of Vacuum Science & Technology B: Microelectronics and Nanometer Structures*, 7(4):841, 1989.

[43] M. Sotoodeh, A. H. Khalid, and A. A. Rezazadeh. Empirical low-field mobility model for III-V compounds applicable in device simulation codes. *Journal of Applied PhysicsA*, 87(6):2890–2900, 2000.

[44] W. Walukiewicz, L. Lagowski, L. Jastrzebski, M. Lichtensteiger, and H. C. Gatos. Electron mobility and free-carrier absorption in GaAs: Determination of the compensation ratio. *Journal of Applied Physics*, 50(2):899, 1979.

[45] J. Heath and P. Zabierowski. Capacitance spectroscopy of thin film solar cells. In D. Abou-Ras, T. Kirchartz, and U. Rau, editors, *Advanced Characterization Techniques for Thin Film Solar Cells*, chapter 4, pages 118–147. Wiley, 2011.

[46] C. E. Michelson, a. V. Gelatos, and J. D. Cohen. Drive-level capacitance profiling: Its application to determining gap state densities in hydrogenated amorphous silicon films. *Applied Physics Letters*, 47(4):412, 1985.

[47] D. V. Lang. Deep-level transient spectroscopy: A new method to characterize traps in semiconductors. *Journal of Applied Physics*, 45(7):3023–3032, 1974.

[48] C. Henry and D. Lang. Nonradiative capture and recombination by multiphonon emission in GaAs and GaP. *Physical Review B*, 15, 1977.

[49] C. R. Crowell and S. Alipanahi. Transient distortion and nth order filtering in deep level transient spectroscopy (DnLTS). *Solid State Electronics*, 24(1):25–36, 1981.

[50] P. Blood and J. Orton. *The electrical characterization of semiconductors: majority carriers and electron states.* Academic Press Ltd., San Diego, 1992.

[51] A. V. Gelatos, J. D. Cohen, and J. P. Harbison. Assessment of lattice relaxation effects in transitions from mobility gap states in hydrogenated amorphous silicon using transient photocapacitance techniques. *Applied Physics Letters*, 49(12):722, 1986.

[52] J. T. Heath, J. D. Cohen, W. N. Shafarman, D. X. Liao, and a. a. Rockett. Effect of Ga content on defect states in CuIn(1-x)GaxSe2 photovoltaic devices. *Applied Physics Letters*, 80(24):4540, 2002.

[53] P. T. Erslev, H. Q. Chiang, D. Hong, J. F. Wager, and J. D. Cohen. Electronic properties of amorphous zinc tin oxide films by junction capacitance methods. *Journal of Non-Crystalline Solids*, 354(19-25):2801–2804, may 2008.

[54] D. W. Miller, C. W. Warren, O. Gunawan, T. Gokmen, D. B. Mitzi, and J. D. Cohen. Electronically active defects in the Cu2ZnSn(Se,S)4 alloys as revealed by transient photocapacitance spectroscopy. *Applied Physics Letters*, 101(14):142106, 2012.

[55] A. V. Gelatos, K. K. Mahavadi, J. D. Cohen, and J. P. Harbison. Transient photocapacitance and photocurrent studies of undoped hydrogenated amorphous silicon. *Applied Physics Letters*, 53(5):403, 1988.

[56] L. Casagrande, A. Juang, and N. Lewis. Photoelectrochemical behavior of n-GaAs and n-Al_xGa_{1-x}As in CH_3CN. *J. Phys. Chem. B*, 104:5436–5447, 2000.

[57] W. Gärtner. Depletion-layer photoeffects in semiconductors. *Physical Review*, 116:0–3, 1959.

[58] S. Sze and J. Irvin. Resistivity, mobility and impurity levels in GaAs, Ge, and Si at 300K. *Solid-State Electronics*, 11(6):599–602, 1968.

[59] E. Palik, editor. *Handbook of Optical Constants of Solids.* Academic Press, London, 1997.

[60] I. García, I. Rey-Stolle, B. Galiana, and C. Algora. Analysis of tellurium as n-type dopant in GaInP: Doping, diffusion, memory effect and surfactant properties. *Journal of Crystal Growth*, 298:794–799, jan 2007.

[61] W. L. Rance, D. L. Young, K. L. Schulte, T. F. Kuech, A. J. Ptak, and R. C. Reedy. Controlled formation of GaAs pn junctions during hydride vapor phase epitaxy of GaAs. *Journal of Crystal Growth*, 352(1):253–257, 2012.

[62] J. C. Bourgoin, D. Stievenard, D. Deresmes, and J. Mimila Arroyo. Oxygen in gallium arsenide. *Journal of Applied Physics*, 69(1):284–290, 1991.

[63] J. Mimila-Arroyo, R. Legros, J. C. Bourgoin, and F. Chavez. Photoluminescence and electrical properties of close space vapor transport GaAs epitaxial layers. *Journal of Applied Physics*, 58(9):3652–3654, 1985.

[64] Z. Huang, N. Guelton, D. Cossement, D. Guay, R. Saint-Jacques, and J. Dodelet. Optimization of the surface morphology of GaAs epitaxial layers grown by close-spaced vapor transport. *Canadian J. Phys.*, 71:462–469, 1993.

[65] A. Baca, F. Ren, J. Zolper, R. Briggs, and S. Pearton. A survey of ohmic contacts to III-V compound semiconductors. *Thin Solid Films*, 308-309:599–606, oct 1997.

[66] M. Murakami, K. Childs, J. M. Baker, and A. Callegari. Microstructure studies of AuNiGe Ohmic contacts to n-type GaAs. *Journal of Vacuum Science & Technology B: Microelectronics and Nanometer Structures*, 4:903–911, 1986.

[67] A. L. Greenaway, A. L. Davis, J. W. Boucher, A. J. Ritenour, S. Aloni, and S. Boettcher. Gallium arsenide phosphide grown by close-spaced vapor transport from mixed powder sources for low-cost III-V photovoltaic and photoelectrochemical devices. *J. Mater. Chem. A*, 4:2909–2918, 2016.

[68] B. A. Lombos, T. Bretagnon, A. Jean, R. Le Van Mao, S. Bourassa, and J. P. Dodelet. EL2 trends in As-rich GaAs grown by close-spaced vapor transport. *Journal of Applied Physics*, 67(4):1879–1883, 1990.

[69] D. R. Lide, editor. *CRC Handbook of Chemistry and Physics.* CRC Press, Inc., 1995.

[70] N. J. Kadhim and D. Mukherjee. Growth model of oval defect structures in MBE GaAs layers. *Journal of Materials Science Letters*, 18(3):229–232, 1999.

[71] H. Kakibayashi, F. Nagata, Y. Katayama, and Y. Shiraki. Structure analysis of oval defects on molecular beam epitaxial GaAs layer by cross-sectional transmition electron microscopy observation. *Japanese J. Appl. Phys*, 23(11):L846–L848, 1984.

[72] Y. G. Chai and R. Chow. Source and elimination of oval defects on GaAs films grown by molecular beam epitaxy. *Applied Physics Letters*, 38(10):796–798, 1981.

[73] D. G. Schlom. Reduction of gallium-related oval defects. *Journal of Vacuum Science & Technology B: Microelectronics and Nanometer Structures*, 7(2):296–298, 1989.

[74] K. Fujiwara, K. Kanamoto, Y. Ohta, Y. Tokuda, and T. Nakayama. Classification and origins of GaAs oval defects grown by molecular beam epitaxy. *Journal of Crystal Growth*, 80(1):104–112, 1987.

[75] N. Chand and S. Chu. A comprehensive study and methods of elimination of oval defects in MBE-GaAs. *Journal of Crystal Growth*, 104(2):485–497, 1990.

[76] M. E. Weiner. Si Contamination in Open Flow Quartz Systems for the Growth of GaAs and GaP. *J. Electrochem. Soc.*, 119(4):496–504, 1972.

[77] R. H. Lamoreaux, D. L. Hildenbrand, and L. Brewer. High-Temperature Vaporization Behavior of Oxides II. Oxides of Be, Mg, Ca, Sr, Ba, B, Al, Ga, In, Tl, Si, Ge, Sn, Pb, Zn, Cd, and Hg. *Journal of Physical and Chemical Reference Data*, 16(3):419–443, 1987.

[78] J. Dabrowski and M. Scheffler. Isolated arsenic-antisite defect in GaAs and the properties of EL2. *Physical Review B*, 40(15):10391–10401, 1989.

[79] J. Lagowski. Passivation of the dominant deep level (EL2) in GaAs by hydrogen. *Applied Physics Letters*, 41(11):1078, 1982.

[80] W. L. Wang, S. S. Li, and D. H. Lee. On the physical origins of the EL2 center in GaAs. *Solid State Sci. Tech.*, 133(1):196–199, 1986.

[81] H. von Bardeleben and D. Stievenard. Identification of a defect in a semiconductor: EL2 in GaAs. *Physical Review B*, 34(10):7192–7202, 1986.

[82] R. A. Morrow. Model of EL2 formation in GaAs. *Journal of Applied Physics*, 70(11):6782–6789, 1991.

[83] A. M. Huber, N. T. Linh, M. Valladon, J. L. Debrun, G. M. Martin, A. Mitonneau, and A. Mircea. Direct evidence for the nonassignment to oxygen of the main electron trap in GaAs. *Journal of Applied Physics*, 50(6):4022, 1979.

[84] J. Lagowski, D. G. Lin, T. Aoyama, and H. C. Gatos. Identification of oxygen-related midgap level in GaAs. *Applied Physics Letters*, 44(3):336–338, 1984.

[85] K. J. Schmieder, E. A. Armour, M. P. Lumb, M. K. Yakes, Z. Pulwin, J. Frantz, and R. J. Walters. Effect of growth temperature on GaAs solar cells at high MOCVD growth rates. *44th Phot. Spec. Conf.*, 2016.

[86] K. L. Schulte and T. F. Kuech. A model for arsenic anti-site incorporation in GaAs grown by hydride vapor phase epitaxy. *Journal of Applied Physics*, 116(24):243504, dec 2014.

[87] R. Castenedo, J. Mimila-Arroyo, and J. C. Bourgoin. Semi-insulating epitaxial GaAs. *Journal of Applied Physics*, 68(12):6274, 1990.

[88] M. Hammadi, J. Bourgoin, and H. Samic. Mechanism of GaAs transport by water reaction application to the growth of thick epitaxial layers. *Journal of Materials Science*, 10:399–402, 1999.

[89] T. Bretagnon and A. Jean. Midgap electron traps in n-type GaAs epitaxial layers grown by the close-spaced vapor transport technique. *Can. J. Phys.*, 69:407, 1991.

[90] G. Masse, M. Lawrence, and J. Lacroix. Dominant donor trap in n-type epitaxial GaAs grown by CSVT. *J. Phys. Chem. Solids*, 49(I):1349–1353, 1988.

[91] N. Talbi, K. Khirouni, G. C. Sun, H. Samic, and J. C. Bourgoin. Electronic characterization of several 100 μm thick epitaxial GaAs layers. *Journal of Materials Science: Materials in Electronics*, 19(5):487–492, aug 2007.

[92] T. Mattila and R. Nieminen. Ab initio study of oxygen point defects in GaAs, GaN, and AlN. *Physical review. B*, 54(23):16676–16682, 1996.

[93] D. Colleoni and A. Pasquarello. The OAs defect in GaAs: A hybrid density functional study. *Applied Surface Science*, 291:6–10, 2014.

[94] W. Orellana and A. C. Ferraz. Structural properties and energetics of oxygen impurities in GaAs. *Physical Review B*, 61(8):5326–5331, 2000.

[95] A. Taguchi and H. Kageshima. First-principles investigation of the oxygen negative- U center in GaAs. *Phys. Rev. B*, 57(12):6779–6782, 1998.

[96] D. Colleoni and A. Pasquarello. Oxygen defects in GaAs: A hybrid functional study. *Applied Physics Letters*, 93:125208, 2016.

[97] M. Pesola, J. Boehm, V. Sammalkorpi, T. Mattila, and R. Nieminen. Microscopic structure of oxygen defects in gallium arsenide. *Physical Review B*, 60(24):R16267–R16270, 1999.

[98] T. F. Kuech, S. Nayak, and J. Huang. Chemical and physical effects in oxygen incorporation during the metalorganic vapor phase epitaxial growth of GaAs. *Journal of Crystal Growth*, 163:171–179, 1996.

[99] M. Skowronski. Absorption spectrum of EL2 defect in p-type GaAs. *Journal of Applied Physics*, 68(7):3741, 1990.

[100] J. Huang and T. Kuech. Multiple deep levels in metalorganic vapor phase epitaxy GaAs grown by controlled oxygen incorporation. *Applied physics letters*, 65(5):604–606, 1994.

[101] U. Kaufmann, E. Klausmann, and J. Schneider. Negative-U, off-center OAs in GaAs and its relation to the EL3 level. *Phys. Rev. B*, 43(14):12106, 1991.

[102] H. C. Alt. Experimental evidence for a negative- U center in gallium arsenide related to oxygen. *Physical Review Letters*, 65(27):3421–3424, 1990.

[103] X. H. Xiao and J. Zhu. Formation of thick , thermally-stable high-resistivity-layers in GaAs by oxygen ion implantation. *Jpn. J. Appl. Phys.*, 20(5):901–907, 1981.

[104] M. R. Brozel, R. C. Newman, J. B. Clegg, B. Clerjaud, G. M. Martin, A. Mitonneau, T. Hashizume, H. Nagabuchi, B. Tuck, D. Pons, J. C. Bourgoin, P. Blood, and J. W. Orton. Oxygen-related gettering of silicon during growth of bulk GaAs Bridgman crystals. *J. Phys. C.*, 15:1841, 1982.

[105] J. W. Huang, K. L. Bray, and T. F. Kuech. Compensation of shallow impurities in oxygen-doped metalorganic vapor phase epitaxy grown GaAs. *Journal of Applied Physics*, 80(12):6819, 1996.

[106] S. W. Johnston, S. R. Kurtz, D. J. Friedman, A. J. Ptak, R. K. Ahrenkiel, and R. S. Crandall. Observed trapping of minority-carrier electrons in p -type GaAsN during deep-level transient spectroscopy measurement. *Applied Physics Letters*, 86(7):1–3, 2005.

[107] S. W. Johnston and S. R. Kurtz. Comparison of a dominant electron trap in n-type and p-type GaNAs using deep-level transient spectroscopy. *Journal of Vacuum Science & Technology A: Vacuum, Surfaces, and Films*, 24(4):1252, 2006.

[108] D. T. J. Hurle. A comprehensive thermodynamic analysis of native point defect and dopant solubilities in gallium arsenide. *Journal of Applied Physics*, 85(10):6957, 1999.

[109] D. T. J. Hurle. A thermodynamic analysis of native point defect and dopant solubilities in zinc-blende III-V semiconductors. *Journal of Applied Physics*, 107(12):121301, 2010.

[110] R. Willardson and A. Beer, editors. *Semiconductors and Semimetals: Physics of III-V compounds*. Academic Press, 1966.

[111] G. M. Martin. Optical assessment of the main electron trap in bulk semi-insulating GaAs. *Applied Physics Letters*, 39(9):747, 1981.

[112] M. Skowronski. Oxygen in gallium arsenide. In S. T. Pantelides, editor, *Deep Centers in Semiconductors*, pages 383–388. Gordon and Breach Science Publishers, 1992.

[113] P. N. Favennec. Chromium gettering in GaAs by oxygen implantation. *Applied Physics Letters*, 38(4):271, 1981.

[114] K. Shikano, K. Kobayashi, and S. Miyazawa. Oxygen distribution in a horizontal Bridgman-grown , semi-insulating GaAs ingot. *Appl. Phys. Lett.*, 46:391–393, 1984.

[115] K. Fujii, F. Orito, H. Fujita, and T. Sato. The role of diffusion barrier temperature in gallium arsenide crystals grown by the gradient freeze method. *J. Cryst. Growth*, 121:255–266, 1992.

[116] M. A. Green, K. Emery, Y. Hishikawa, W. Warta, and E. D. Dunlop. Solar cell efficiency tables (Version 38). *Progess in Photovoltaics: Research and Applications*, 19(5):565–572, 2011.

[117] M. A. Green, K. Emery, Y. Hishikawa, W. Warta, and E. Dunlop. Solar cell efficiency tables (version 48). *Prog. Photovolt: Res. Appl.*, 24:905–913, 2016.

[118] A. Onno, N.-P. Harder, L. Oberbeck, and H. Liu. Simulation study of GaAsP/Si tandem solar cells. *Solar Energy Materials and Solar Cells*, 145:206–216, 2016.

[119] G. E. Gottlieb. Vapor Phase Transport and Epitaxial Growth of GaAs(1-x)P(x) Using Water Vapor. *Journal of the Electrochemical Society*, 112(2):192–196, 1965.

[120] R. K. Purohit. Close-Spaced Epitaxial Growth of GaAsxP1-x from powder gaas and gap. *Journal of Materials Sicence 3*, 3(3):330–332, 1968.

[121] J. F. Nicolau, K. W. Benz, and J. U. Fischbach. InP epitaxial growth by the close-spaced method. *Symposium on Gallium Arsenide*, 1972.

[122] C. Frosch. The Epitaxial Growth of GaP by a Ga2 O Vapor Transport Mechanism. *Journal of The Electrochemical Society*, 1964.

[123] M. G. Mauk, A. N. Tata, and B. W. Feyock. Selectively-grown InGaP/GaAs on silicon heterostructures for application to photovoltaicphotoelectrolysis cells. *Journal of Crystal Growth*, 225(2-4):359–365, may 2001.

[124] R. F. Lever and F. Jona. Epitaxial Growth of Germanium Using Water Vapor. *Journal of Applied Physics*, 34(10):3139, 1963.

[125] R. R. Fergusson and T. Gabor. The Transport of Gallium Arsenide in the Vapor Phase by Chemical Reaction. *J. Electrochem. Soc.*, 111(5), 1962.

[126] P.-A. Hoss, L. A. Murray, and J. J. Rivera. The Close-Spaced Growth of Degenerate P-Type GaAs, GaP, and Ga (Asx , Pl-x) by ZnCI2 Transport for Tunnel Diodes. *Journal of the Electrochemical Society: Solid State Science*, 115(5):553–556, 1968.

[127] H. T. Minden. Pits and Hillocks on Epitaxial GaAs Grown from the Vapor Phase. *Journal of Crystal Growth*, 8(March 1970):37–44, 1971.

[128] P. Blood and J. J. Harris. Deep states in GaAs grown by molecular beam epitaxy. *Journal of Applied Physics*, 56(4):993–1007, 1984.

[129] D. V. Lang, A. Y. Cho, A. C. Gossard, M. Ilegems, and W. Wiegmann. Study of electron traps in n-GaAs grown by molecular beam epitaxy. (USA). *J. Appl. Phys.*, 47:2558, 1976.

[130] N. Chand. Reduction and origin of electron and hole traps in GaAs grown by molecular-beam epitaxy. *Journal of Vacuum Science & Technology B: Microelectronics and Nanometer Structures*, 7(2):399, mar 1989.

[131] A. Mitonneau, A. Mircea, G. Martin, and D. Pons. Electron and hole capture cross-sections at deep centers in gallium arsenide. *Revue de Physicque Appliquee*, 14:853, 1979.

[132] Z. Q. Fang, T. E. Schlesinger, and A. G. Milnes. Evidence for EL6 (Ec- 0.35 eV) acting as a dominant recombination center in n-type horizontal Bridgman GaAs. *Journal of Applied Physics*, 61(11):5047–5050, 1987.

[133] G. Martin, A. Mitonneau, D. Pons, A. Mircea, and D. Woodward. Detailed electrical characterisation of the deep Cr acceptor in. *J. Phys. C: Solid State. Phys*, 13:3855, 1980.

[134] A. Mitonneau, G. Martin, and A. Mircea. Hole traps in bulk and epitaxial GaAs crystals. *Electronics Letters*, 13(22):666, 1977.

[135] K. Sakai and T. Ikoma. Deep levels in gallium arsenide by capacitance methods. *Appl. Phys.*, 5(2):165–171, 1974.

[136] D. Lang and R. Logan. A study of deep levels in GaAs by capacitance spectroscopy. *J. Electron. Mater.*, 4(5):1053–1066, 1975.